Measurements of the Fifth Structure Function of the Deuteron

G.P. Gilfoyle, R. Burrell, C. Copos, K. Gill, K. Greenholt, M. Jordan,
University of Richmond, Richmond, VA, 23173

W.K. Brooks,
Universidad Técnica Federico Santa María, Casilla 110-V Valparaíso, Chile

J.D. Lachniet, B.P. Quinn,
Carnegie Mellon University, Pittsburgh, Pennsylvania 15213

M.F. Vineyard
Union College, Schenectady, NY 12308

October 26, 2012

Abstract

We have measured the asymmetry A'_{LT} associated with the fifth structure function of the deuteron $\sigma_{LT'}$ using the reaction $^2\mathrm{H}(\vec{e},e'p)n$ in quasi-elastic kinematics with CLAS. The hadronic model of nuclear physics is not complete in the GeV region and the theoretical mixture of relativistic corrections, final-state interactions, meson-exchange currents, and isobar configurations is unknown. These data provide a baseline for conventional nuclear physics to meet so that deviations from the hadronic model at higher Q^2 can be attributed to quark-gluon effects with greater confidence. The structure function was extracted by measuring the moments of the out-of-plane production in CLAS. This analysis was performed on the E5 data set that covers the range $\mathrm{Q}^2 = 0.2{-}5.0\ (GeV/c)^2$. It is part of a CLAS Approved Analysis entitled 'Out-of-Plane Measurements of the Structure Functions of the Deuteron'.

Contents

1 Introduction

This CLAS Analysis Note presents the results of a measurement of the asymmetry A'_{LT} associated with the fifth structure function $\sigma_{LT'}$ of the $^2\mathrm{H}(\vec{e}, e'p)n$ reaction in quasi-elastic (QE) kinematics. The motivation of the measurement is to study the transition from a description of nuclei based on hadronic degrees of freedom to one based on quarks and gluons. To quantitatively understand that transition requires a solid understanding of the hadronic model to identify where its breakdown will occur. The structure functions are an essential meeting ground of theory and experiment and this measurement of the so-called 'fifth' structure function extracts this little-known component of the deuteron in a model-independent way.

Understanding the deuteron tests our ability to construct a 'consistent and exact description' of few-body nuclei (^{2}H, ^{3}H, ^{3}He, ^{4}He) [1]. For example, it is an open question whether a single interaction or current operator can account for the attributes of all these nuclei. Calculations using hadronic effects like meson-exchange currents (MEC), isobar configurations (IC), and final-state interactions (FSI) are under development, but have yet to be fully challenged by data in the GeV region [1, 2]. The influence of relativity is also being studied [1, 2, 3, 4, 5]. Previous results at lower Q^2 reveal the onset of many of these effects so a complete, modern calculation is needed to compare with data across the full range of Q^2 to test and understand the hadronic model in this region. These issues were raised as 'Key Questions' at the Jefferson Laboratory PAC14 Few-Body Workshop [1].

Improvements in the hadronic model will enable us to clearly map out the transition to quark-gluon degrees of freedom; an essential goal of nuclear physics [1, 6]. The basic idea is that if we cannot describe observations with all of the pieces mentioned above, then we would see genuine quark-gluon effects in the nucleus. Clearly, we cannot make that leap without getting firm control of the calculations using the hadronic degrees of freedom. It is expected the transition may occur in the GeV region or higher and some expect the region $1\ (\mathrm{GeV/c})^2 < Q^2 < 6\ (\mathrm{GeV/c})^2$ to be an ideal one for investigating this transition [2, 6, 7, 8]. The mixture of physics effects that influence the transition also depends on the transferred energy. For quasi-elastic scattering that we study here, FSI and relativistic corrections are important for the structure functions, but MEC and IC are less so [9].

In this CLAS Analysis Note we first present some necessary background defining the asymmetry used as the main analysis tool and describe the context of other measurements of the fifth structure function of the deuteron. We then describe the experiment and how events were selected from the data set. Corrections to the analysis are discussed and then the results are shown including uncertainties. An Appendix contains many details so we could use the main text to focus on the physics.

2 Necessary Background

We now develop some of the necessary background for our discussion of the structure functions. The fivefold differential cross section for the quasielastic $^2\mathrm{H}(\vec{e}, e'p)n$ reaction can be

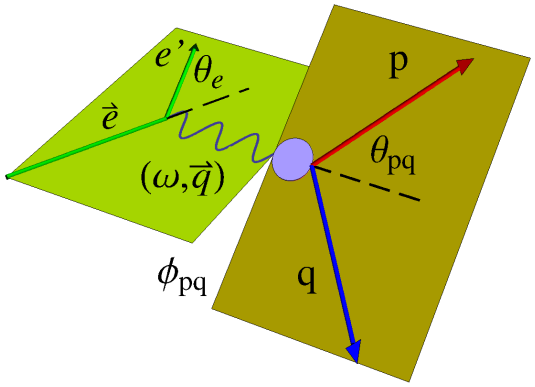

Figure 1: Kinematic quantities used in this analysis.

written as [10]

$$\frac{d^5\sigma}{dQ^2 dp_m d\phi_{pq} d\Omega_e d\Omega_p} = \sigma^{\pm} = c[\rho_L f_L + \rho_T f_T + \rho_{LT} f_{LT} \cos\phi_{pq} + \rho_{TT} f_{TT} \cos 2\phi_{pq} + h\rho_{LT'} f_{LT'} \sin\phi_{pq}] \quad (1)$$

where the superscript on $\sigma^{\pm}$ refers to the helicity, ϕ_{pq} is the angle between the plane defined by the incoming and outgoing electron momenta and the plane defined by the ejected proton and neutron (see Figure 1), the ρ_i's depend only on the electronic kinematics, f_i are the hadronic structure functions, and h is the helicity of the electron beam ($h = \pm 1$). The constant c is

$$c = \frac{\alpha E'}{6\pi^2 E Q^4} \quad (2)$$

where α is the fine structure constant, E is the beam energy, E' is the scattered electron energy, and Q^2 is the square of the 4-momentum transfer. The kinematic quantities are shown in Figure 1. For compactness we write the cross section as

$$\frac{d^5\sigma}{dQ^2 dp_m d\phi_{pq} d\Omega_e d\Omega_p} = \sigma_L + \sigma_T + \sigma_{LT} \cos\phi_{pq} + \sigma_{TT} \cos 2\phi_{pq} + h\sigma_{LT'} \sin\phi_{pq} \quad (3)$$

where the σ_i's are the partial cross sections for each component. Consider the helicity asymmetry [10]

$$A_h(Q^2, p_m, \phi_{pq}) = \frac{\sigma^+ - \sigma^-}{\sigma^+ + \sigma^-} \quad (4)$$

where the superscripts refer to the helicity of the electron beam and p_m is the missing momentum defined as

$$\vec{p}_m = \vec{q} - \vec{p}_p \quad (5)$$

where $\vec{q}$ is the momentum transfer and $\vec{p}_p$ is the measured proton momentum. In the plane-wave impulse approximation this missing momentum is the opposite of the initial momentum

of the proton. The magnitude of p_m grows with increasing θ_{pq} where θ_{pq} is the angle between the momentum transfer $\vec{q}$ and the proton 3-momentum $\vec{p}_p$ (see Figure 1). The relationship between the two quantities is described in Ref. [11]. If we pick $\phi_{pq} = 90^\circ$ the asymmetry becomes (see Section 6.1 for more details)

$$A_h(\mathrm{Q}^2, p_m, \phi_{pq} = 90^\circ) = A^{fa}_{LT'} = \frac{\sigma^+_{90} - \sigma^-_{90}}{\sigma^+_{90} + \sigma^-_{90}} = \frac{\sigma_{LT'}}{\sigma_L + \sigma_T - \sigma_{TT}} \quad . \tag{6}$$

where we call $A^{fa}_{LT'}$ the fixed-angle asymmetry. This form of the asymmetry is used in previous experiments discussed below and is often called simply $A_{LT'}$ in the literature. However, we have used a slightly different form of the helicity asymmetry that enables us to take full advantage of the large acceptance of CLAS. It is the following (see Section 6.1 for more details).

$$A'_{LT} = \frac{\sigma_{LT'}}{\sigma_L + \sigma_T} \tag{7}$$

The difference between Equations 6 and 7 is only in the subtraction of σ_{TT} in the denominator of Equation 6 which is usually small. Within the uncertainties in our measurement we will show in Section 6.3.2 the two are identical.

3 Previous Measurements

Existing measurements of $\sigma_{LT'}$ and its associated amplitude $f_{LT'}$ are sparse. For quasi-elastic kinematics they have only been made at $\mathrm{Q}^2 = 0.22$ $(\mathrm{GeV/c})^2$ and $\mathrm{Q}^2 = 0.13$ $(\mathrm{GeV/c})^2$ at Bates [9, 12, 13]. An example of the results is shown in Figure 2. The bottom panel shows the dependence of the amplitude $f_{LT'}$ on θ_{pq} (see Figure 1) on the bottom scale. The angle θ_{pq} is between the transferred 3-momentum $\vec{q}$ and $\vec{p}_p$ the ejected proton momentum. The top scale shows the magnitude of the missing momentum $\vec{p}_m$. The middle panel shows the results for the asymmetry which is equivalent to the fixed-angle asymmetry $A^{fa}_{LT'}$ in Equation 6 and labeled A'_{LT} in the figure. The top panel shows Σ which is is the non-beam-helicity-dependent part of the cross section. That work demonstrated the feasibility of out-of-plane measurements and the calculations show that relativity already plays a significant role even at this low value of Q^2 [5]. The effect of final-state interactions is dramatic and can be seen in the bottom and middle panels of Figure 2. The dashed lines at $f_{LT'} = 0$ and $A_{LT'} = 0$ are from a Plane-Wave Born Approximation calculation which does not include FSI. In general, $A^{fa}_{LT'}$ and A'_{LT} are non-zero only in the presence of final-state interactions. The other calculation (solid curve) does include FSI and is significantly different from zero in the bottom and middle panels of Figure 2. Unfortunately, the large uncertainties of the measurements prevent one from distinguishing among different phenomena like relativistic corrections, MEC, FSI, and IC or between different potentials. The success of the Bates work at low Q^2 is an invitation to extend the measurements with CLAS.

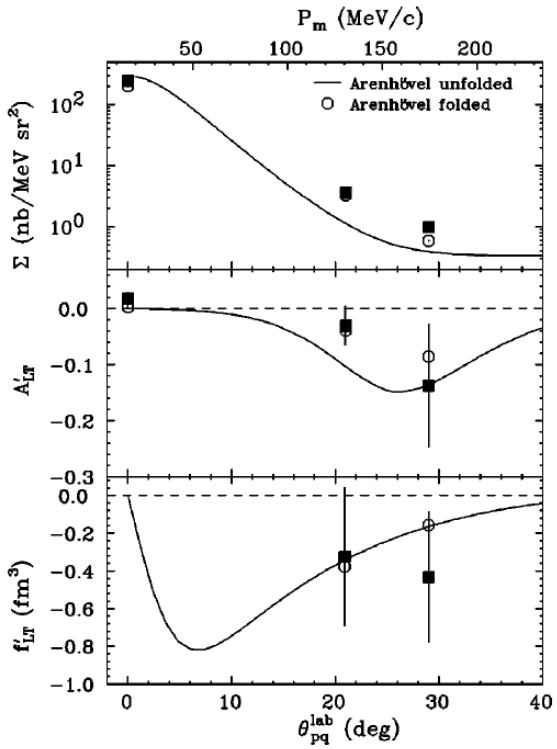

Figure 2: Measurements of $f_{LT'}$ and its associated cross section and asymmetry from Reference [9] at $Q^2 = 0.13$ (GeV/c)^2.

4 Experimental Details

4.1 Data Sets

We are investigating the ^{2}H$(\vec{e}, e'p)n$ reaction by detecting the scattered electron and the ejected proton with CLAS and using missing mass to identify the neutron. The data were collected during the E5 run period (spring, 2000) and consist of runs 24020–24588 at two beam energies: 2.56 GeV and 4.23 GeV. About 2.3 billion triggers were collected under three sets of run conditions shown in Table 1 where normal polarity refers to inbending electrons and reversed polarity is for outbending electrons. We focus most of our attention on the two

Data Set	Beam Energy (GeV)	Torus Current (A)	Polarity
1	4.23	3375	normal
2	2.56	2250	normal
3	2.56	2250	reversed

Table 1: Running conditions for E5.

2.6-GeV data sets because the statistics for the helicity asymmetry are limited at 4.2 GeV.

4.2 Dual-Cell Target

The target for each data set was a dual, co-linear, liquid hydrogen-deuterium cell which enabled us to collect calibration data simultaneously with production data [14]. We used the proton target to check the beam helicity sign, measure the beam charge asymmetry, and to determine momentum corrections. The deuterium cell was 5 cm long and located upstream from the nominal CLAS target position. The hydrogen cell was also 5 cm long and centered on the nominal CLAS target position. There were 4.7 cm between the cells. Figure 3 is an engineering drawing of the target. The cells were constructed of aluminum with thin (20

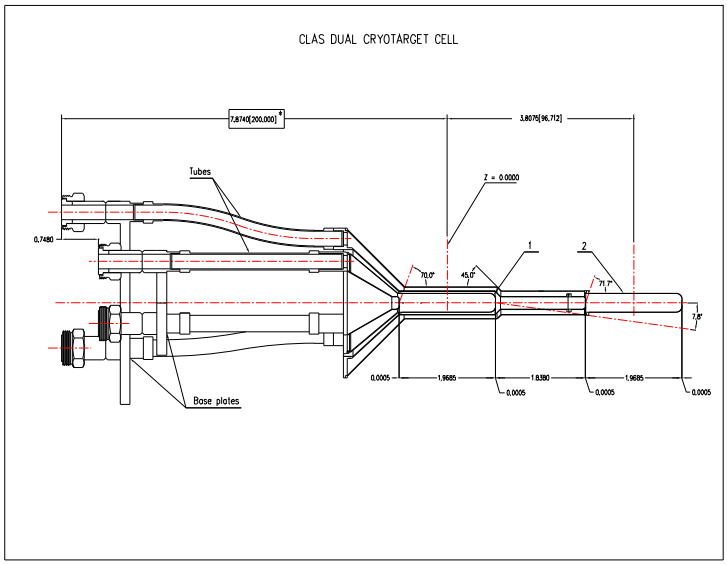

Figure 3: An engineering drawing of the E5 dual-cell cryotarget.

micron) windows on each end. Figure 4 shows the z-component of the electron (black) and proton (red) vertex positions and the clear separation of the deuterium and hydrogen cells.

5 Event Selection of $^2\mathrm{H}(\vec{e}, e'p)n$

5.1 Event Reconstruction

The reconstruction of the E5 data is described in [14]. We summarize that material here. The analysis of the E5 data was performed with a modified version of the CLAS reconstruction software, derived from the 'release-4-3' code. The detectors were calibrated (EC timing and energy, SC timing and energy, DC drift time to drift distance conversion) using the standard packages. Because of the unique, dual-cell target, a set of special 'road files' generated for the E5 target and magnetic field configurations was used as an input template to the RECSIS event reconstruction code. RECSIS returned particle charge, momentum, and position values for charged particles in the drift chamber. Details of the tracking code can be found in [15]. Information from other detector packages, such as hit locations and times in the EC and SC,

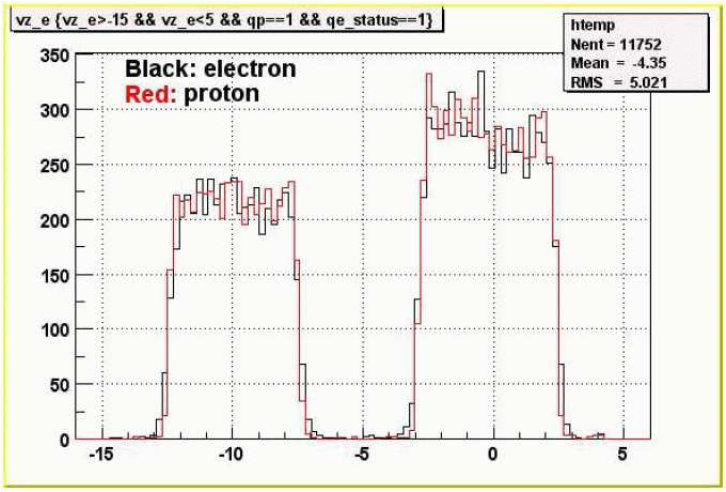

Figure 4: Position of the electron and proton vertex along the beamline for the e5 target for ep events.

were matched to the DC tracks by the SEB package. The reconstructed events were written to BOS files, along with some of the raw event information, to the JLab tape silo.

5.2 Run Selection

Run files were selected for analysis by examining the ratio of protons to electrons originating in the hydrogen target cell, and the ratio of time-based tracks to hit-based tracks. The cuts were selected to remove files in which either of these quantities differed too much from the average. See [14]. Figure 5 shows a sample of those two ratios for the 2.6 GeV, normal-torus-polarity data sets from Ref [14].

5.3 Electron Selection

Electrons were identified as negative tracks from the EVNT bank (produced by SEB) in coincidence with hits in the Cerenkov counters, the TOF scintillators, and the electromagnetic calorimeter. A cut on the number of photo-electrons of greater than 2.5 from the Cerenkov counters was imposed to reduce the number of negative pions mis-identified as electrons [16]. The deuterium target was selected by requiring the electron vertex v_z lie in the range -11.5 cm $< v_z < -8.0$ cm. See Figure 4. A summary of the criteria for identifying electrons is shown in Table 2. More details can be found below and in [14].

We have studied the ^{2}H$(\vec{e}, e'p)n$ reaction in quasielastic kinematics. To select those kinematics for each CLAS torus polarity setting we first calculated W_n, the mass of the residual hadron for the ^{2}H$(\vec{e}, e'p)n$ reaction. We calculate W_n using

$$W_n = \sqrt{M_d^2 - 2M_d E_p + m_p^2 + 2(M_d - E_p)\nu - Q^2 + 2|\vec{p_p}||\vec{q}|\cos\theta_{pq}} \tag{8}$$

where M_d is the deuteron mass, m_p is the proton mass, p_p is the magnitude of the proton 3-momentum, $E_p = \sqrt{p_p^2 + m_p^2}$ is the proton energy, $\nu = E - E'$ is the energy transfer

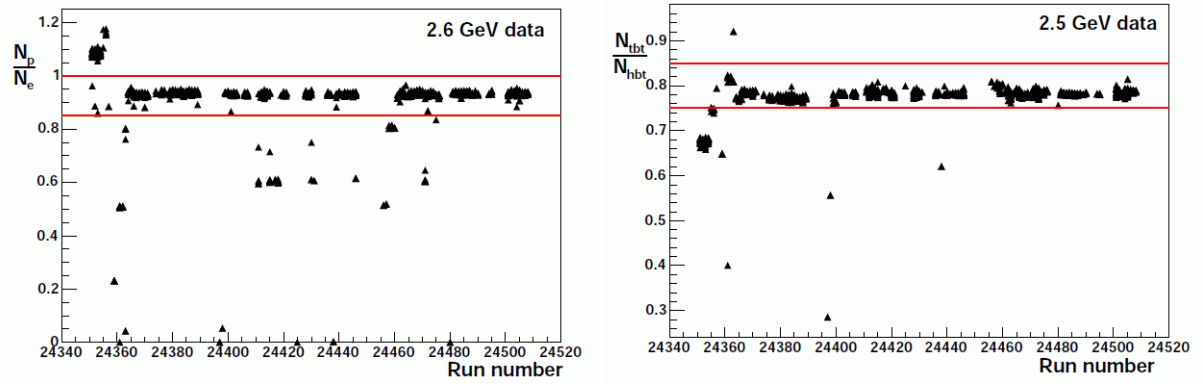

Figure 5: The ratio of the number of protons to the number of electrons for events originating in the hydrogen target versus run number is shown in the left-hand-side panel. The data are from the 2.6-GeV normal-torus-polarity data set. The cuts applied are shown in red. The ratio of the number of time-based tracks to the number of hit-based tracks versus run number is shown in the right-hand-side panel. The data are from the 2.6-GeV, normal-torus-polarity data set. The cuts applied are shown in red. Both plots are from Ref [14].

Description of cut	Parameters
Good CC, EC, SC, status	$cc > 0$, $ec > 0$, $sc > 0$, $stat > 0$
Energy-momentum match	$0.325p_e - 0.13 < E_{total} < 0.325p_e + 0.06$
Reject pions	$ec\_ei \geq 0.100$ and $nphe \geq 25$
EC track coordinates fiducial	$\lvert dc\_ysc\rvert \leq 165(dc\_xsc - 80)/280$
EC fiducial	No tracks within 10 cm of the end of a strip
Egiyan threshold cut	$p_e \geq (214 + 2.47 \cdot ec\_threshold) \cdot 0.001$
Quasi-elastic scattering	$W_n \leq 1.02$ GeV
Select deuterium target	-11.5 cm $< v_z < -8.0$ cm

Table 2: Electron Identification Parameters.

where E is the beam energy and E' is the scattered electron energy, $Q^2 = 4EE'\sin^2\frac{\theta}{2}$ is the square of the electron 4-momentum transfer and θ is the electron scattering angle, $q = |\vec{q}| = \sqrt{Q^2 + \nu^2}$ is the magnitude of the electron 3-momentum transfer, and θ_{pq} is the angle between the proton 3-momentum $\vec{p}_p$ and the 3-momentum transfer $\vec{q}$. The distributions for the two sets of E5 running conditions at $E = 2.6$ GeV are shown in Figure 6. Both panels show a sharp peak at the neutron mass and higher mass inelastic events.

We now discuss choosing the position of the cut on the W_n spectrum to select QE events. If we measured W_n with perfect resolution we would see a spike at the neutron mass ($m_n = 0.94$ GeV) with no other events around it until the pion threshold is reached ($m_{threshold} = m_n + m_\pi = 1.08$ GeV) which would mark the low-mass limit of a broad $N\pi$ distribution. With a real detector, that distribution is smeared by the experimental resolution so some of the $N\pi$ events could contaminate the region below the pion threshold. To remove those events we first determine the mass resolution of the W_n spectrum by fitting

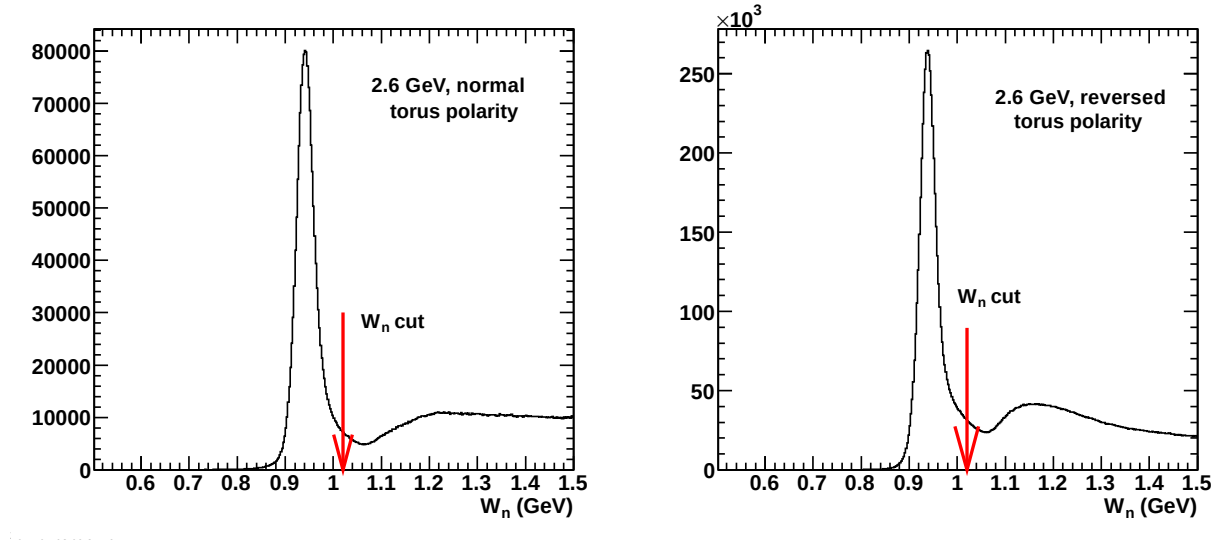

Figure 6: Spectra of W_n for the normal (left-hand panel) and reversed (right-hand panel) polarity data sets at 2.6 GeV. The red arrow marks the position of the cut used to eliminate background events from pion production and higher mass reactions.

the neutron peak for each data set. We obtained nearly the same result for the resolution σ for each data set ($\sigma = 19$ MeV for the 2.6-GeV, reversed-torus-field data and $\sigma = 18$ MeV for the 2.6-GeV, normal-torus-field data set). To form the cut we subtracted 3σ from the pion threshold and call events with W_n below this value quasielastic. The position of the cut for the two data sets is shown as the red arrow in each panel in Figure 6.

We generated fiducial cuts for the electron sample to restrict the acceptance to regions where it is expected to be well-behaved. The azimuthal part of the electron solid angle is determined by the range of the electron's azimuthal angle ϕ_e in each sector. These ϕ_e limits are, in turn, defined by the drop in efficiency in the optical collection of the Cerenkov detector mirrors. See Figure 7 for an example of the ϕ_e dependence. To focus our analysis on the regions of uniform proton acceptance we have largely followed the technique of D.Protopopescu, *et al.* in [17] and summarize the method in Appendix A. The results are shown in Appendix B. One of the benefits of the procedure is to make the fiducial cuts smoothly varying functions of particle momentum and position and reduce the chances of experimental artifacts appearing in the analysis. An example of the final CLAS electron acceptance is shown in Figure 8 for the 2.6-GeV data for both torus polarity settings.

Radiative effects create a long tail so the scattered electron momentum is less than expected for a QE event at that scattering angle. To show this feature consider Figure 9. It shows the scattered electron momentum p_e versus scattering angle θ_e for QE events and reversed torus polarity. The black curve is for electrons elastically scattered from a proton. There is a large ridge in the data which follows the trend of this curve (broadened by the Fermi motion) and a long 'tail' of events that lie at p_e below what is expected for QE events. We will correct for events in the ridge lost to radiation (see Section 6.2.4). To exclude the tail,

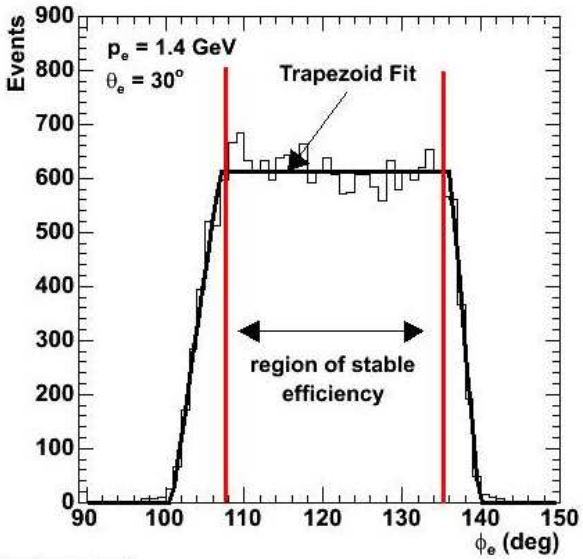

Figure 7: Electron azimuthal dependence for sector 3, 2.6-GeV, normal polarity run. The electron momentum and polar angle θ_e are given on each plot. The black curve is the result a fit to a trapezoidal function described in Appendix A.

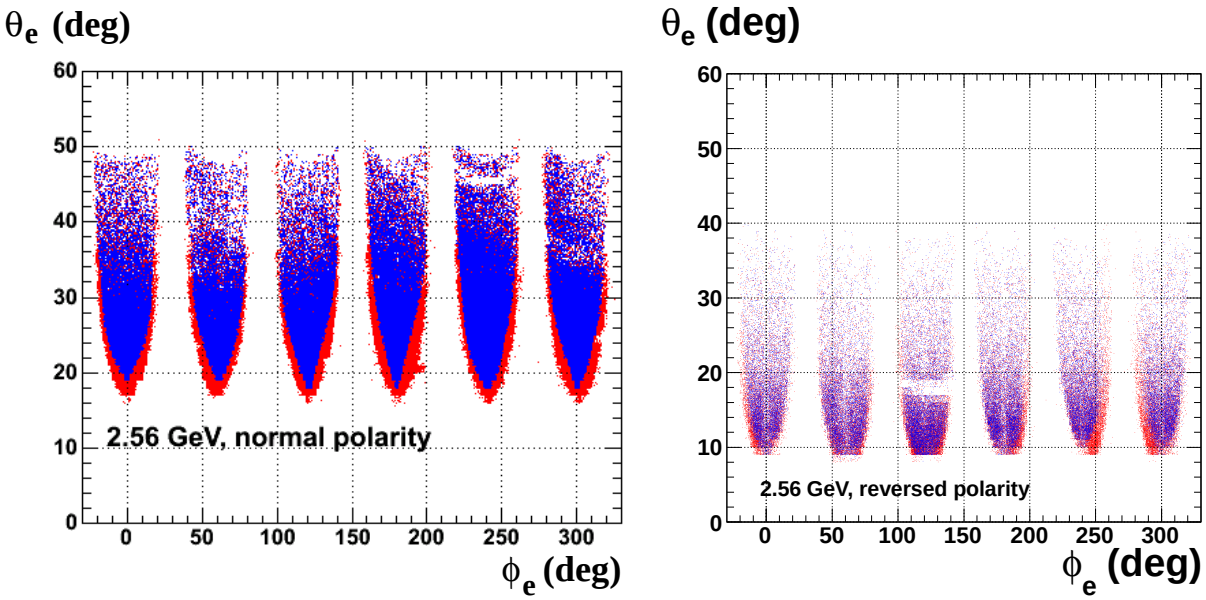

Figure 8: CLAS acceptance for electrons at E = 2.56 GeV and normal torus polarity (left-hand panel) with fiducial cuts turned on (blue points) and off (red points). The right-hand panel shows the same result for the E = 2.56 GeV, reversed torus polarity data.

we first calculate the scattered electron momentum p_e^{calc} using only the scattered electron angle from the CLAS reconstruction and, second, take the difference between this calculated

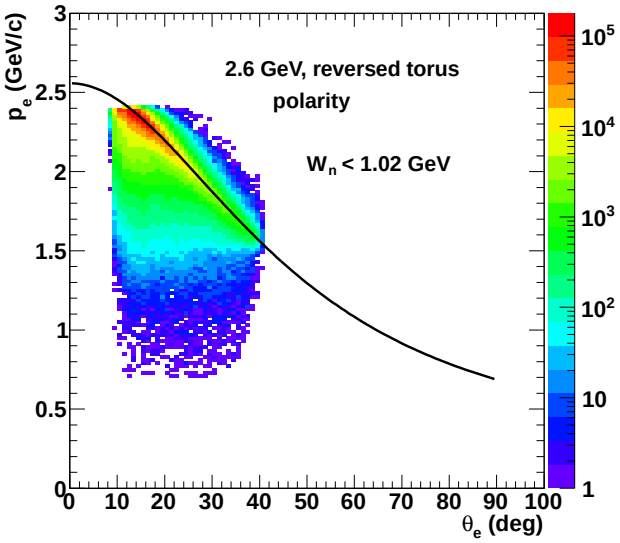

Figure 9: Scattered electron momentum p_e versus scattering angle θ_e for QE events and reversed torus polarity. The black curve shows the kinematics for elastic scattering off the proton.

value and the one from the reconstruction $\Delta p_e = p_e^{calc} - p_e$. The Δp_e distributions are shown for both data sets in Figure 10. The right-hand panel has the distribution for the reversed

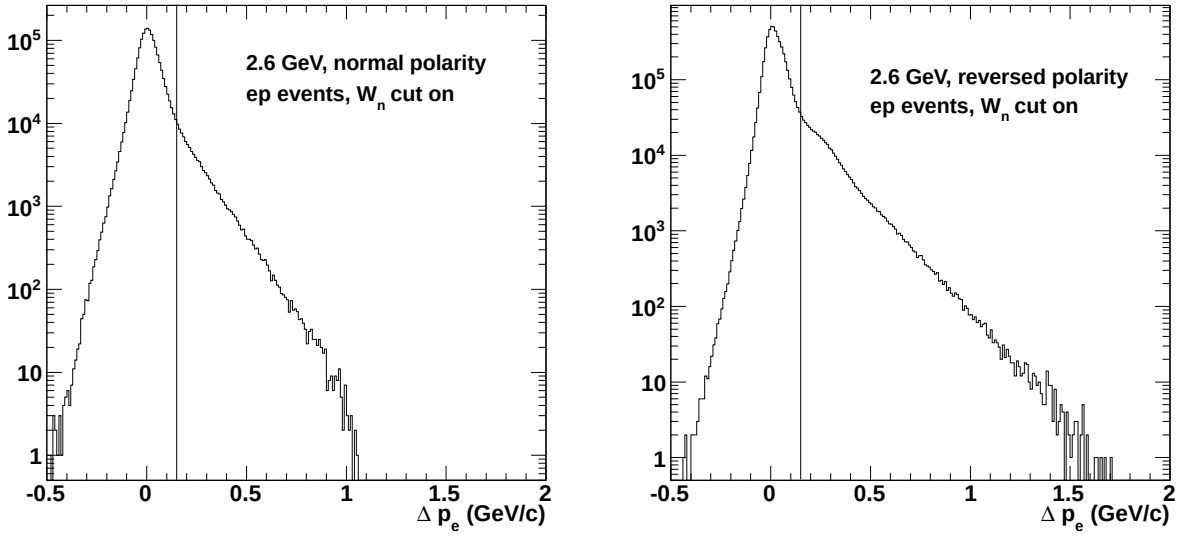

Figure 10: Distribution of Δp_e for normal (left) and reversed (right) polarity data for QE events ($W_n < 1.02$ GeV) and electron/proton fiducial cuts turned on.

torus data. There is a peak centered at zero as expected and a large tail that dominates the spectrum above $\Delta p_e > 0.15$ GeV. The 2.6-GeV, normal polarity data (left-hand panel) shows the same behavior. Based on the results in Figure 10 we require $\Delta p_e < 0.15$ GeV to exclude events with large radiative effects.

To study the impact of this last cut we investigate the Bjorken x_{Bj} distribution. Figure 11 shows the effect of the QE cut on W_n for each 2.6-GeV data set. The black histograms

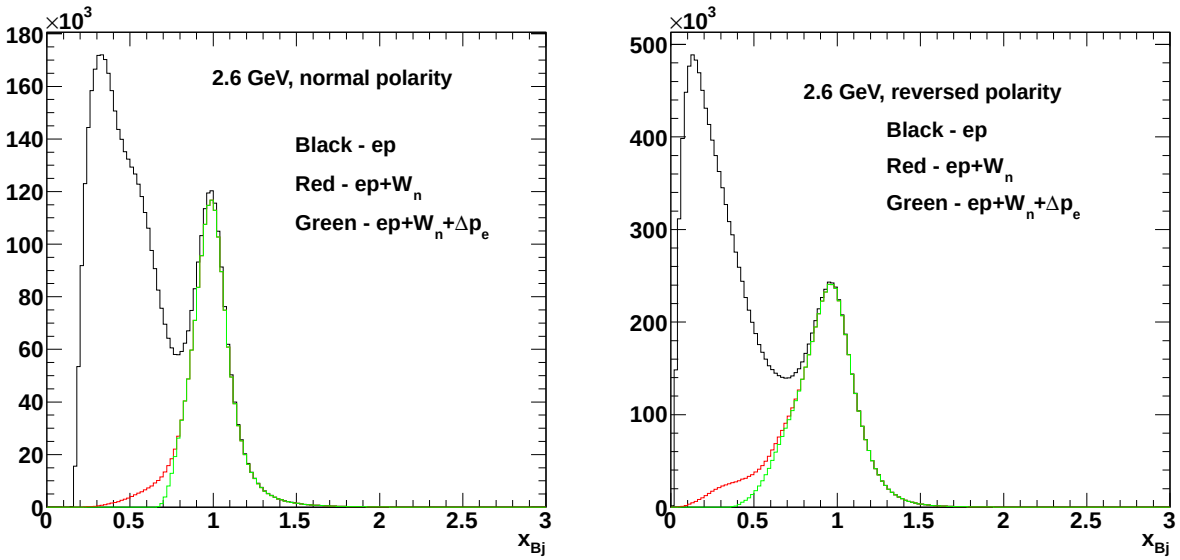

Figure 11: Comparison of Bjorken x with $W_n < 1.02$ GeV cut off (black) and on (red) and with fiducial cuts on for the 2.6-GeV, normal-torus-polarity field (left-hand panel) and the 2.6-GeV, reversed-torus-polarity field (right-hand panel). The green histogram is the result of adding the $\Delta p_e < 0.15$ GeV/c cut to the previous ones.

show the x_{Bj} distribution for the ^{2}H$(e, e'p)X$ reaction with electron and proton fiducial cuts turned on. There is a clear QE peak in each panel at $x_{Bj} \approx 1$ (obscured by the green histograms that we discuss below) and a large inelastic contribution at lower x_{Bj}. Turning on the quasielastic requirement that $W_n < 1.02$ GeV generates the red histograms (also partially obscured by the green ones). The inelastic part of the spectrum is drastically reduced and the distribution is roughly symmetric about one except for a shoulder at low x_{Bj} in the 2.6-GeV, reversed torus polarity data (right-hand panel). When we apply the Δp_e cut to the distribution of Bjorken x_{Bj} we obtain the green histograms shown in Fig 11. In the right-hand panel with the reversed polarity data, the shoulder has disappeared while the data around the peak near $x_{Bj} = 1$ are unchanged. The same effect is seen for the normal polarity data in the left-hand panel. The low-x_{Bj} events have gone away while the regions near the peak and above are not affected. The impact of the Δp_e cut on A'_{LT} is limited and we study that below when we turn to the systematic uncertainty on the cut.

We also investigated the impact of another kinematic constraint on the residual mass W left behind by the scattered electron. This constraint was motivated by past experiments at Bates measuring the asymmetry $A^{fa}_{LT'}$ (recall Section 2) over a narrow range in Q^2 and

energy transfer ν [9]. The kinematics in Ref [9] correspond to a bin $\Delta\nu = 17$ MeV centered where the residual mass W is equal to the nucleon mass. Our data cover a much wider range in W as shown in Figure 12. To explore any differences with our results in the region close

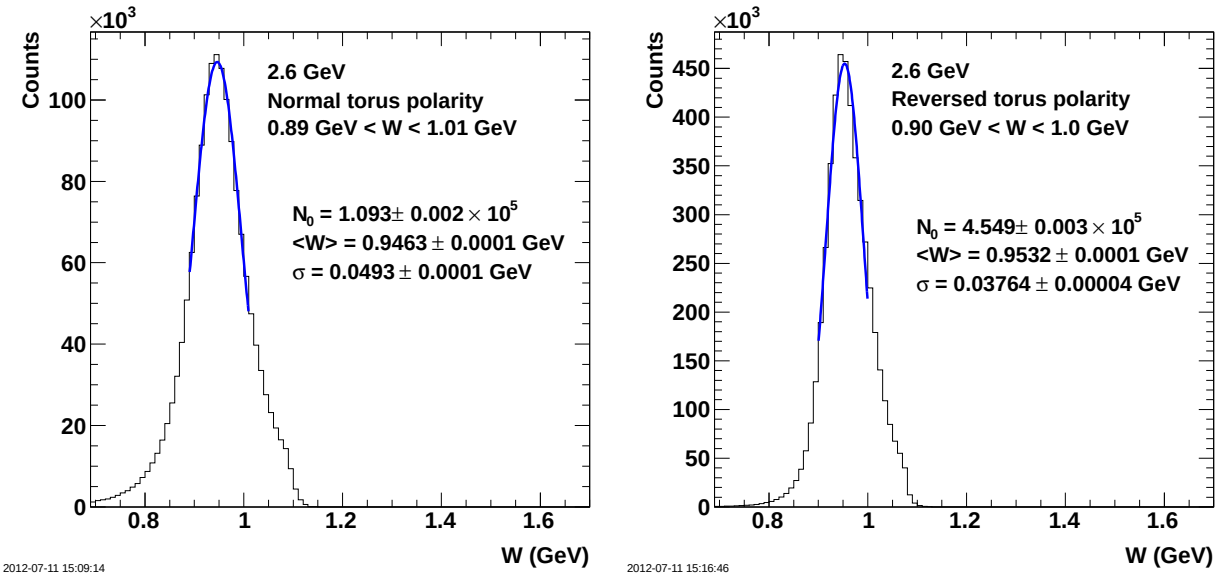

Figure 12: Distributions of the residual mass W for events that pass the cuts on W_n and Δp_e for the reversed (left-hand side) and normal (right-hand side) torus polarity data sets.

to the nucleon mass we applied a narrow cut near the top of the distributions in Figure 12. We could not use the same small width used in Ref [9] because the statistics were poor so we used a wider cut. We selected the limits of the cut by first fitting the central region of the W distribution with a Gaussian (blue curves in Figure 12) and extracting the width σ. We then placed the cut at $\pm\sigma$ relative to the average value of the fit. This cut was then added to the previous electron selection criteria described above and shown in Table 2. We discuss the impact of this cut in Sections 5.5 and in more detail in 6.5.

5.4 Proton Selection

Proton candidates were selected from positively-charged tracks in the EVNT bank in coincidence with a good electron. An additional mass cut 0.90 GeV $< m_p <$ 1.05 GeV was required where m_p is the proton mass derived from tracking and two more cuts were applied to the electron and proton track vertices. The proton vertex $v_z(p)$ was required to lie in the same range as the electron -11.5 cm $< v_z(p) < -8.0$ cm (see Figure 4) and the electron and proton vertices were required to be within 1.5 cm of one another $|v_z(e) - v_z(p)| \leq 1.5$ cm.

Proton fiducial cuts are necessary to eliminate $e - p$ coincidences where the proton is in a region near the cryostat holding the coils used to generate the CLAS magnetic field. The field in these regions is sensitive to the distance from the coils and not as well-known as the field in the more central region between the coils. We have largely followed the method described in [18] which is analogous to the technique used to determine the electron fiducials.

The details of the method are described in Appendix C and results are shown in Appendix D. The final hadron acceptance is shown in Figures 13 and 14. A summary of the criteria

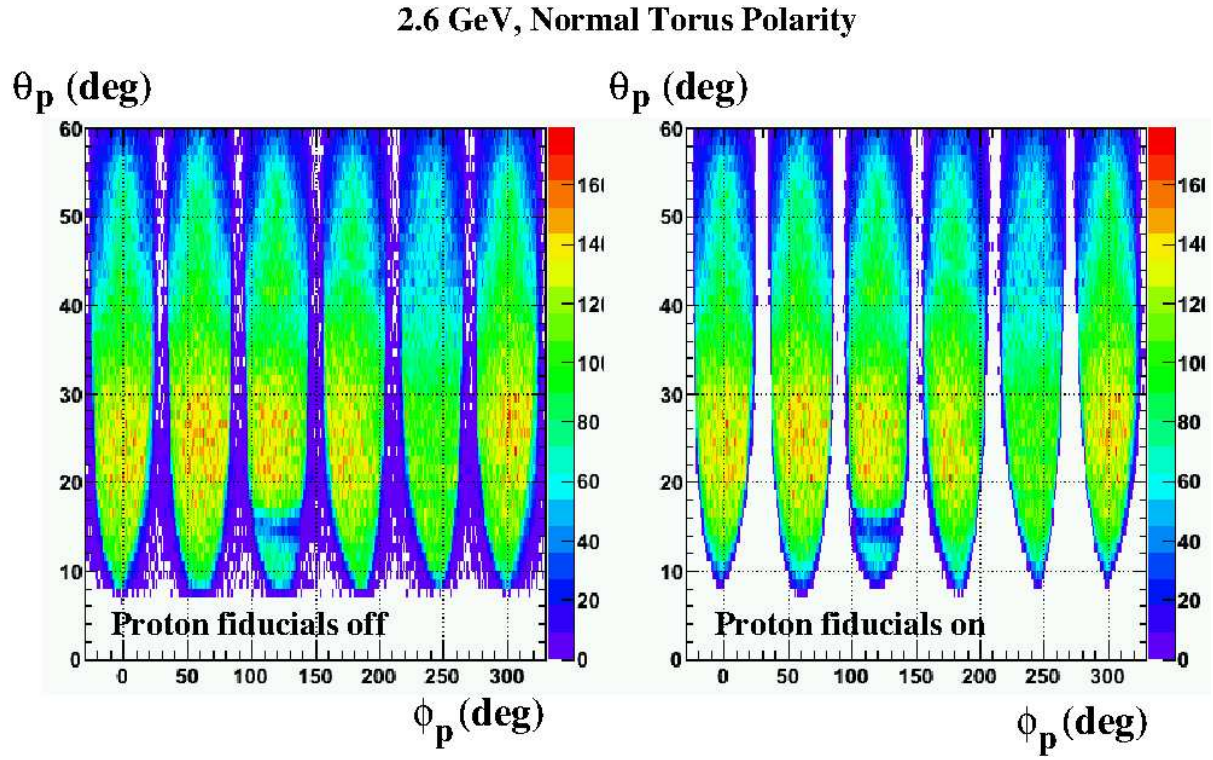

Figure 13: Hadron acceptance is shown with hadron fiducial cuts on (right-hand panel) and off (left-hand panel) for 2.6-GeV, normal-torus-polarity data set.

for identifying protons is shown in Table 3.

Description of cut	Parameters
Proton mass (m_p)	0.90 GeV $< m_p <$ 1.05 GeV
Select deuterium target (cm)	-11.5 cm $< v_z < -8.0$ cm
$e-p$ vertex separation (cm)	$\leq$ 1.5 cm
Missing mass cut (normal polarity)	0.84 GeV$^2 < MM^2 <$ 0.92 GeV^2
Missing mass cut (reversed polarity)	0.83 GeV$^2 < MM^2 <$ 0.91 GeV^2

Table 3: Hadron Identification Parameters.

5.5 Preliminary Results

We present here our preliminary results for A'_{LT} for data sets 2-3 from Table 1. We excluded data set 1 because the statistics for A'_{LT} are poor (see Figure 23 in Section 6.2.5 below). Figure 15 shows A'_{LT} defined in Equation 7 for the 2.6-GeV, normal-torus-polarity data

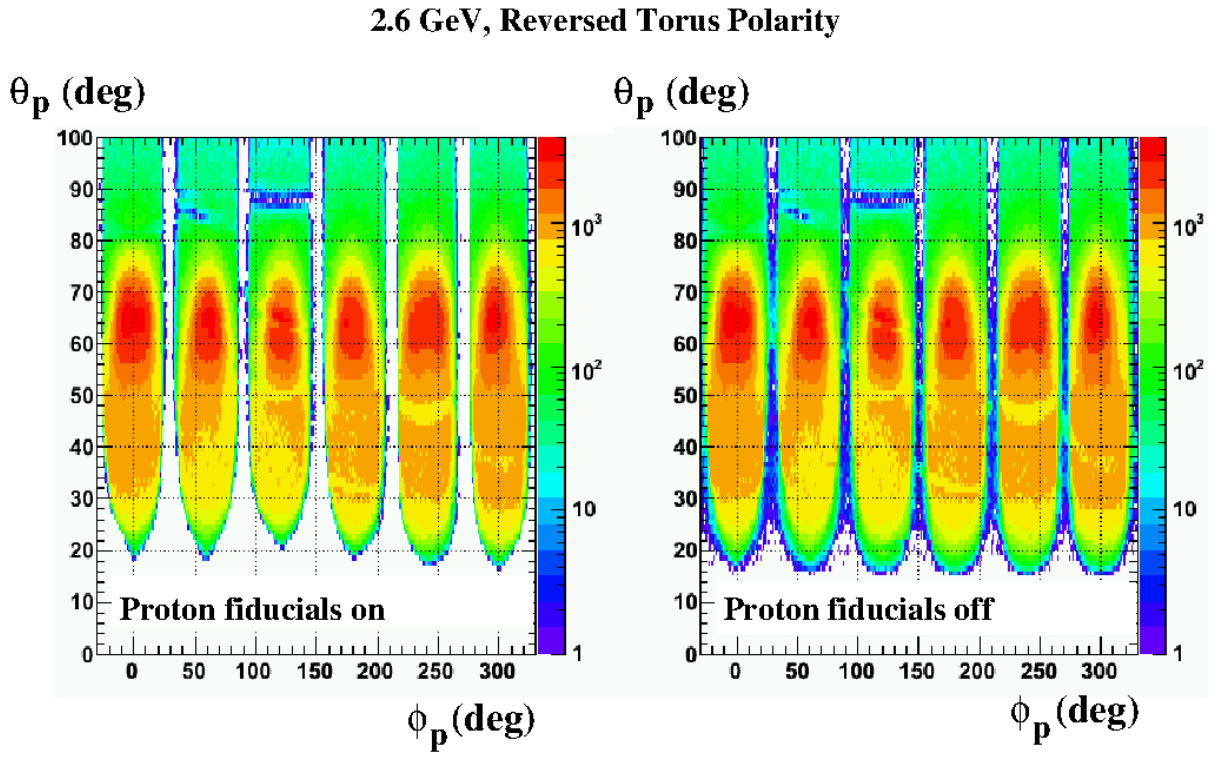

Figure 14: Hadron acceptance is shown with hadron fiducial cuts on (left-hand panel) and off (right-hand panel) for 2.6-GeV, reversed-torus-polarity data set.

(left-hand panel) and the reversed-torus-polarity (right-hand panel). The uncertainties on each point are statistical ones only. The details of extracting A'_{LT} are discussed in Sections 6.1-6.2.5. The right-hand panel of Figure 15 shows a clear, statistically significant dip in A'_{LT} centered at $p_m \approx 0.22\ GeV/c$. The reversed-torus-polarity data cover a lower Q^2 than the normal torus polarity data. The left-hand panel shows evidence of the same dip in A'_{LT}, but with lower statistics.

In Figure 16 we show A'_{LT} with the additional cut to select events with residual mass W near the nuclear mass (see Section 5.3). For the reversed torus polarity data (right-hand panel) there is little difference with or without this narrow W cut. Compare the right-hand panels in Figures 15 and 16. For the normal torus polarity data (left-hand panels in Figures 15 and 16) there is a significant change. The dip in A'_{LT} has grown by more than a factor of three. We will return to these differences in Section 6.5.

6 Experiment Results

6.1 Extracting Asymmetries

In this section we discuss in more detail the method for extracting the asymmetry A'_{LT} discussed in the Section 1. The method we use is based on measuring the weighted moments of the data to take full advantage of the large acceptance of CLAS. Recall that we wrote the

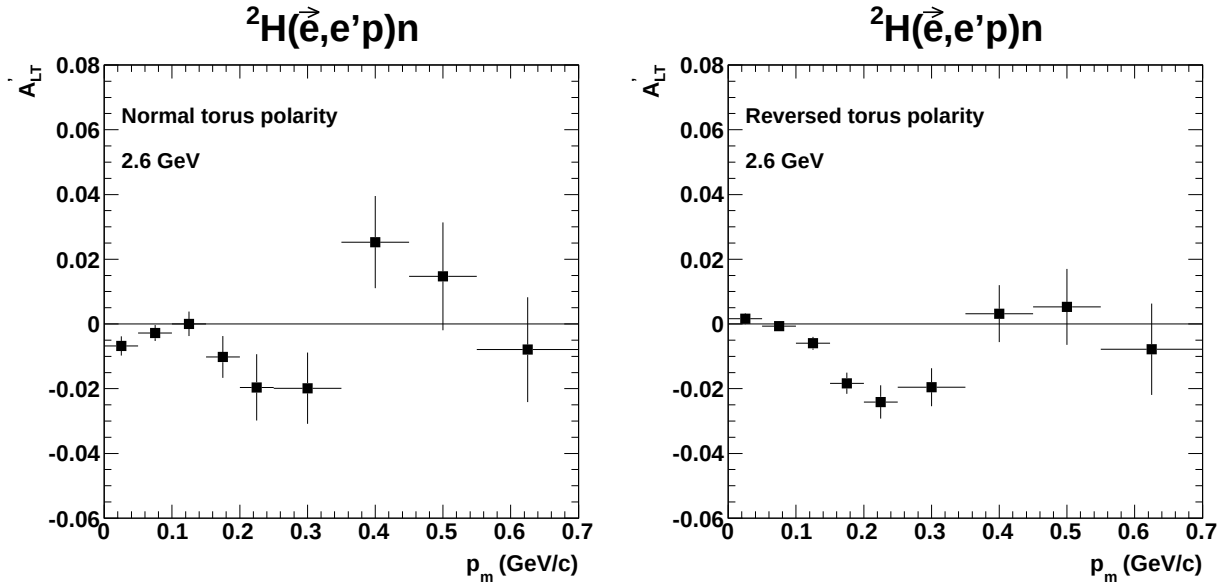

Figure 15: Preliminary results for helicity asymmetry A'_{LT} for the ^{2}H(ẽ, e′p)n reaction at 2.6 GeV with normal-polarity torus field (left-hand panel) and reversed-polarity torus field (right-hand panel).

fivefold differential cross section for the quasielastic $^2\mathrm{H}(\vec{e}, e'p)n$ reaction as

$$\frac{d^5\sigma}{d\mathrm{Q}^2 dp_m d\phi_{pq} d\Omega_e d\Omega_p} = \sigma^{\pm} = \sigma_L + \sigma_T + \sigma_{LT}\cos\phi_{pq} + \sigma_{TT}\cos 2\phi_{pq} + h\sigma_{LT'}\sin\phi_{pq} \qquad (9)$$

where the superscript on $\sigma^{\pm}$ refers to the helicity, ϕ_{pq} is defined in Figure 1, and the σ_i's are the partial cross sections for each component. First, we want to make contact with the form of the asymmetry used in Ref [9, 13, 12, 19] and shown in Figure 2. Recall the helicity asymmetry.

$$A_h(\mathrm{Q}^2, p_m, \phi_{pq}) = \frac{\sigma^+ - \sigma^-}{\sigma^+ + \sigma^-} \qquad (10)$$

Substituting Equation 9 into Equation 10 one obtains the following result.

$$A_h(\mathrm{Q}^2, p_m, \phi_{pq}) = \frac{\sigma_{LT'}\sin\phi_{pq}}{\sigma_L + \sigma_T + \sigma_{LT}cos\phi_{pq} + \sigma_{TT}\cos 2\phi_{pq}} \qquad (11)$$

If we then pick $\phi_{pq} = 90^\circ$ we obtain the fixed angle asymmetry discussed in Section 2.

$$A_h(\mathrm{Q}^2, p_m, \phi_{pq} = 90^\circ) = A^{fa}_{LT'} = \frac{\sigma^+_{90} - \sigma^-_{90}}{\sigma^+_{90} + \sigma^-_{90}} = \frac{\sigma_{LT'}}{\sigma_L + \sigma_T - \sigma_{TT}} \quad . \qquad (12)$$

This is the form of the asymmetry used in Ref [9, 13, 12, 19] and shown as $A_{LT'}$ in Figure 2. It depends on measurements at a few select angles. With CLAS we want to take full advantage of the large acceptance so we take a different approach.

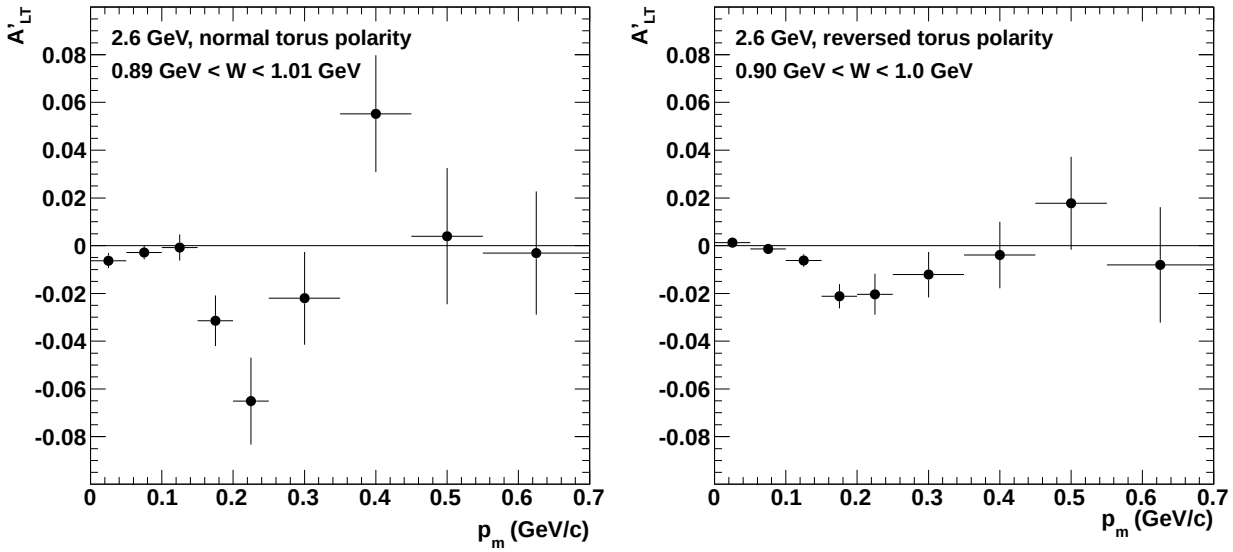

Figure 16: Helicity asymmetry A'_{LT} with the cut on the residual mass W applied in addition to the cuts discussed in Section 5.3.

Consider taking the $\sin\phi_{pq}$ moment of the cross section for the two different choices of helicity.

$$\langle \sin\phi_{pq}\rangle_{\pm} = \frac{\int_0^{2\pi}\sigma^{\pm}\sin\phi_{pq}d\phi_{pq}}{\int_0^{2\pi}\sigma^{\pm}d\phi_{pq}} \tag{13}$$

$$= \frac{\int_0^{2\pi}(\sigma_L+\sigma_T+\sigma_{LT}\cos\phi_{pq}+\sigma_{TT}\cos 2\phi_{pq}+h\sigma_{LT'}\sin\phi_{pq})\sin\phi_{pq}d\phi_{pq}}{\int_0^{2\pi}(\sigma_L+\sigma_T+\sigma_{LT}\cos\phi_{pq}+\sigma_{TT}\cos 2\phi_{pq}+h\sigma_{LT'}\sin\phi_{pq})d\phi_{pq}} \tag{14}$$

By the orthogonality of sines and cosines all of the terms disappear except for the $\sigma_{LT'}$ term in the numerator and the ϕ_{pq}-independent terms in the denominator. The result is

$$\langle \sin\phi_{pq}\rangle_{\pm} = \frac{\pm\sigma_{LT'}}{2(\sigma_L+\sigma_T)} = \frac{A'_{LT}}{2} \approx \pm\frac{A^{fa}_{LT'}}{2} \tag{15}$$

where we have used $h=\pm 1$, and made the approximation that σ_{TT} is small compared to σ_L or σ_T as has been observed [12, 20, 21]. We now use the definition of the asymmetry A'_{LT} in Equation 7 where the denominator differs from the one in Refs [9, 13, 12, 19] (see Equation 6) by neglecting the additional σ_{TT} term. For practical purposes as we will discuss later, there is no significant difference between the two definitions because σ_{TT} is small relative the σ_L and σ_T.

We now present a useful feature of $\langle \sin\phi_{pq}\rangle^{\pm}$ that can be exploited to reduce acceptance effects. In Equation 15, $\sigma_{LT'}$ depends on Q^2, p_m or θ_{pq}, and one expects to see behavior like that shown in Figure 17 below. The curve for one helicity is the opposite of the curve for the other helicity as a function of p_m. However, acceptance effects can distort the expected

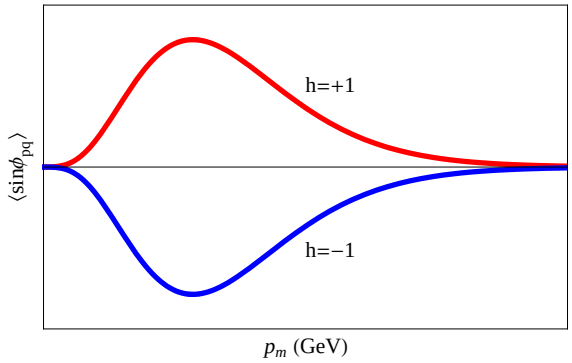

Figure 17: Schematic drawing showing the possible results for $\langle \sin \phi_{pq} \rangle^{\pm}$ with no acceptance effects.

distributions of Equation 15 if the CLAS acceptance has a component that varies as $\sin \phi_{pq}$. In such a case this experimental artifact will survive the integration in Equation 14 when it is multiplying the constant portion of the cross section (σ_L and σ_T terms in Equation 14). Such an acceptance effect is additive and shifts $\langle \sin \phi_{pq} \rangle_{\pm}$ up or down, so

$$\langle \sin \phi_{pq} \rangle_{\pm} = \pm \frac{\sigma_{LT'}}{2(\sigma_L + \sigma_T)} + \alpha \tag{16}$$

where α is the additive acceptance correction. See Appendix E for more details. If one has measured this $\sin \phi_{pq}$ moment for each helicity then the results can be combined so

$$\langle \sin \phi_{pq} \rangle_{+} - \langle \sin \phi_{pq} \rangle_{-} = \frac{\sigma_{LT'}}{\sigma_L + \sigma_T} = A'_{LT} \tag{17}$$

and

$$\frac{\langle \sin \phi_{pq} \rangle_{+} + \langle \sin \phi_{pq} \rangle_{-}}{2} = \alpha \quad . \tag{18}$$

The asymmetry A'_{LT} can be extracted with reduced sensitivity to acceptance effects and the $\sin \phi_{pq}$-dependent acceptance effects have been measured from the data. This technique has been used by others for the $p(\vec{e}, e'\pi^+)n$ and $p(\vec{e}, e'p)\pi^0$ reactions [22, 23].

Finally, to extract A'_{LT} we will use the $\sin \phi_{pq}$-weighted moments of the data corrected for the beam polarization P_e and beam charge asymmetry A_Q so

$$A'_{LT} = \frac{1}{P_e A_Q} \left(\langle \sin \phi_{pq} \rangle^m_+ - \langle \sin \phi_{pq} \rangle^m_- \right) \tag{19}$$

and $\langle \sin \phi_{pq} \rangle_{\pm}$ is defined by Equation 13 and subject to the cuts described in Section 5.

To determine $\langle \sin \phi_{pq} \rangle_{\pm}$ from the data for a given bin in Q^2 consider Equation 13. The denominator is proportional to the number of events one observes and the numerator is proportional to the sum of all the values of $\sin \phi_{pq}$. In other words,

$$\langle \sin \phi_{pq} \rangle_{\pm} = \frac{1}{N_{\pm}} \sum_{i=1}^{N_{\pm}} \sin \phi_i \tag{20}$$

Sector	Uncorrected (GeV^2)		Corrected(Lachniet) (GeV^2)	
	$\langle W^2 \rangle$	$\Delta(W^2)$	$\langle W^2 \rangle$	$\Delta(W^2)$
1	0.866	0.023	0.879	0.028
2	0.853	0.027	0.875	0.032
3	0.829	0.043	0.866	0.018
4	0.860	0.027	0.877	0.027
5	0.861	0.025	0.877	0.024
6	0.864	0.025	0.876	0.029
Average	0.855	0.029	0.875	0.027

Table 4: Effect of momentum corrections on the average value and width of W^2 peak for *ep* elastic scattering for the 2.6-GeV, reversed-torus-polarity data.

where the sum is over the ϕ_{pq} distribution of the data, i's refer to individual events, and $N_{\pm}$ refers to the number of events of each helicity.

6.2 Corrections

6.2.1 Momentum Corrections

Misalignments of the CLAS drift chambers in each sector and uncertainties in the magnetic field produced by the CLAS torus can lead to inaccuracies in measuring the momentum of charged particles. To correct for these inaccuracies, we used the method described by J.Lachniet in Ref [14] and pioneered by V. Burkert. This technique relies on elastic scattering from the proton in the E5, dual target. For elastically scattered electrons we determine θ_e for the electron and calculate W^2, the square of the mass of the residual object which is a proton here. The difference between W^2 and the square of the proton mass is minimized to determine a correction factor to the electron momentum as a function of the electron θ_e and ϕ_e and for each data set.

The effect of the momentum corrections for the 2.6-GeV, reversed-torus-polarity data on the centroid and width of the proton peak in the W^2 spectrum is shown in Table 4 sector by sector. The first feature of Table 4 to notice is the E5 data are well calibrated to start. The uncorrected proton peak is, on average, 3% below the expected value. Applying the momentum corrections, the proton peak moves to 0.6% below the expected value. The Lachniet method reduces the width of the proton peak by 7%.

The effect of the momentum corrections on the 2.6-GeV, normal-torus-polarity data on the centroid and width of the proton peak in the W^2 spectrum is shown in Table 5. Again, the E5 data is well calibrated; the uncorrected proton peak is only about 1% below the expected value. The Lachniet method improves the agreement with the proton mass to 0.2% and reduces the width of the distribution by about 18%.

For completeness we show the results for the 4.2-GeV data set in Table 6. As we show in Figure 23, we found the statistical uncertainty on the fifth structure function asymmetry $A_{LT'}$ is poor. The E5 data is again well calibrated; the uncorrected proton peak is only about 2% below the expected value. The Lachniet method improves the agreement with the proton mass to 0.8% and reduces the width of the distribution by 25%.

Sector	Uncorrected (GeV^2)		Corrected(Lachniet) (GeV^2)	
	$\langle W^2 \rangle$	$\Delta(W^2)$	$\langle W^2 \rangle$	$\Delta(W^2)$
1	0.870	0.034	0.879	0.028
2	0.839	0.045	0.877	0.027
3	0.887	0.033	0.881	0.028
4	0.872	0.030	0.879	0.028
5	0.874	0.031	0.879	0.029
6	0.889	0.029	0.881	0.030
Average	0.871	0.034	0.879	0.028

Table 5: Effect of momentum corrections on the average value and width of W^2 peak for *ep* elastic scattering for the 2.6-GeV, normal-torus-polarity data.

Sector	Uncorrected (GeV^2)		Corrected(Lachniet) (GeV^2)	
	$\langle W^2 \rangle$	$\Delta(W^2)$	$\langle W^2 \rangle$	$\Delta(W^2)$
1	0.849	0.048	0.874	0.033
2	0.832	0.053	0.865	0.033
3	0.893	0.037	0.877	0.034
4	0.858	0.041	0.873	0.030
5	0.864	0.042	0.872	0.030
6	0.885	0.035	0.875	0.031
Average	0.863	0.043	0.873	0.032

Table 6: Effect of momentum corrections on the average value and width of W^2 peak for *ep* elastic scattering for the 4.2-GeV, normal-torus-polarity data.

To conclude, we find the E5 data set is well calibrated at the start. The Lachniet method reduces the discrepancy with the proton mass in the W^2 spectrum from 1-3% depending on which data set is used down to 0.8% or less. The width of the proton peak in the W^2 distribution is reduced by 7-25%.

6.2.2 Beam Charge Asymmetry

To measure the helicity-dependent charge asymmetry of the electron beam we used the ratio of inclusive, elastic *ep* scattering from the E5 proton target to measure the quantity

$$A_Q = \frac{N^+}{N^-} \tag{21}$$

where $N^{\pm}$ is the number of elastic scattering events from the proton target for each helicity. The inclusive cross section has no helicity dependence and is more reliable than the Faraday cup readings [24]. All electron selection cuts were applied. We selected elastic events by requiring that 0.89 GeV $< W <$ 0.99 GeV and took the ratio of the results for the different beam helicity states. The results are shown in Table 7. The half-wave plate which determines the beam helicity was fixed during the E5 run period and, as expected, no shifts were observed in the helicity during the run.

Data set	A_Q
2.6-GeV, reversed torus polarity	0.9936 ± 0.0007
2.6-GeV, normal torus polarity	0.9954 ± 0.0007
4.2-GeV, normal torus polarity	0.9987 ± 0.0009

Table 7: Beam charge asymmetries for different helicity states for the E4 data set.

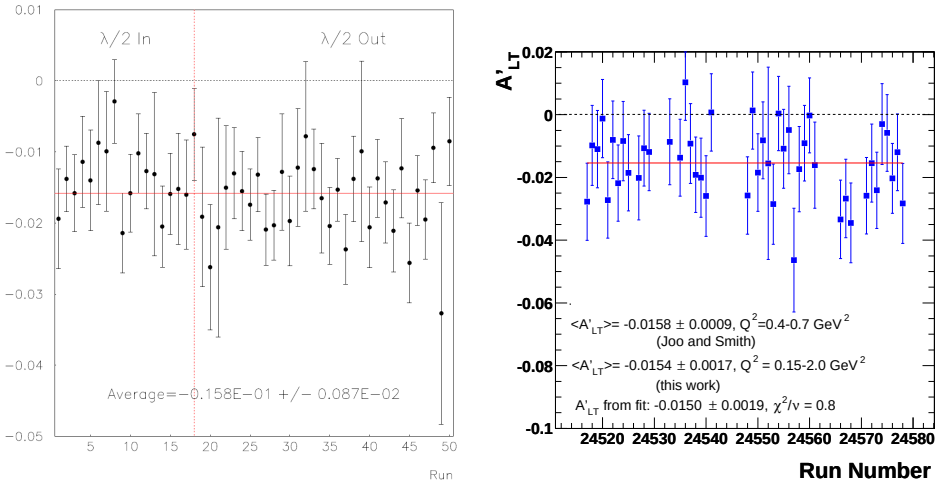

Figure 18: Comparison of helicity asymmetry for $p(\vec{e}, e'p)\pi^0$ measured previously in CLAS (left-hand panel) by Joo and Smith ([23]) and during the E5 run (right-hand panel)

6.2.3 Beam Polarization

The beam polarization was monitored during the E5 run using the Hall B Moeller polarimeter. The polarization is measured by observing asymmetries in the yields of beam electrons scattered from electrons in a polarized iron target with polarization components parallel and anti-parallel to the beam direction. This method was used seven times during the E5 run and an average polarization $P_e = 0.736 \pm 0.017$ was obtained.

To check the sign of the beam helicity we extracted the helicity asymmetry A'_{LT} from the $p(\vec{e}, e'p)\pi^0$ reaction from the proton target. This reaction has a large asymmetry and has been measured in CLAS [23] so it serves as a clear test of understanding of the sign of the helicity. The results are shown in Figure 18. Our results agree with the ones from Joo and Smith in sign and magnitude [23].

6.2.4 Radiative Corrections

The measurements of the $^2\mathrm{H}(\vec{e}, e'p)n$ reaction in this analysis are subject to radiative corrections. We are using a version of the program EXCLURAD written by Afanasev, *et al.* and modified for the $^2\mathrm{H}(\vec{e}, e'p)n$ reaction to perform those calculations [25]. This code applies a more sophisticated method than the usual approach of Mo and Tsai or Schwinger and takes into account the exclusive nature of our measurements [26, 27]. This work is described in Ref [28, 29] and in Appendix F. It was expected that the difference between the polarized

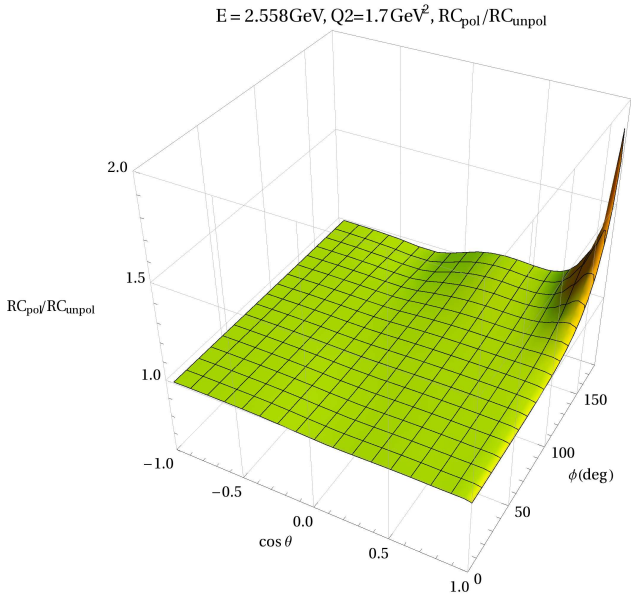

Figure 19: Ratio of polarized to unpolarized radiative correction at $Q^2 = 1.7$ GeV^2 calculated with EXCLURAD.

and unpolarized radiative corrections (RC) would be small ($RC_{pol}/RC_{unpol} \approx 1$) so that in the ratio used to extract A'_{LT} there would be little difference and the correction could be ignored. This was observed in the analysis of the G_M^n experiment using the same data [30]. However, in this case that is not completely true in certain kinematic regions. Figure 19 shows the ratio RC_{pol}/RC_{unpol} for $Q^2 = 1.7$ GeV^2. At $\cos\theta_{pq} \approx 1$ and ϕ_{pq} close to 180° the difference between the two RCs is almost a factor of two. Even when averaging these ratios over ϕ_{pq} we find differences of the order of 4-8% as shown in Figure 20. Because of these differences we corrected A'_{LT} for radiative effects.

The radiative corrections were performed in the following way (1) Radiative corrections were calculated for polarized and unpolarized events as a function of $\cos\theta_{pq}$ and ϕ_{pq} with EXCLURAD at the following values of Q^2: 0.2, 0.5, 0.8, 1.1, 1.4, 1.7 (GeV^2). These calculations cover the full data range for the $2.6-$GeV data sets (see right-hand panel of Fig. 23 below) where there is a significant cross section. (2) The dependence on $\cos\theta_{pq}$ was converted to p_m using the method described in Ref. [31]. (3) These $p_m - \phi_{pq}$ surfaces were stored in two, three-dimensional histograms (polarized and unpolarized) in our ROOT analysis code. (4) We applied each correction as a weight on an event-by-event basis for a given Q^2, p_m, and ϕ_{pq} when we incremented the analysis histograms used to extract the helicity asymmetry. This weight was the inverse of the correction calculated by EXCLURAD and the values of the corrections were interpolated between the Q^2 points in the histograms. The polarized correction was applied in the histogram used to extract the numerator in Equation 20. The unpolarized correction was applied to the histogram used to extract the denominator in Equation 20. The effect of the correction on A'_{LT} for the normal-torus-polarity data is shown in the left-hand panel of Figure 21 which displays the asymmetry with (red) and without

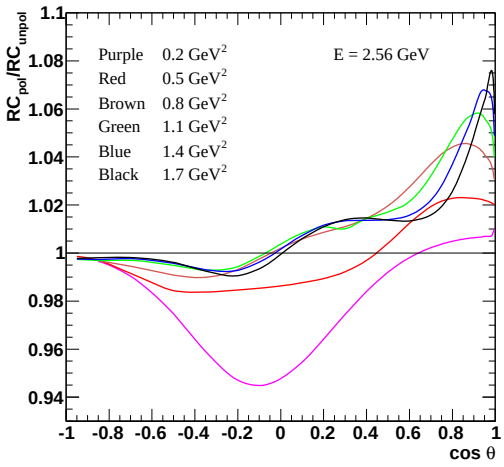

Figure 20: Radiative correction for A'_{LT} averaged over ϕ_{pq} for different values of Q^2. A full set of plots for all Q^2 are in Appendix G.

(black) the correction in the left-hand panel. The effect is much smaller than the statistical uncertainty. In the right-hand panel of Figure 21 the difference between the corrected and uncorrected asymmetries is shown.

The same corrections were applied to the 2.6-GeV, reversed-torus-polarity data. The left-hand panel of Figure 22 shows the helicity asymmetry with (red) and without (black) the radiative correction applied. The difference between the two asymmetries in shown in the right-hand panel of Figure 22. The effect of the radiative correction turns out to be small in the ratio.

6.2.5 Results for Asymmetries

In Fig 23 we show our results for the asymmetry $A_{LT'}$ for all three sets of running conditions from the E5 running period. The data are integrated over the full Q^2 range for each set of running conditions to get adequate statistics so we have included the Q^2 distribution in parallel with the asymmetry for each data set. The 2.6-GeV, reversed torus field data show a very clear dip to $A'_{LT} \approx -0.025$ at $p_m = 0.23$ GeV/c followed by a rise back to zero at larger missing momentum. The same general features are seen in the 2.6-GeV, normal torus field data at higher Q^2 with larger statistical uncertainties. The 4.2-GeV has large statistical uncertainties over most of the p_m range (note the change of scale) and so there are few conclusions to be drawn from these data.

In Figure 24 we show our results for the background asymmetry α defined in Equation 18. The background asymmetries are about the same magnitude as the features in the $A_{LT'}$ distributions which emphasizes the importance of the use of the difference between the asymmetries extracted from the opposite helicities to eliminate this background.

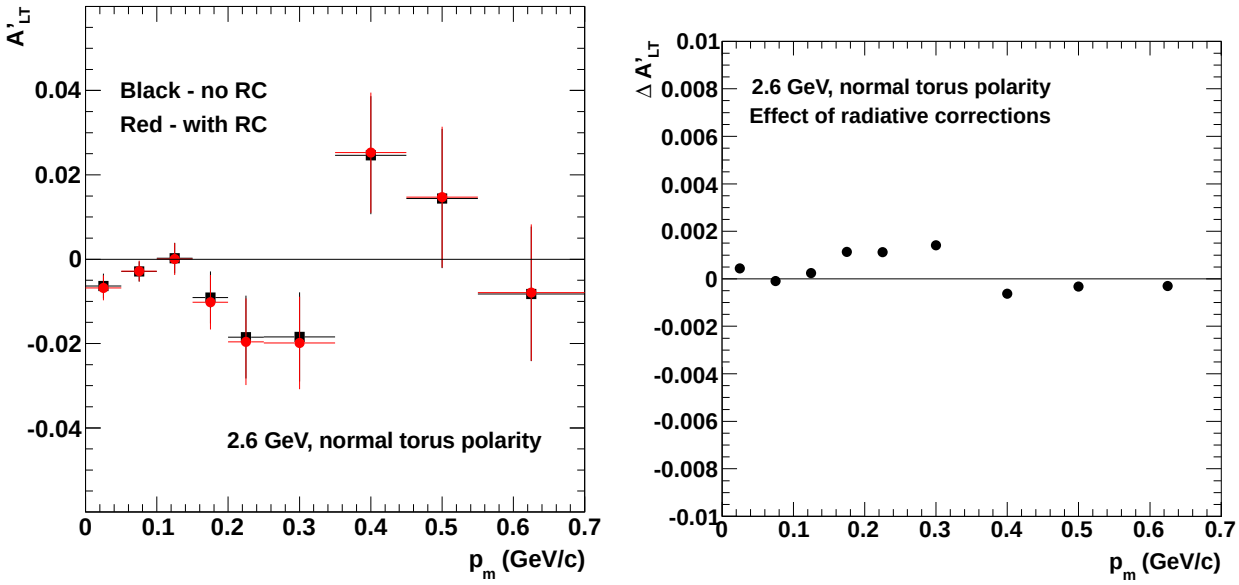

Figure 21: The effects of radiative corrections on A'_{LT} for 2.6-GeV, normal-torus-polarity data.

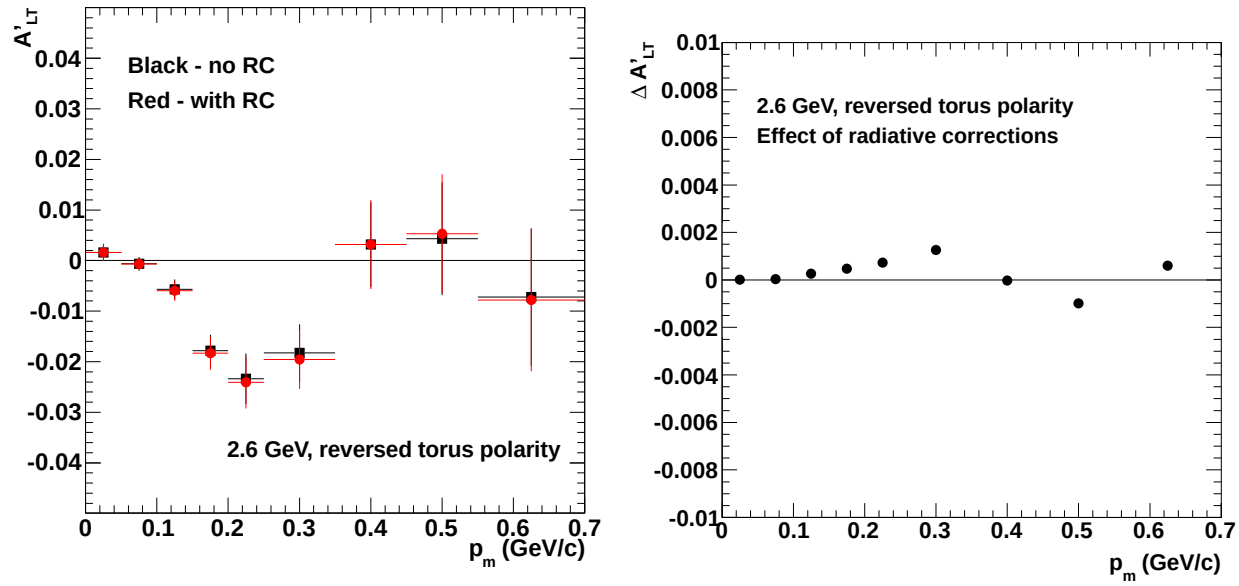

Figure 22: The effects of radiative corrections on A'_{LT} for 2.6-GeV, reversed-torus-polarity data.

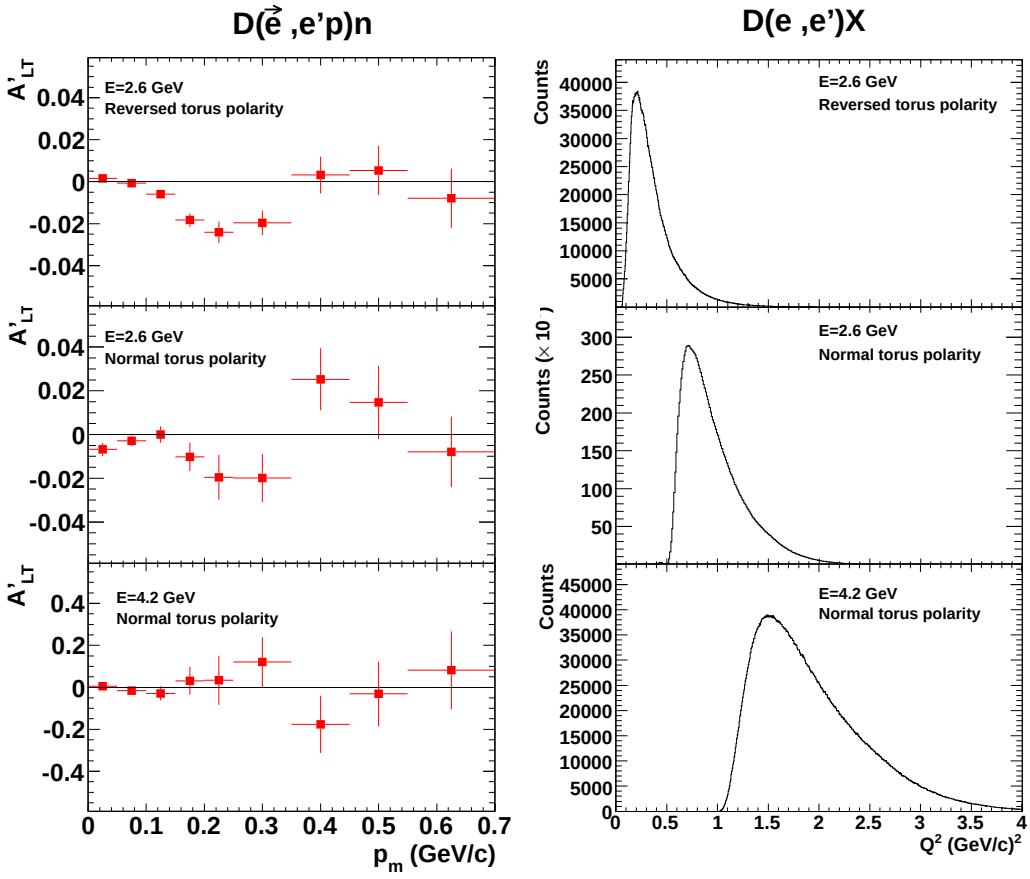

Figure 23: The left-hand column shows the results for A'_{LT} for the 2.6-GeV, reversed torus polarity data (top panel), the 2.6-GeV, normal torus polarity data (middle panel), and the 4.2-GeV, normal torus polarity data (bottom panel). The right-hand column shows the Q^2 spectrum for each data set. The asymmetries were summed over all Q^2. The uncertainties are statistical only.

6.3 Consistency Checks of the Analysis

We now present the results of a series of consistency checks of our results to test our analysis algorithms.

6.3.1 Asymmetry at $p_m \approx 0$

The first test is the behavior of A'_{LT} at small missing momentum p_m or small θ_{pq}. We expect the asymmetry to go to zero in this region. To understand this recall the helicity asymmetry $A_h(Q^2, p_m, \phi_{pq})$ in Equation 11. For fixed Q^2, W^2, and p_m, the only kinematic dependence is on $\sin\phi_{pq}$ (the ϕ_{pq}-dependent parts in the denominator are small compared to the constant ones) and the asymmetry will disappear if one averages over all ϕ_{pq}. Now consider $A_h(Q^2, p_m, \phi_{pq})$ at small p_m. The sinusoidal dependence is compressed into a small

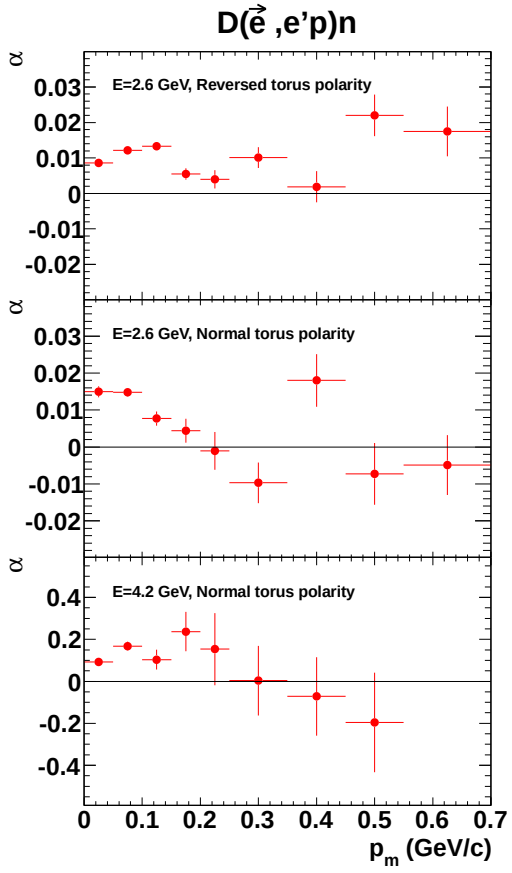

Figure 24: The background asymmetry α for the 2.6-GeV, reversed torus polarity data (top panel), the 2.6-GeV, normal torus polarity data (middle panel), and the 4.2-GeV, normal torus polarity data (bottom panel). The asymmetries were summed over all Q^2. The uncertainties are statistical only.

cone around the 3-momentum transfer $\vec{q}$. In the limit of small p_m and the finite resolution of our detector, we will be averaging over the entire $\sin\phi_{pq}$ part which will go to zero. The amplitude of $A_h(Q^2, p_m, \phi_{pq})$ is A'_{LT} as long as the σ_{LT} and σ_{TT} components in the denominator of Equation 11 are small relative to σ_L and σ_T (we show this later). In addition, since we are taking the difference between $\langle\sin\phi_{pq}\rangle$ for different beam helicities, the low p_m behavior is also a test of the accuracy of the beam charge asymmetry.

Our data are consistent with this behavior within the statistical uncertainty. See Figure 23 and focus on the first bin in each distribution of A'_{LT} (left-hand column). In Table 8 we list the results in that first bin. The results overlap with zero within the uncertainties except the 2.6-GeV, normal torus polarity result which is about two standard deviations low. To study this issue more carefully we examined A'_{LT} in finer steps at small p_m for the 2.6-GeV data. The results for the normal-torus-polarity data are shown in the left-hand panel of Figure 25. At the smallest p_m, we have limited statistics, but the small p_m behavior is consistent

Data Set	A'_{LT}
2.6 GeV, reversed polarity	0.0016 ± 0.0017
2.6 GeV, normal polarity	-0.0068 ± 0.0030
4.2 GeV, normal polarity	-0.003 ± 0.019

Table 8: Asymmetry in the first p_m bin for each data set. In each case this bin covers the range $p_m = 0.0 - 0.05$ GeV.

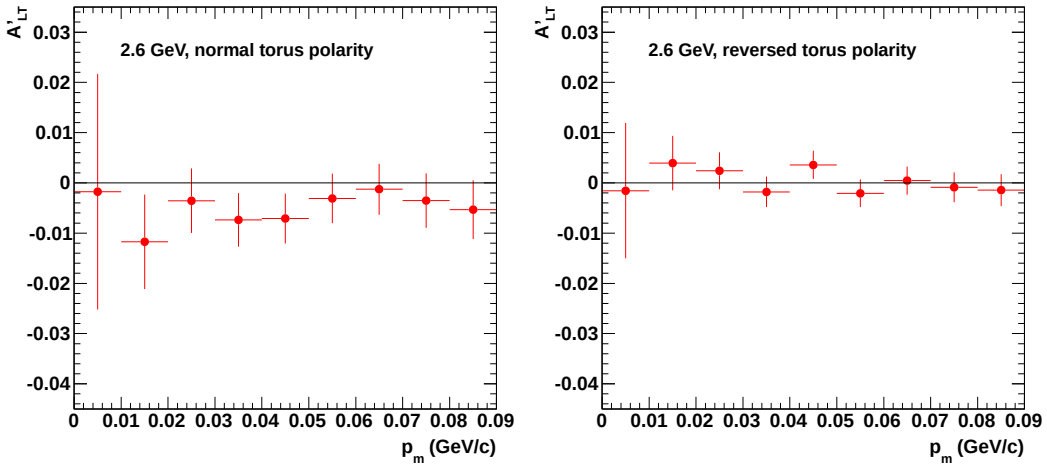

Figure 25: Helicity asymmetry for the 2.6-GeV, normal (left-hand panel) and reversed (right-hand panel) torus polarity data at small p_m where the asymmetry is expected to go to zero.

with zero within the experimental uncertainties. The average of the first three points in the left-hand panel of Figure 25 (the normal torus polarity data) is -0.0057 ± 0.0052 versus 0.0013 ± 0.0016 for the right-hand panel (the reversed torus polarity data).

To further study this question one needs better statistics. We can add statistics here by removing the electron and proton fiducial cuts. These restrictions eliminate events that are suspect because they are in an angular region near the edge of the sector where the magnetic field is changing rapidly and is not well known. The reconstructed momenta are not trustworthy. This implies the identification of quasielastic events may not be valid, but the helicity asymmetry extracted from those events should still go to zero at low p_m. We show the 2.6-GeV, normal helicity asymmetry with the fiducial cuts off in Figure 26. At the lowest missing momentum bin the asymmetry is 0.0009 ± 0.0022; consistent with zero. Within the experimental uncertainties the asymmetry A'_{LT} shows the correct behavior near $p_m = 0$ for both 2.6-GeV data sets.

6.3.2 Extracting A'_{LT} by Fitting the ϕ_{pq} Dependence

We investigated another method for extracting A'_{LT} that also takes advantage of the large acceptance of CLAS. Recall the expression for $A_h(\mathrm{Q}^2, p_m, \phi_{pq})$ (see Equation 11) which is

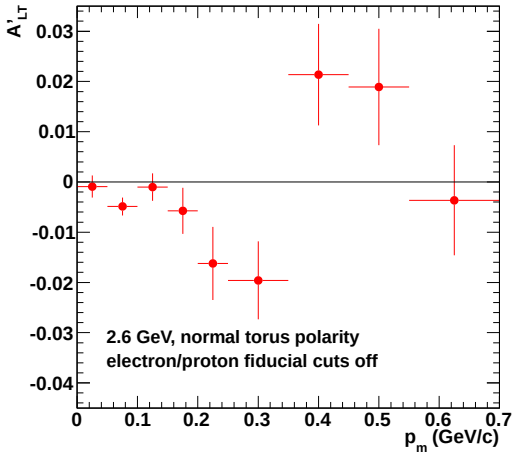

Figure 26: Helicity asymmetry for the 2.6-GeV, normal torus polarity data with electron and proton fiducial cuts off.

reproduced here.

$$A_h(\mathrm{Q}^2, p_m, \phi_{pq}) = \frac{\sigma_{LT'} \sin\phi_{pq}}{\sigma_L + \sigma_T + \sigma_{LT} cos\phi_{pq} + \sigma_{TT} \cos 2\phi_{pq}} \tag{22}$$

The numerator in Equation 22 is proportional to $\sin(\phi_{pq})$ and the denominator is approximately constant as long as σ_{LT} and σ_{TT} are small. If one forms the following ratio of different helicities

$$A(\mathrm{Q}^2, p_m, \phi_{pq}) = \frac{\sigma^+ - \sigma^-}{\sigma^+ + \sigma^-} = \frac{N_+ - N_-/A_Q}{N_+ + N_-/A_Q} = \frac{\sigma'_{LT} \sin\phi_{pq}}{\sigma_L + \sigma_T + \sigma_{LT} cos\phi_{pq} + \sigma_{TT} \cos 2\phi_{pq}} \tag{23}$$

where A_Q is the beam charge asymmetry, then the distribution should have a sinusoidal dependence on ϕ if σ_{LT} and σ_{TT} are small relative to σ_T and σ_L. In other words,

$$A(\mathrm{Q}^2, p_m, \phi_{pq}) \approx \frac{\sigma'_{LT} \sin\phi_{pq}}{\sigma_L + \sigma_T} = A'_{LT} \sin\phi_{pq} \tag{24}$$

so the amplitude of the asymmetry is A'_{LT}. We can fit this distribution and compare that fit with our results using the $\sin\phi_i$-weighted distributions. We have calculated this ratio and the results are shown in Figure 27 for four different bins in θ_{pq} in the range $\mathrm{Q}^2 = 0.8 - 1.0$ $(\mathrm{GeV/c})^2$ for the 2.6-GeV, normal torus polarity data set. The distributions were fitted with a sine curve without the small LT and TT contributions and the results are shown on the figure. The fits all have acceptable reduced χ^2. We also tried fitting a more complex function that included the $\cos\phi_{pq}$ and $\cos 2\phi_{pq}$ terms in the denominator of Equation 11. We found the contributions from σ_{LT} and σ_{TT} were consistent with zero and there was no significant improvement to the fit.

We compared the two different methods for measuring A'_{LT} and show the results in Figure 28. The top panel shows the angular distribution in θ^{cm}_{pq} measured using the $\sin\phi_{pq}$

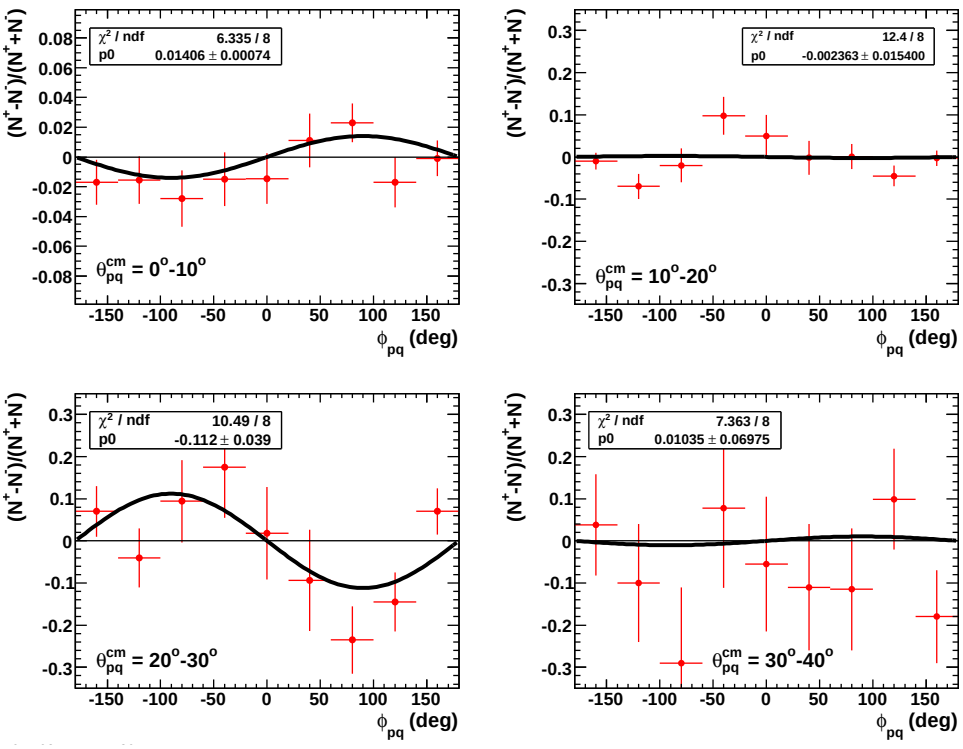

Figure 27: Results for ϕ dependence of A'_{LT} using the helicity ratio technique.

moments of the distribution and the lower panel is from the fits to $A(Q^2, \theta_{pq}, \phi_{pq})$. The results in Figure 28 are for the range $Q^2 = 0.8 - 1.0$ (GeV/c)^2. The two results are consistent with each other. The values of A'_{LT} in each angle bin agree for both methods as well as the size of the uncertainties in each angle bin. It is worth noting how A'_{LT} goes from small and positive for $\theta^{cm}_{pq} = 0° - 10°$ to large and negative for $\theta'_{pq} = 20° - 30°$. This is clearly seen in the shapes of the ϕ_{pq} distributions in Figure 27 in the upper-left and lower-left panels. We expect the $\sin\phi_{pq}$ moments and the $A(\phi_{pq})$ methods to be consistent; they represent the same quantity extracted from the same data set. We conclude that these methods are consistent and the $\sin\phi_{pq}$ moments analysis and the fit to $A(\phi_{pq})$ are equivalent methods. We have used the $\sin\phi_{pq}$ moments results throughout this Analysis Note.

6.3.3 Monte Carlo Simulations

We have tested our analysis codes in simulation to validate their accuracy and support the expectation that using a ratio to extract A'_{LT} should be independent of acceptance corrections. We put a known asymmetry similar to the observed one into the event generator, ran the CLAS standard simulation GSIM, and then analyzed the results with the same codes we used to analyze the data. If we recover the original, known asymmetry, we validate our analysis. We started with the event generator QUEEG [14] which includes elastic scattering and the effect of the Fermi motion of the nucleons in deuterium. The code is described in Appendix H. We modified the original code to include a part that depended on $\sin\phi_{pq}$

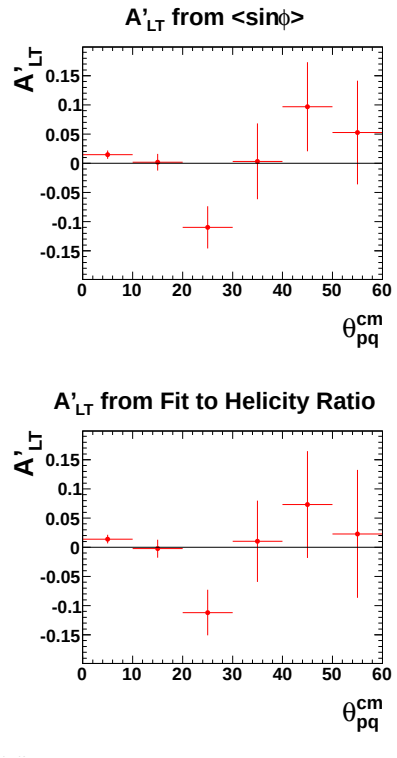

Figure 28: Comparison of A'_{LT} extracted using different analysis techniques.

with an amplitude controlled by the user. The goal here is to control the size of the $\sin(\phi_{pq})$ dependent part of the $^2\mathrm{H}(e,e'p)n$ cross section so we can compare the value used in the event generator with the final results of the analysis chain. Here, we summarize how QUEEG generates events with no asymmetry.

1. The magnitude of the Fermi momentum of the proton is picked from the Hulthen distribution and given a random direction in the laboratory frame.

2. Transform to the (now moving) rest frame of the proton and calculate a new beam energy for the incoming electron relative to this new rest frame of the proton.

3. The angle of the scattered electron is selected based on the cross section for elastic scattering at this new electron energy.

4. The momentum of the scattered electron is transformed from the proton rest frame into the lab frame.

5. To maintain energy conservation determine the scattered electron energy for the $^2\mathrm{H}(e,e'p)n$ reaction using the known momentum of the neutron (*i.e.* the negative of the Fermi momentum of the proton chosen in step 1 above). The neutron is treated as a spectator.

6. Calculate $\vec{q}$ (3-momentum transfer) and p_p (proton 3-momentum) in the lab for this quasi-elastic scattering.

7. Randomly select the lab azimuthal angle of the electron (ϕ_e) and rotate the 3-vectors for the momentum transfer, proton, and scattered electron momenta.

To include a known asymmetry the selection of the angle ϕ_{pq} is altered. The angle ϕ_{pq} is between the scattering plane (defined by the incoming and outgoing electron 3-momenta) and the reaction plane (defined by the proton and momentum transfer 3-vectors) (see Figure 1). The modifications are made to step 7 above. They are described below.

1. The direction of the momentum transfer, the magnitude of the proton 3-vector, and the angle θ_{pq} are unchanged.

2. The missing momentum is calculated based on the known momentum of the beam, scattered electron and proton. This is the same as the neutron momentum mentioned in step 5 above.

3. The coordinates are rotated so that the z-axis is now in the direction of the 3-momentum transfer $\vec{q}$. The y-axis stays the same for this new coordinate system and the lab system.

4. A new ϕ_{pq} is randomly generated based on a sinusoidal distribution with an amplitude that depends on the magnitude of the missing momentum. The amplitude is a function of p_m derived from a fit to the measured asymmetry A'_{LT} as shown in Figure 29. The

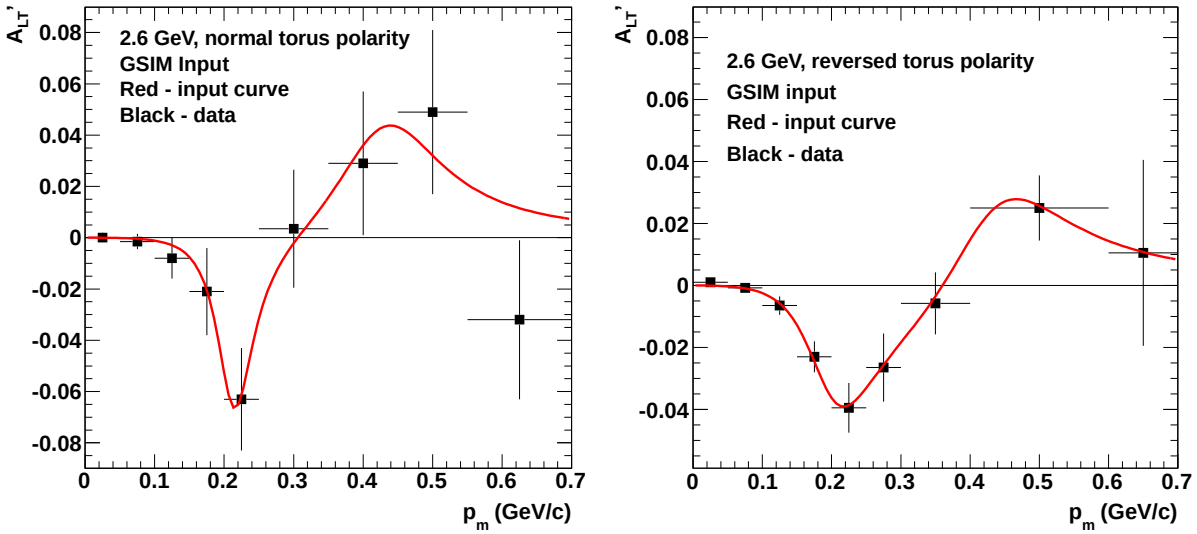

Figure 29: Plots of measured helicity asymmetry A'_{LT} and fitted curves for normal torus polarity (left-hand panel) and reversed torus polarity (right-hand panel).

fits are to the equation

$$A'^{in}_{LT} = \frac{a_1 p_m^2 + a_2 p_m^4}{1 + a_3 p_m + a_4 p_m^2 + a_5 p_m^4 + a_6 p_m^6} \tag{25}$$

where for the normal and reversed torus polarities are shown in Table 9.

Data set	a_1	a_2	a_3	a_4	a_5	a_6
normal torus polarity	-0.0344	0.3204	-11.15	35.47	-119.2	227.0
reversed torus polarity	0.0653	0.5031	-11.03	36.09	-126.7	256.1

Table 9: Best-fit coefficients for Equation 25 for normal and reversed torus magnet polarity.

5. A new missing momentum 3-vector is calculated with the same magnitude as in part 1, but with a different ϕ_{pq} using the result of part 4.

6. The coordinate system is now rotated back to the lab coordinate system with the z-axis along the beam.

7. A new, proton 3-vector is calculated using momentum conservation and the original beam, target, and scattered electron momenta and the modified neutron momentum.

Figure 30 below shows the results from using this modified version of QUEEG and extracting A'_{LT} from simulated events analyzed with the same codes used for the data analysis. The fits $A'^{\,in}_{LT}$ to the measured asymmetries are the red curves in each panel of Figure 30 and serve as the inputs for A'_{LT} in the simulation. These curves can be compared to the results extracted from the simulation with that original function (the black 'data' points in Figure 30). To make a better comparison between the input to GSIM and the simulated results,

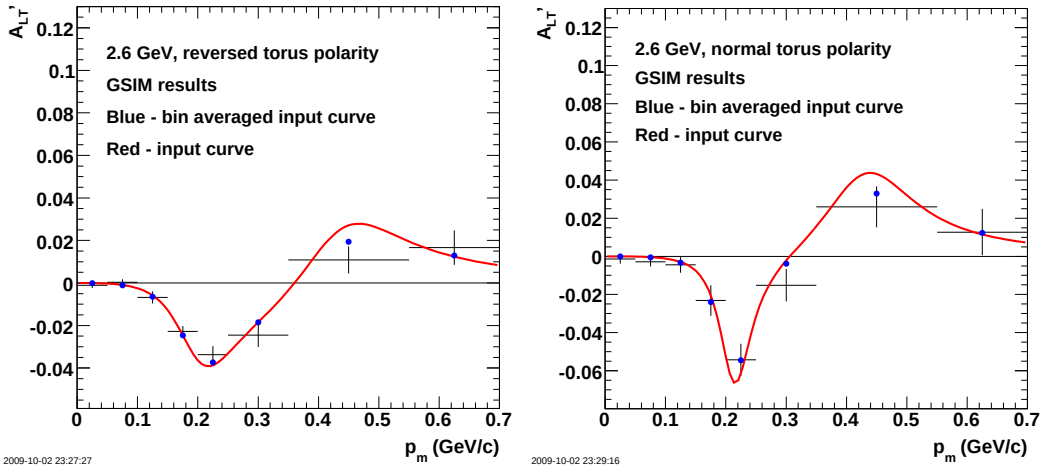

Figure 30: Comparison of GSIM-simulated A'_{LT} with 'true' asymmetry used as input to the code for 2.6-GeV, reversed torus polarity (left panel) and 2.6-GeV, normal torus polarity (right-hand panel). The red curve is the input function derived from a fit to the measured A'_{LT}. The blue points calculated with the same input function and averaged over the bins. The black points are the product of the simulation.

we averaged the input functions (red curves in Figure 30) over the same bins used in the

analysis so

$$\langle A'^{\,in}_{LT} \rangle = \frac{\int_{bin} A'^{\,in}_{LT}(p_m) dp_m}{\Delta p_m} \tag{26}$$

where $A'^{\,in}_{LT}$ is the input fit function. The bin-averaged asymmetries are the blue points in Figure 30. There is good agreement over the range of p_m within the statistical uncertainties of the Monte Carlo calculation between the bin-averaged input asymmetry and the asymmetry extracted from the simulation. The results validate our analysis codes and support the hypothesis that the asymmetry A'_{LT} is independent of acceptance corrections within our uncertainties.

6.4 Systematic Uncertainties

We now consider systematic uncertainties in our extraction of A'_{LT}. The $\sin\phi_{pq}$-averaged asymmetry can be written as

$$A'_{LT}(p_m) = A'_{LT}(p_m; \vec{f}) \tag{27}$$

where $\vec{f}$ is the set of parameters defining our extraction of A'_{LT}. The standard propagation of uncertainties is used so

$$(\Delta A'_{LT})^2 = \sum_i \left(\frac{\partial A'_{LT}}{\partial f_i} \right)^2 (\delta f_i)^2 \tag{28}$$

where the index i is over the parameter set $\vec{f}$. The primary contributions to the systematic uncertainty are shown in Table 10 along with the maximum value. Additional cuts like the electron EC fiducial cut and the Egiyan electron momentum threshold had no effect on the final value of the helicity asymmetry. The results for quantities 1-10 in Table 10 as a

Row	Quantity	$\delta A'_{LT}$
1	W_n cut	< 0.003
2	Δp_e cut	< 0.002
3	EC track coordinate cut	< 0.002
4	EC sampling fraction	< 0.002
5	EC pion threshold	< 0.002
6	Number of Photoelectrons	< 0.005
7	Beam Polarization	< 0.001
8	Beam charge asymmetry	< 0.002
9	m_p cut	< 0.003
10	RC correction	< 0.004
11	electron/proton fiducial cuts	< 0.002

Table 10: Inventory of systematic uncertainties (maximum magnitudes for p_m-dependent quantities).

function of p_m for the normal and reversed torus polarity runs were extracted and are shown

in Figures 81-90 of Appendix I. The measurement of the uncertainties on the fiducial cuts is discussed below.

The systematic uncertainty on the W_n cut was determined starting with the uncertainty on the width σ from the Gaussian fit to the nucleon peak in the W_n distribution (see Figure 6). Recall the position of the W_n cut was set at 3σ below the pion threshold. We took half the difference between A'_{LT} extracted with the maximum and minimum values of the W_n cut (see Figure 81). The value for the Δp_e cut was found by first using the width of the region where the slopes in Figure 10 change value. The uncertainty is taken to be half the difference between A'_{LT} calculated using these extremes (see Figure 82).

The results in Rows 3-6 of Table 10 were determined by (1) changing the position of the cut by $\pm 10\%$ (*e.g*, the EC pion threshold and number of photoelectrons) or by increasing and decreasing the width of a cut by $\pm 10\%$ (*e.g.*, the EC sampling fraction cut). (2) The uncertainty for each data set (normal or reversed torus polarity) and p_m bin was determined by the following expression.

$$\delta A'_{LT} = \frac{A'_{LT}(1.1 \times f_i) - A'_{LT}(0.9 \times f_i)}{2} \tag{29}$$

The results are shown in Figures 83-86.

The results in rows 7-11 of Table 10 were determined individually. For the beam polarization uncertainty (row 7 in Table 10) the measurements of the beam polarization using the Moeller polarimeter during the experiment were used (0.736 ± 0.017). We multiplied A'_{LT} for each data set by the uncertainty on the polarization. See Figure 87 in Appendix I. For the beam charge asymmetry (row 8 in Table 10), the ratio of elastic proton scattering for the two different beam helicities was used. We calculated the systematic uncertainty by multiplying A'_{LT} by the statistical uncertainty on the beam charge asymmetry for each data set. See Table 7 and Figure 88 in Appendix I. The effect of the proton mass cut (row 10 in Table 10) was taken to be half the difference between the helicities asymmetries for the two, 2.6-GeV data with and without the cut applied (see Figure 89 in Appendix I). For the uncertainty on the radiative corrections(row 10 in Table 10) we took half of the difference between the corrected and uncorrected asymmetry (see Figures 21, 22, and 90).

The electron and proton fiducial cuts are not amenable to the procedure described above because of their more complex dependence on angles and particle momenta. We studied their impact on the analysis by probing the changes to the asymmetry when they were turned off. This procedure must be done carefully since changing the fiducial cuts can change the Q^2 distribution that contributes to the sample and could alter the asymmetry. To avoid this effect we added a cut on the normal-torus-polarity data analysis because the Q^2 distribution with the fiducial cuts turned off extended to lower values of Q^2. This cut made the lower limit of Q^2 the same with fiducials cuts on and off. We also turned off the cut on W_n (which selects quasielastic events) to increase the size of the event sample. The uncertainty due to the electron/proton fiducial cuts (row 11 in Table 10) was then taken to be the standard deviation of the average value of the difference between A'_{LT} extracted with the fiducial cuts switched on and off. We call this quantity $\Delta A'^{fid}_{LT}$. The results for the two data sets are shown in Figure 31. These points were averaged for each data set and the standard deviation taken to be the uncertainty. We note here that the statistical uncertainties shown in the figures are accurate; they are determined by constructing $\Delta A'^{fid}_{LT}$ from the event sample that

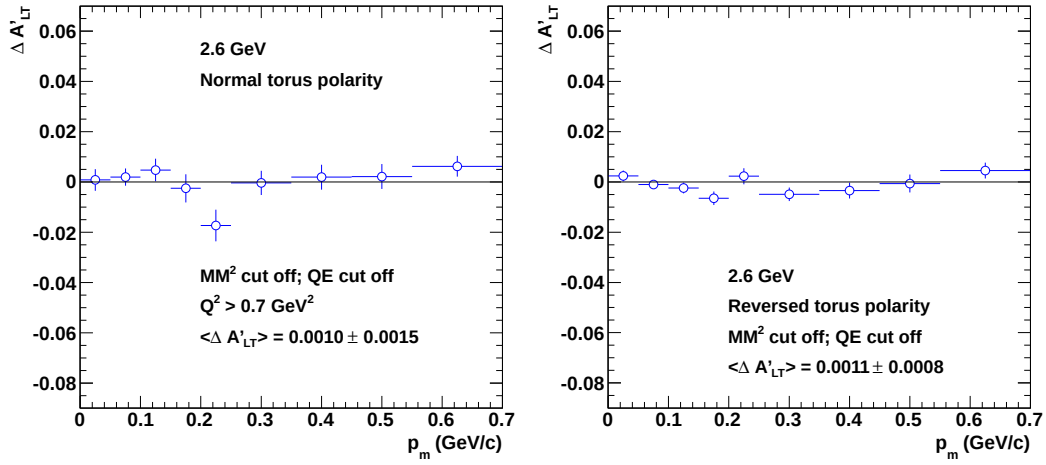

Figure 31: The left-hand panels shows the difference $\Delta A'^{fid}_{LT}$ between the asymmetry extracted with the electron and proton fiducial cuts on and off for the normal torus polarity data. The right-hand panel shows the same quantity for the reversed torus polarity data.

passed all the cuts except the fiducial ones. They are not extracted by adding the statistical uncertainties for the A'_{LT} distributions for fiducial cuts on and off. That method is incorrect because the two samples (fiducial cuts on and off) are not independent ones.

The uncertainties from Table 10 were added in quadrature. The final results are shown in Figure 32. The maximum value of each quantity was determined and entered in Table 10.

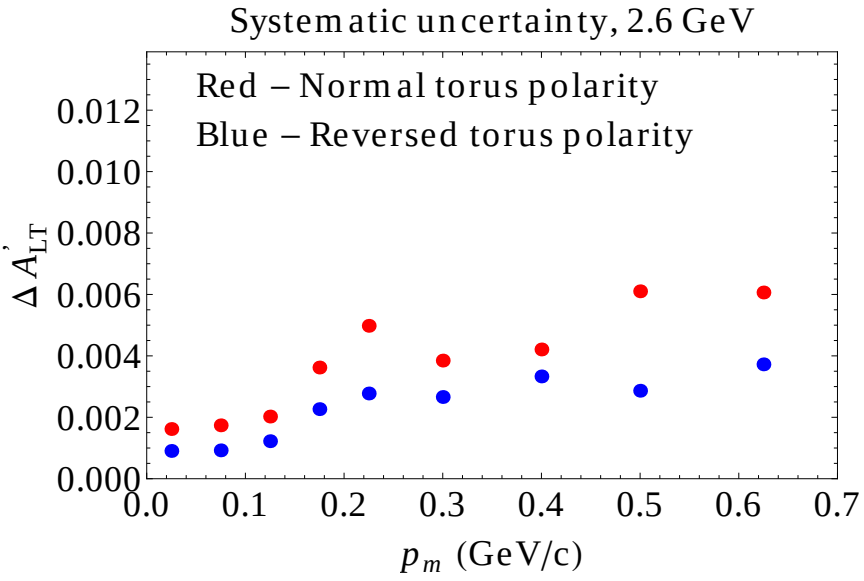

Figure 32: Systematic uncertainty on A'_{LT} as a function of Q^2 for the normal torus polarity data (red) and the reversed polarity data (blue).

The systematic uncertainty is everywhere less than 10^{-2}.

6.5 Results and Comparison with Theory

Preliminary results with statistical and systematic uncertainties are shown in Figures 33 and 34. The error bars on the points are for statistical uncertainties and systematic uncertainties

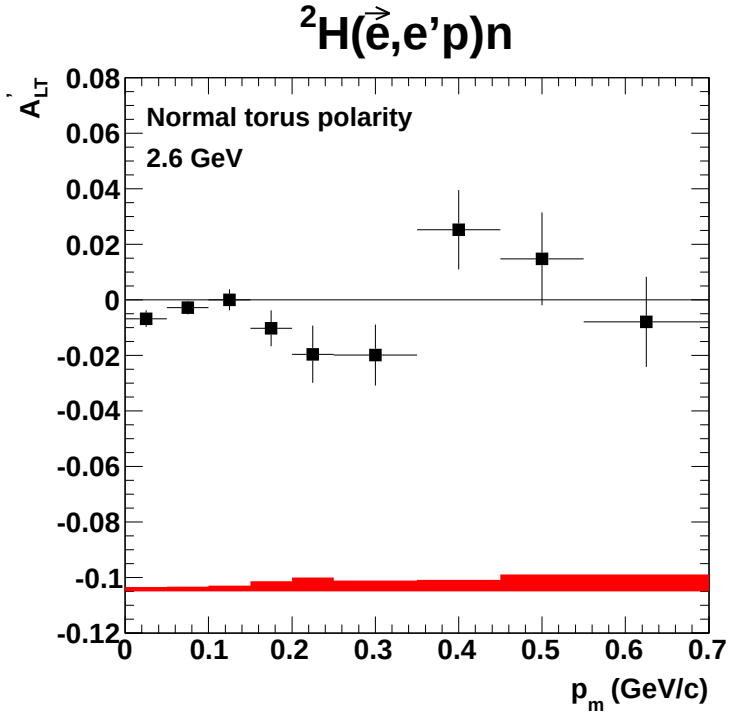

Figure 33: Preliminary results for helicity asymmetry A'_{LT} for the ^{2}H(ẽ, e′p)n reaction at 2.6 GeV with normal torus polarity.

are represented by the bar graphs. For each torus setting, the helicity asymmetry A'_{LT} starts near zero as expected and there is a dip at $p_m = 0.23$ GeV/c. At higher missing momentum A'_{LT} is consistent with zero. Within the statistical uncertainties both asymmetries are about the same.

In Figure 35 we compare our preliminary results with several calculations. The black curves are from Arenhövel [32]. The starting point for this calculation is the non-relativistic Schrödinger equation and other effects are added: relativistic corrections, meson exchange currents, isobar currents, and final state interactions. The black curves here are averaged over the CLAS acceptance. There is reasonable agreement between the reversed-torus-polarity data at lower average Q^2 and the calculation for $p_m < 0.2$ GeV/c, but at higher p_m they diverge. For the normal-torus-polarity data at higher average Q^2 the calculations predict a much deeper asymmetry than observed. The green curves are from Laget [33]. He follows a diagrammatic approach for $Q^2 = 1.1$ GeV^2 (lower panel) and $Q^2 = 0.7$ GeV^2 (upper panel). The curves in each panel are for a single value of Q^2. For the lower Q^2 data (upper panel),

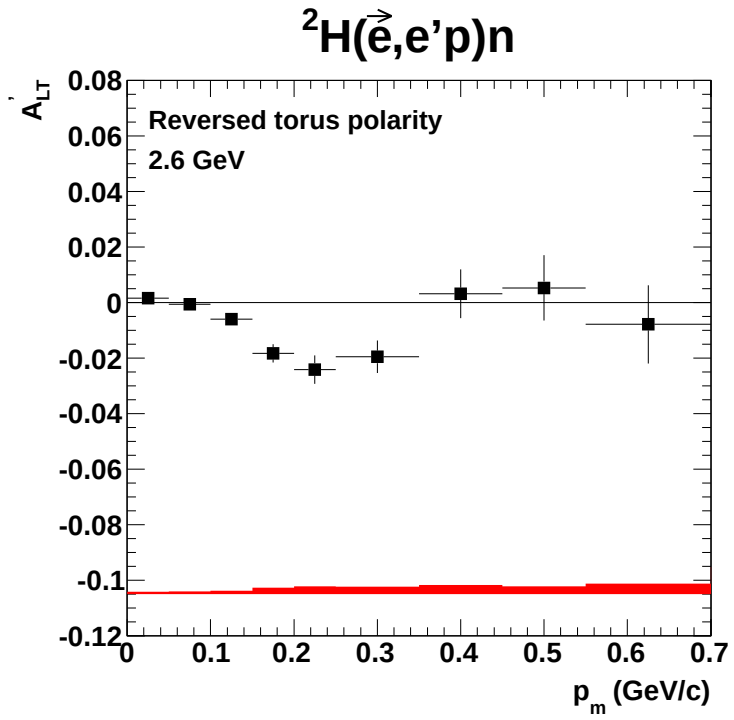

Figure 34: Preliminary results for helicity asymmetry A'_{LT} for the ^{2}H(ẽ, e′p)n reaction at 2.6 GeV with reversed torus polarity.

the calculation produces a more pronounced dip that extends to larger missing momentum than the data. For the higher Q^2 results (lower panel), the dip has shrunk closer to zero and agrees well with the data for $p_m < 0.35$ GeV/c.

The red curves are from Jeschonnek and Van Orden [31, 34]. They use a fully relativistic calculation in the impulse approximation, the Gross equation for the deuteron ground state, and the SAID parameterization of the NN scattering amplitude for FSI. The off-shell form factor cutoff is set to $\Lambda_N = 1.0$ GeV. The red curves are averaged over the CLAS acceptance. There is agreement here on the position and depth of the dip centered at $p_m = 0.23$ GeV/c for the low-Q^2 range (reversed torus polarity data). For $p_m > 0.4$ GeV/c the calculation is more negative than the data which may be a sign of the increased influence of meson exchange currents. For the normal torus data at higher average Q^2, the calculation produces a much deeper dip than observed. No parameters were adjusted in the calculations shown here.

Recall that we also investigated a cut to restrict the range of the residual mass W to be near the nucleon mass. This step is made so this analysis is more in keeping with previous work at Bates [9]. A comparison with the same set of calculations is shown in Figure 36. For the low-Q^2 data (reversed torus polarity) shown in the upper panel in Figure 36 the effect of the additional cut on the shape of the asymmetry is limited so the comparison with the theory curves is much the same as discussed above. For the higher Q^2 data (normal torus polarity data) there is a significant change in the asymmetry at around $p_m = 0.23$ GeV/c

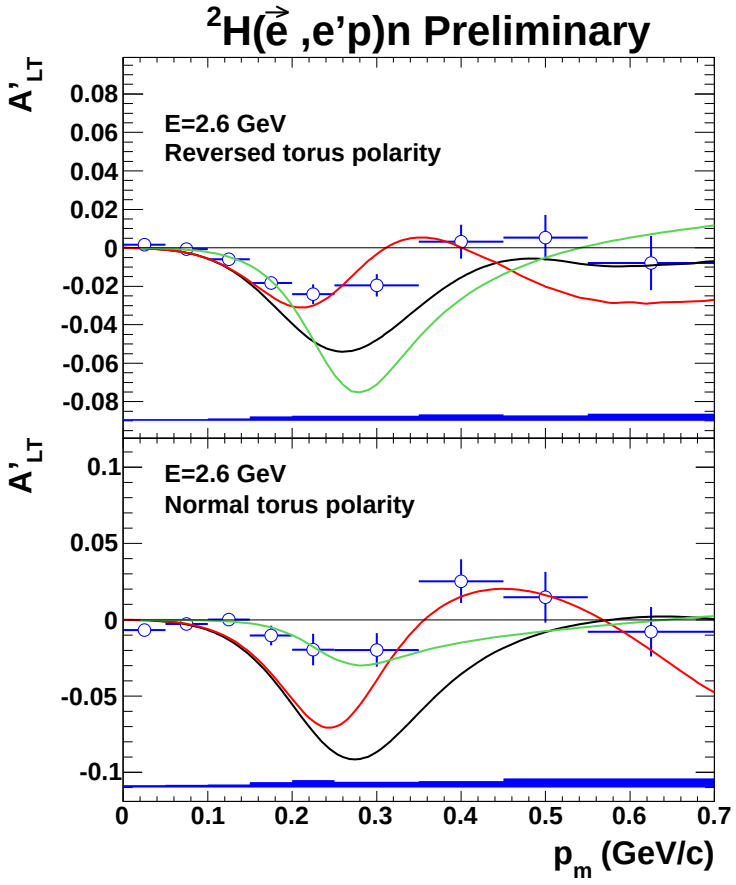

Figure 35: Preliminary results for helicity asymmetry A'_{LT} for the ^{2}H($\tilde{e}$, e′p)n reaction at 2.6 GeV with reversed torus polarity (upper panel) and normal torus polarity (lower panel). The curves are from Arenhövel [32] (black), Laget [33] (green), and Jeschonnek and Van Orden [31, 34]

where the magnitude of the dip increases by a factor of three. There is also now good agreement between the data and the calculation by Jeschonnek and Van Orden across the full range of the missing momentum. The use of this constraint on the data is not well justified, but the result is an intriguing one. Our main results remain the ones shown in Figure 35.

This work is supported by US Department of Energy grant DE-FG02-96ER40980 and Jefferson Science Associates.

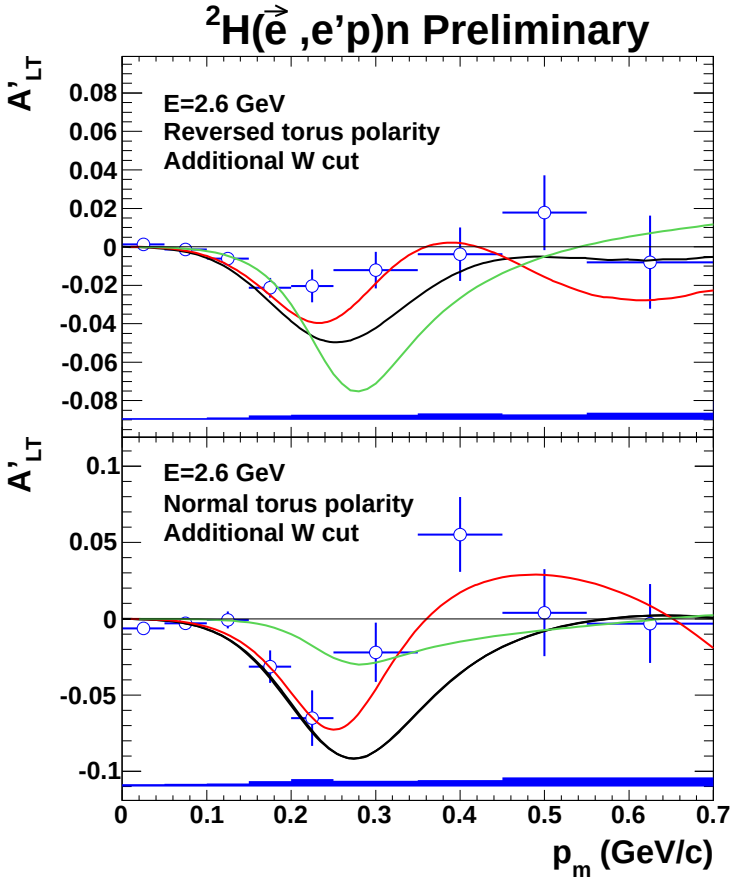

Figure 36: Preliminary results for helicity asymmetry A'_{LT} for the ^{2}H($\tilde{e}$, e′p)n reaction at 2.6 GeV with reversed torus polarity (upper panel) and normal torus polarity (lower panel). These asymmetries differ from the ones in Figure 35 by including the additional cut on the residual mass W described in Section 5.3. The curves are from Arenhövel [32] (black), Laget [33] (green), and Jeschonnek and Van Orden [31, 34]

References

[1] JLab Physics Advisory Committee. PAC14 Few-Body Workshop. Technical report, Jefferson Laboratory, Williamsburg, VA, 1998.

[2] S. Jeschonnek. *Phys. Rev. C*, 63:034609, 2001.

[3] S. Jeschonnek and T.W. Donnelly. *Phys. Rev. C*, 57:2438, 1998.

[4] S. Jeschonnek and J.W. Van Orden. *Phys. Rev. C*, 62:044613, 2000.

[5] F. Ritz, H. Goller, Th. Wilbois, and H. Arenhoevel. *Phys. Rev. C*, 55:2214, 1997.

[6] DOE/NSF Nuclear Science Advisory Committee. Opportunities in nuclear science: A long-range plan for the next decade. Technical report, US Department of Energy and National Science Foundation, Washington, DC, 2002.

[7] M. Sargsian. *Int. J. Mod. Phy.*, E10:405–458, 2001.

[8] P. Rossi et al. Onset of asymptotic scaling in deuteron photodisintegration. *Phys. Rev. Lett.*, 94(1):12301, 2005.

[9] S. M. Dolfini et al. Out-of-plane measurements of the fifth response function of the exclusive electronuclear response. *Phys. Rev. C*, 60(6):064622, Nov 1999.

[10] S. Boffi, C. Giusti, F.D. Pacati, and M. Radici. *Electromagnetic Response of Atomic Nuclei*. Oxford Science Publications, Oxford University Press, Walton St., Oxford, 1st edition, 1996.

[11] Jr. Adam, J., Franz Gross, Sabine Jeschonnek, Paul Ulmer, and J. W. Van Orden. Covariant description of inelastic electron deuteron scattering: Predictions of the relativistic impulse approximation. *Phys. Rev.*, C66:044003, 2002.

[12] S. Gilad, W. Bertozzi, and Z.-L. Zhou. *Nucl. Phys.*, A631:276c, 1998.

[13] S. Dolfini et al. Out-of-plane quasielastic scattering from deuterium using polarized electrons. *Phys. Rev. C*, 51(6):3479–3482, Jun 1995.

[14] J.D. Lachniet. *A High Precision Measurement of the Neutron Magnetic Form Factor Using the CLAS Detector*. PhD thesis, Carnegie Mellon University, 2005.

[15] J.W.C. McNabb. *Photoproduction of* Λ *and* Σ_0 *hyperons off protons in the nucleon resonance region using CLAS at Jefferson Lab*. PhD thesis, Carnegie Mellon University, 2002.

[16] C. Hadjidakis. private communications.

[17] D. Protopopescu, F.W. Hersman, M. Holtrop, and S. Stepanyan. Fiducial Cuts for electrons in the CLAS/E2 data at 4.4 GeV. Technical Report CLAS Note 2000-007, Jefferson Laboratory, Newport News, VA, 2000.

[18] R. Nyazov and L. Weinstein. Fiducial Cut For Positive Hadrons in CLAS/E2 data at 4.4 GeV. Technical Report CLAS Note 2001-013, Jefferson Laboratory, Newport News, VA, 2001.

[19] Z.-L. Zhou et al. Relativistic Effects and Two-Body Currents in $^2H(e,e'p)n$ Using Out-of-Plane Detection. *Phys. Rev. Lett.*, 87(17):172301, Oct 2001.

[20] T. Tamae, H. Kawahara, A. Tanaka, M. Nomura, K. Namai, M. Sugawara, Y. Kawazoe, H. Tsubota, and H. Miyase. Out-of-plane measurement of the $d(e,\ e^{'}p)$ coincidence cross section. *Phys. Rev. Lett.*, 59(26):2919–2922, Dec 1987.

[21] M. van der Schaar, H. Arenhövel, H. P. Blok, H. J. Bulten, E. Hummel, E. Jans, L. Lapikás, G. van der Steenhoven, J. A. Tjon, J. Wesseling, and P. K. A. de Witt Huberts. Longitudinal-transverse interference structure function of ^2H. *Phys. Rev. Lett.*, 68(6):776–779, Feb 1992.

[22] H. Avakian. CLAS Analysis Note 2002-101, 2002.

[23] K. Joo and C. Smith. Measurement of polarized structure function σ'_{LT} for $p(e, e'p)\pi^0$ in the delta(1232) resonance region. CLAS Analysis Note 2001-109, 2001.

[24] M. Anghinolfi, M. Battaglieri, A. Bersani, R. DeVita, M. Ripani, and M. Taiuti. About the Error Estimation in Charge Assymetry Measurements - A MonteCarlo Simulation. Technical Report CLAS Note 2001-020, Jefferson Laboratory, Newport News, VA, 2001.

[25] A. Afanasev, I. Akushevich, V. Burkert, and K. Joo. *Phys. Rev.*, D66:074004, 2002.

[26] L.W. Mo and Y.S Tsai. *Rev. Mod. Phys.*, 41:205, 1969.

[27] J. Schwinger. *Phys. Rev.*, 76:898, 1949.

[28] G.P. Gilfoyle and A. Afanasev. Radiative corrections for deuteron electro-disintegration. CLAS-Note 2005-022, Jefferson Lab, 2005.

[29] G.P. Gilfoyle. Radiative Corrections Using DEEP. `http://www.richmond.edu/~ggilfoyl/research/RC/wvo.html`, last accessed September 17, 2008.

[30] J.D. Lachniet, W.K. Brooks, G.P. Gilfoyle, B. Quinn, and M.F. Vineyard. A high precision measurement of the neutron magnetic form factor using the CLAS detector. CLAS Analysis Note 2008-103, Jefferson Lab, 2008.

[31] Sabine Jeschonnek and J. W. Van Orden. A new calculation for D(e,e'p)n at GeV energies. *Phys. Rev. C*, 78:014007, 2008.

[32] J. Lachniet, A. Afanasev, H. Arenhövel, W. K. Brooks, G. P. Gilfoyle, D. Higinbotham, S. Jeschonnek, B. Quinn, M. F. Vineyard, et al. Precise Measurement of the Neutron Magnetic Form Factor G_M^n in the Few-GeV^2 Region. *Phys. Rev. Lett.*, 102(19):192001, 2009. `http://link.aps.org/abstract/PRL/v102/e192001`.

[33] J-M. Laget. private communication.

[34] Sabine Jeschonnek and J. W. Van Orden. Ejectile polarization for ^{2}H$(e, e'\vec{p})n$ at GeV energies. *Phys. Rev. C*, 81(1):014008, Jan 2010.

[35] K. Aniol and J. Cornejo. Radiative corrections, external and internal bremsstrahlung factors. Technical report, Cal State, LA, 2003. http://www.calstatela.edu/academic/nuclear_physics/schwin12_extbrems.html.

[36] M. N. Rosenbluth. High Energy Elastic Scattering of Electrons on Protons. *Phys. Rev.*, 79(4):615–619, Aug 1950.

[37] F. Gross. *Relativistic Quantum Mechanics and Field Theory*. Wiley, New York, NY, 1993.

[38] E. J. Brash, A. Kozlov, S. Li, and G. M. Huber. New empirical fits to the proton electromagnetic form factors. *Phys. Rev.*, C65:051001, 2002.

A Electron Fiducial Cuts

To focus our analysis on the regions of uniform proton acceptance we have largely followed the technique of D.Protopopescu, *et al.* in [17]. One of the benefits of the procedure described below is to make the fiducial cuts smoothly varying functions of particle momentum and position and reduce the chances of experimental artifacts appearing in the analysis.

1. Two-dimensional histograms of ϕ_e versus θ_e in momentum bins of 100 MeV/c are extracted first. This was done starting with a three-dimensional histogram in ROOT of p_e versus θ_e versus ϕ_e for electron singles events and then projecting out the $\phi_e - \theta_e$ histogram for each electron momentum bin. Figure 37 is a sample of the $\phi_e - \theta_e$ distribution for $p_e = 2.2 - 2.3$ GeV/c and a beam energy of 4.2 GeV.

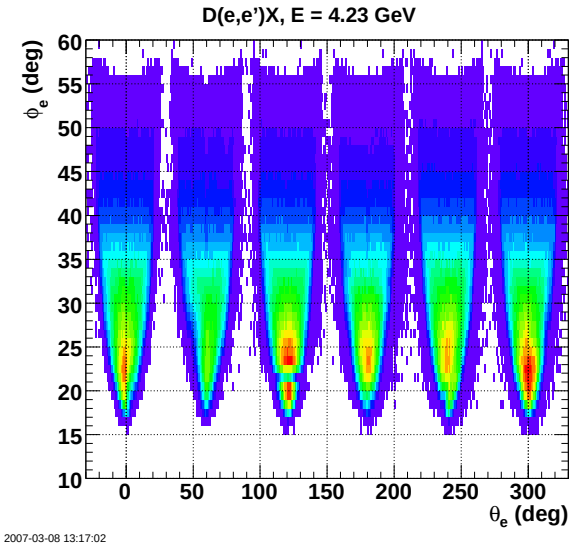

Figure 37: Distribution of ϕ_e versus θ_e for electrons for all sectors and E = 4.2 GeV.

2. A series of one-dimensional histograms of ϕ_e in one-degree bins in θ_e are projected out for each electron momentum bin. These distributions are then fitted with a trapezoidal function. We refer to these fits as first generation fits. Some typical results are shown in Figure 38.

3. The edges of the central, flat region of the ϕ_e distribution for each θ_e bin at this value of the electron momentum are extracted from the fits and plotted versus θ_e. See Figure 39. The distribution is then fitted with a function that can be asymmetric about the central ϕ_e angle of the sector. The function used for the upper branch in Figure 39 is

$$\phi_{edge} = \phi_{mid} + b_{lt}\left(1 - \frac{1}{1 + (\theta_e - t_{l0})/a_{lt}}\right) \tag{30}$$

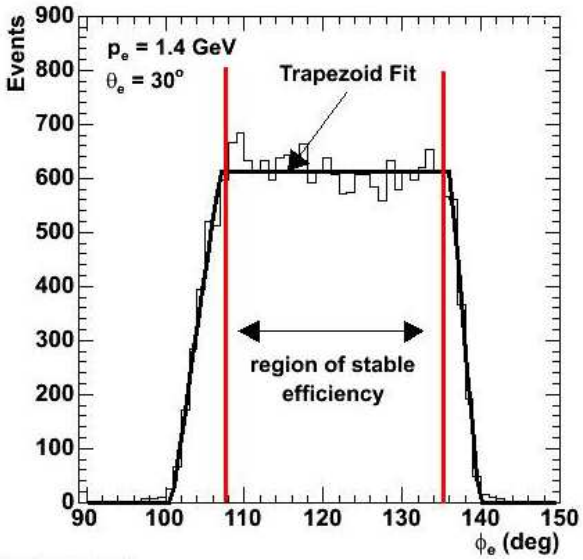

Figure 38: Electron azimuthal dependence for sector 3, 2.6-GeV, normal polarity run. The electron momentum and polar angle θ_e are given on each plot. The black curve is the result a fit to a trapezoidal function described in the text.

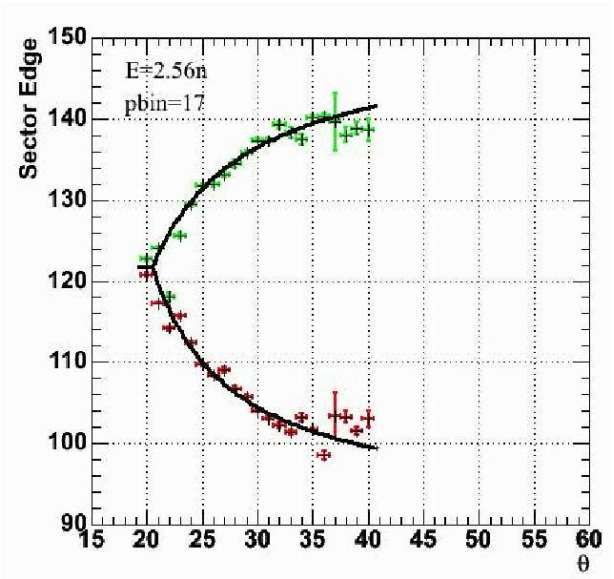

Figure 39: Fits to the position of the edges of the plateau of the trapezoids used in the first generation fits. The horizontal axis is the electron polar angle in degrees.

where b_{lt}, ϕ_{mid}, t_{l0}, and a_{lt} are fit parameters. For the lower branch in Figure 39, we use

$$\phi_{edge} = \phi_{mid} - b_{rt}\left(1 - \frac{1}{1 + (\theta_e - t_{l0})/a_{rt}}\right) \tag{31}$$

where b_{rt}, ϕ_{mid}, t_0, and a_{rt} are fit parameters. The average of ϕ_{mid} is taken from the separate fits to each branch and then the fits are done again with ϕ_{mid} fixed. An example of the results is shown as the black curve in Figure 39 . These curves are called second generation fits.

4. The last step in generating the electron fiducial cuts is to take the results of the second generation fits to the ϕ_e versus θ_e distributions as a function of electron momentum p_e and fit these results for each sector. The parameter t_0 is fitted with a power function and the other fit parameters (a_{lt}, b_{lt}, a_{rt}, b_{rt}) are fitted with a fifth-order polynomial. These curves are third generation fits. Plots of these fits for all sectors are shown in Appendix B. An example of the final CLAS electron acceptance is shown in Figure 40 for the 4.2-GeV data set.

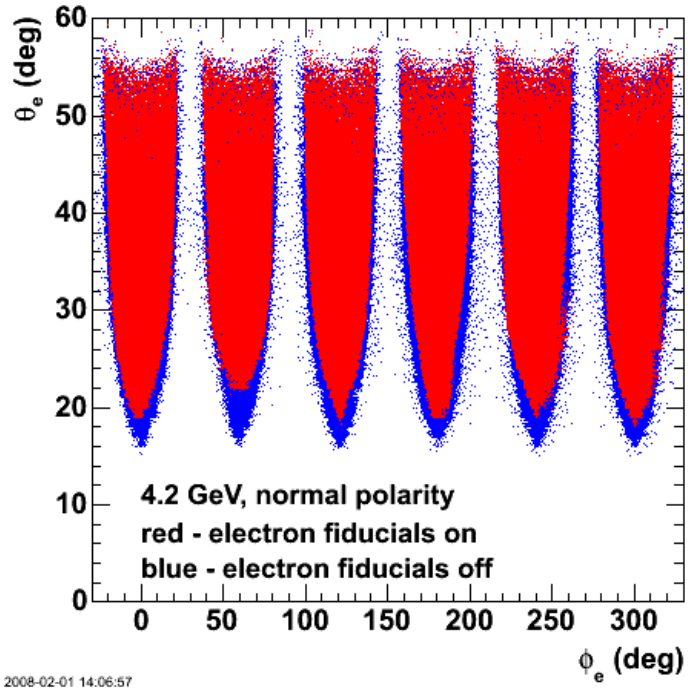

Figure 40: CLAS acceptance for electrons at E = 4.2 GeV with fiducial cuts turned on (red points) and off (blue points).

B Electron Fiducial Fits

Third Generation Fits, 2.6 GeV, normal polarity.

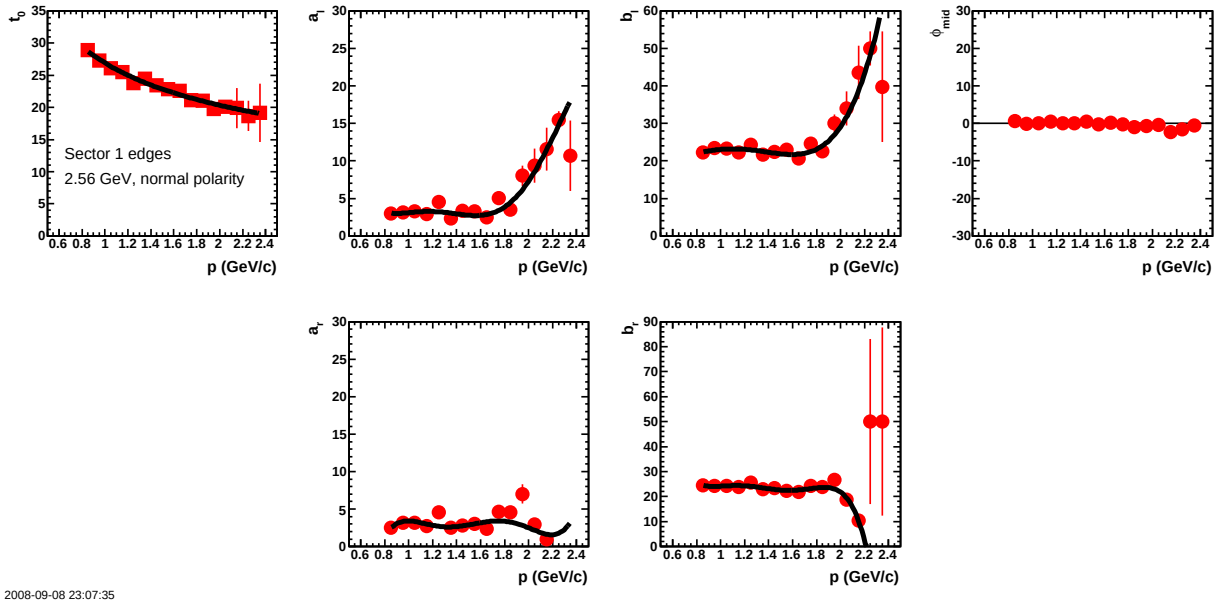

Figure 41: Sector 1.

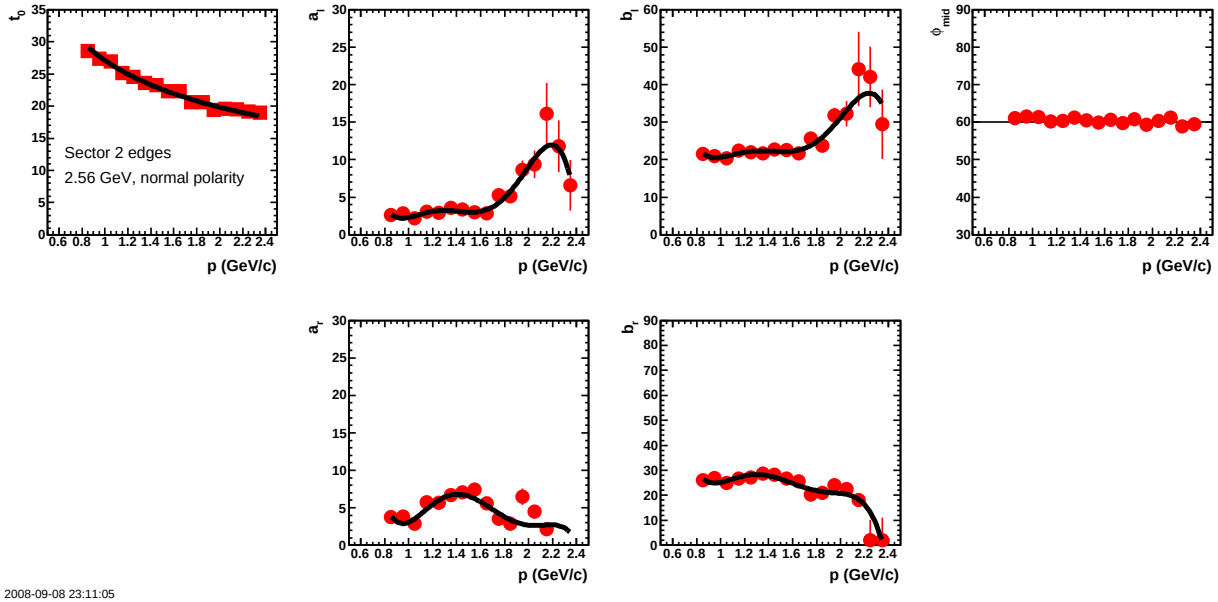

Figure 42: Sector 2.

Third Generation Fits, 2.6 GeV, normal polarity.

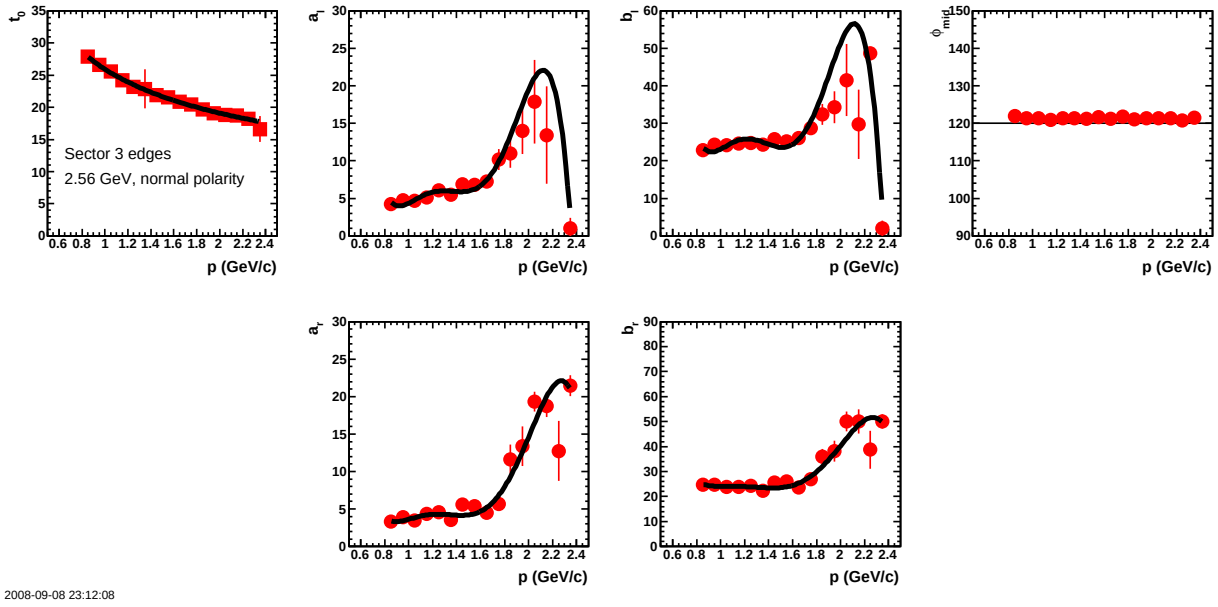

Figure 43: Sector 3.

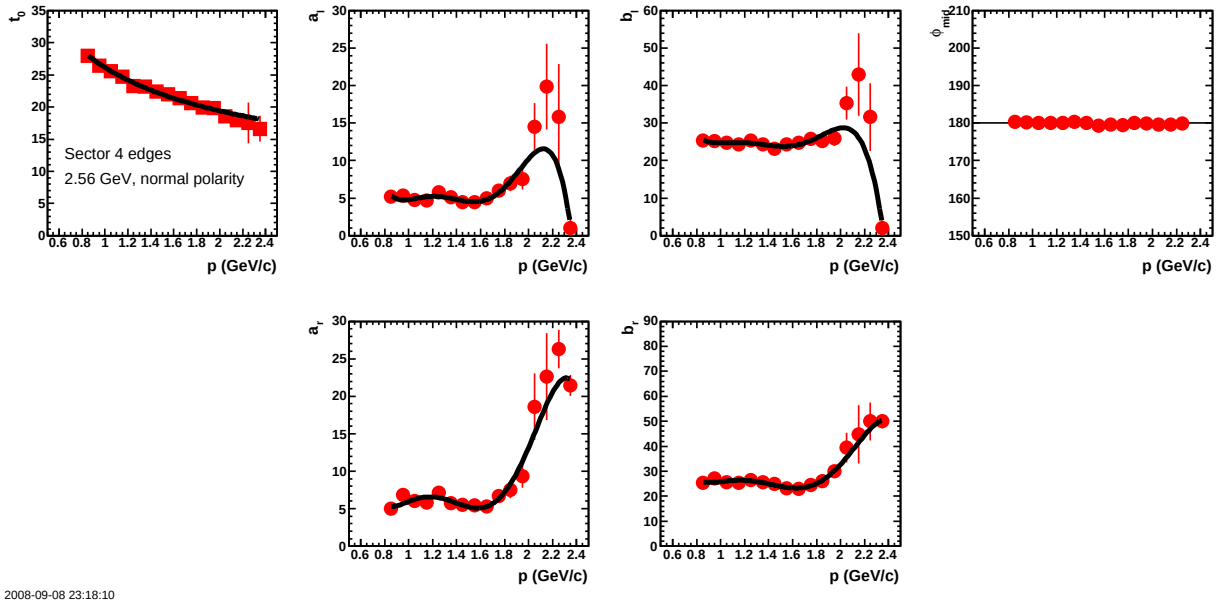

Figure 44: Sector 4.

Third Generation Fits, 2.6 GeV, normal polarity.

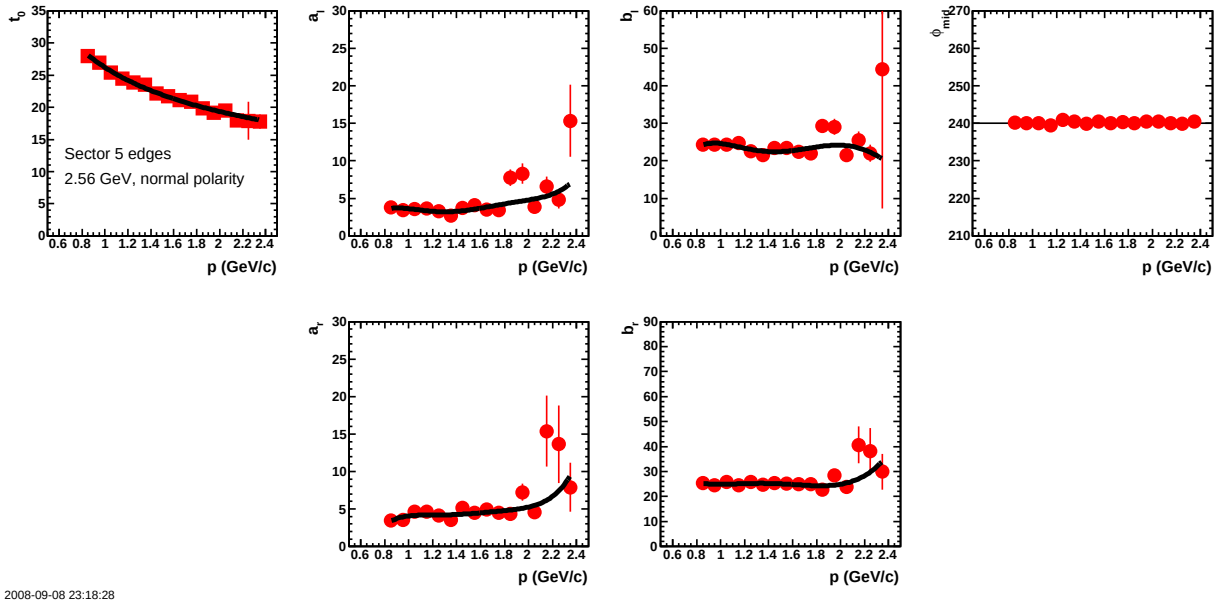

Figure 45: Sector 5.

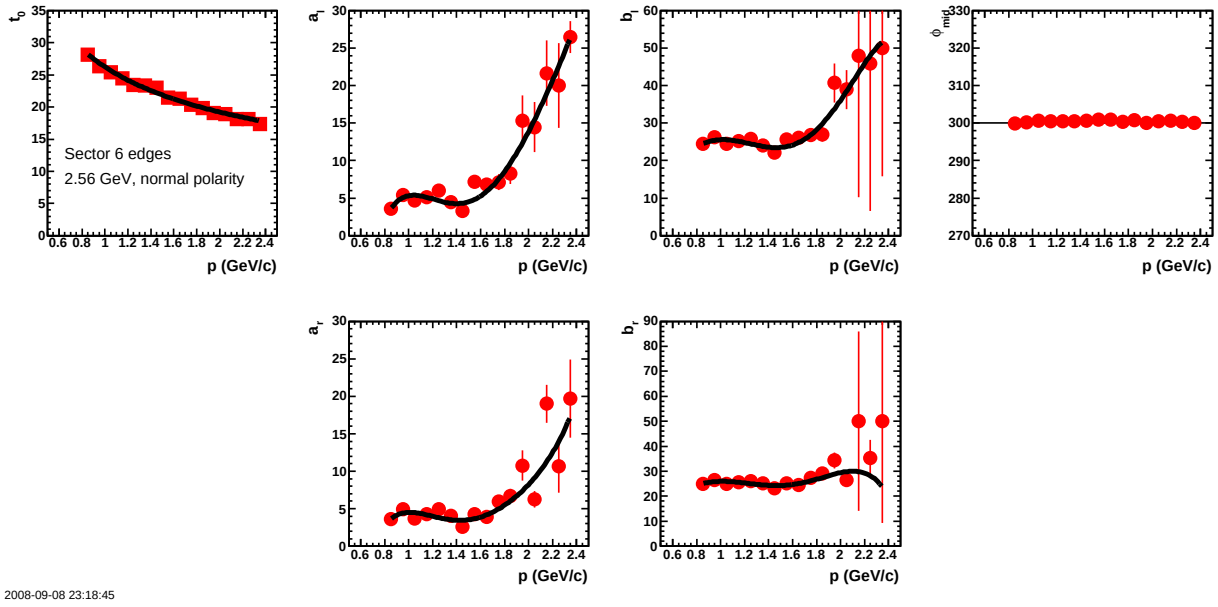

Figure 46: Sector 6.

Third Generation Fits, 2.6 GeV, reversed polarity.

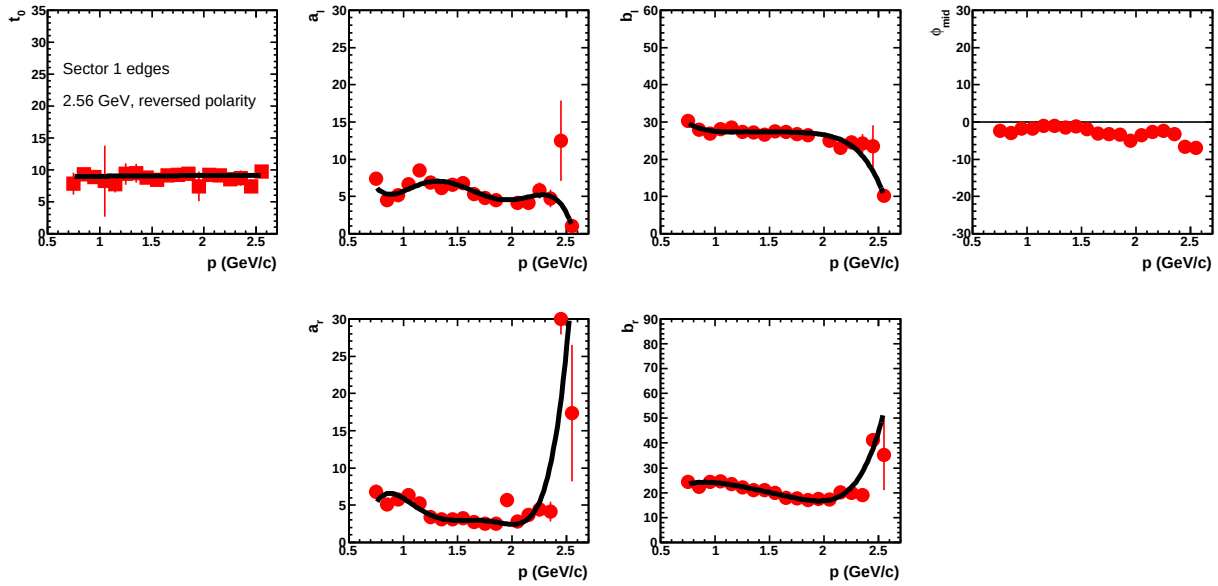

Figure 47: Sector 1.

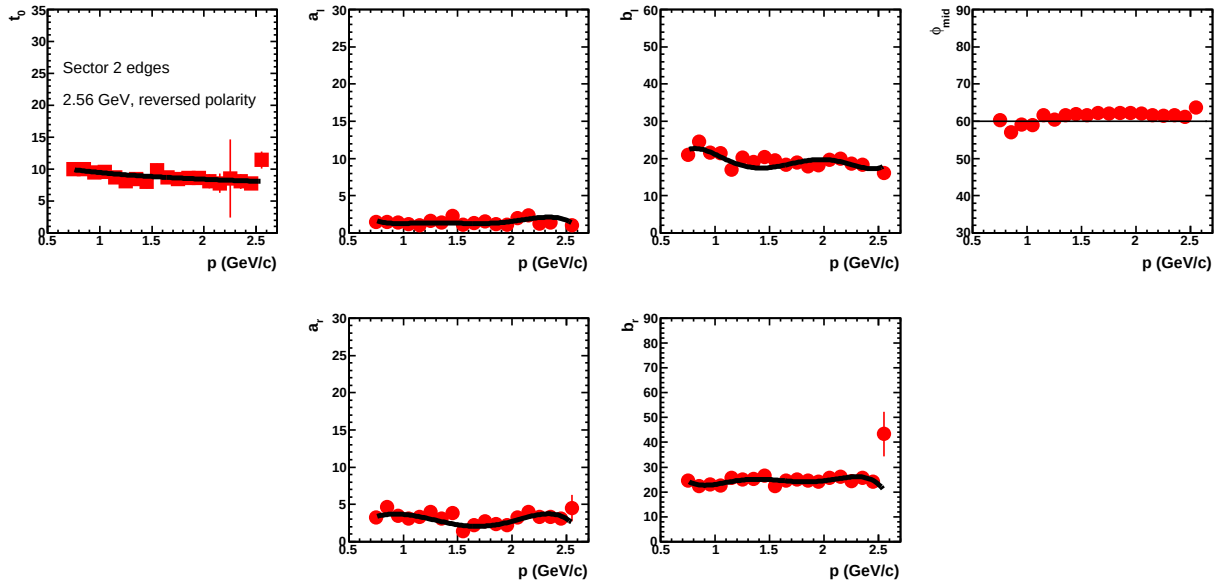

Figure 48: Sector 2.

Third Generation Fits, 2.6 GeV, reversed polarity.

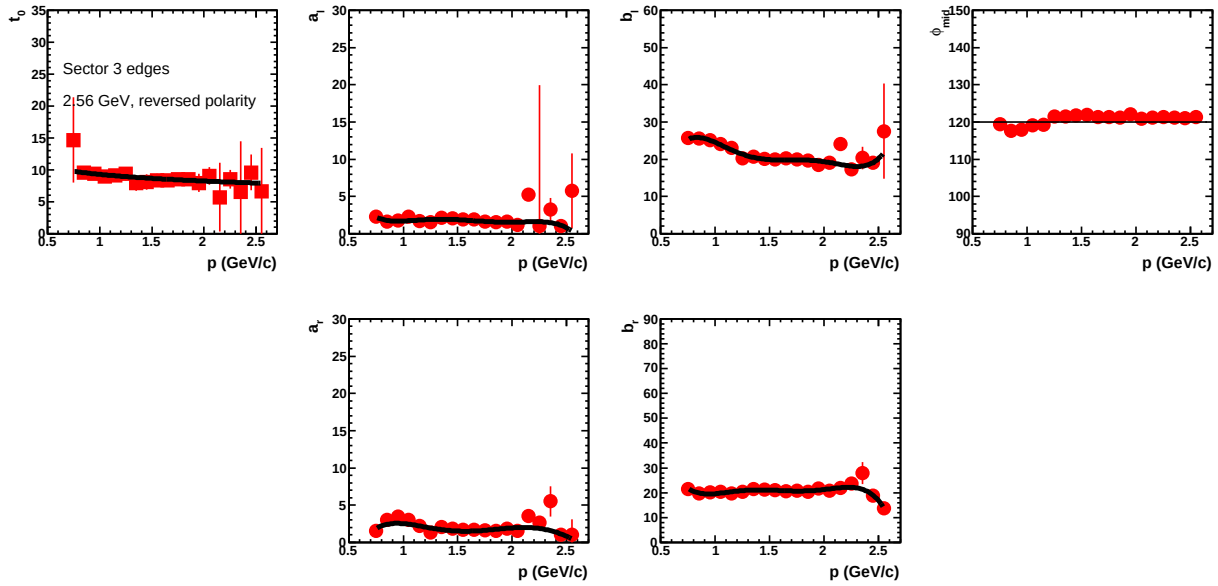

Figure 49: Sector 3.

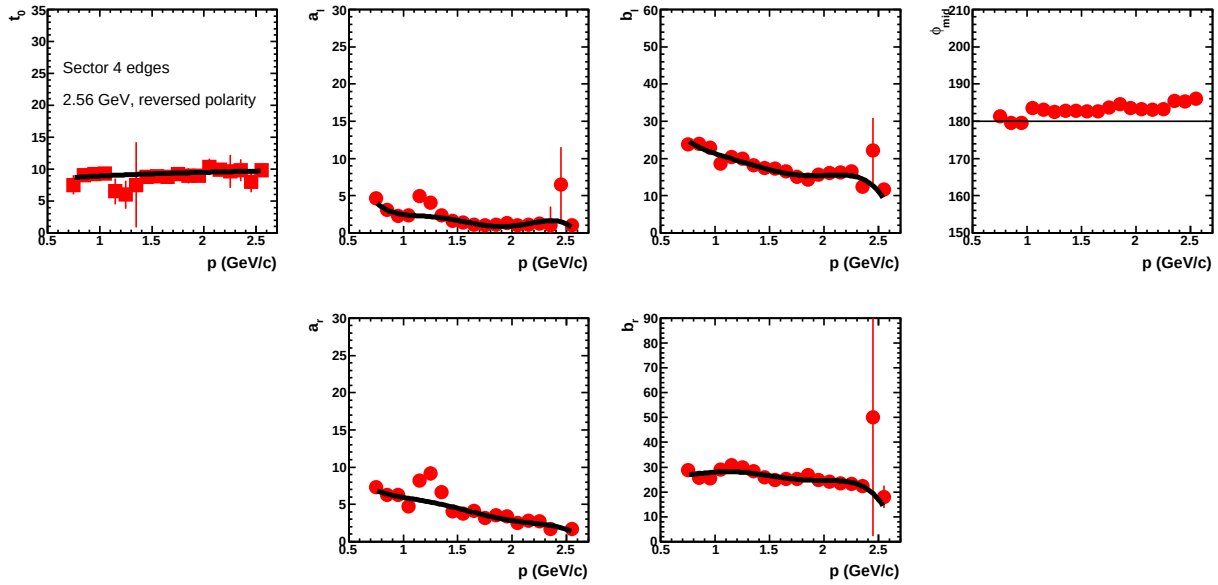

Figure 50: Sector 4.

Third Generation Fits, 2.6 GeV, reversed polarity.

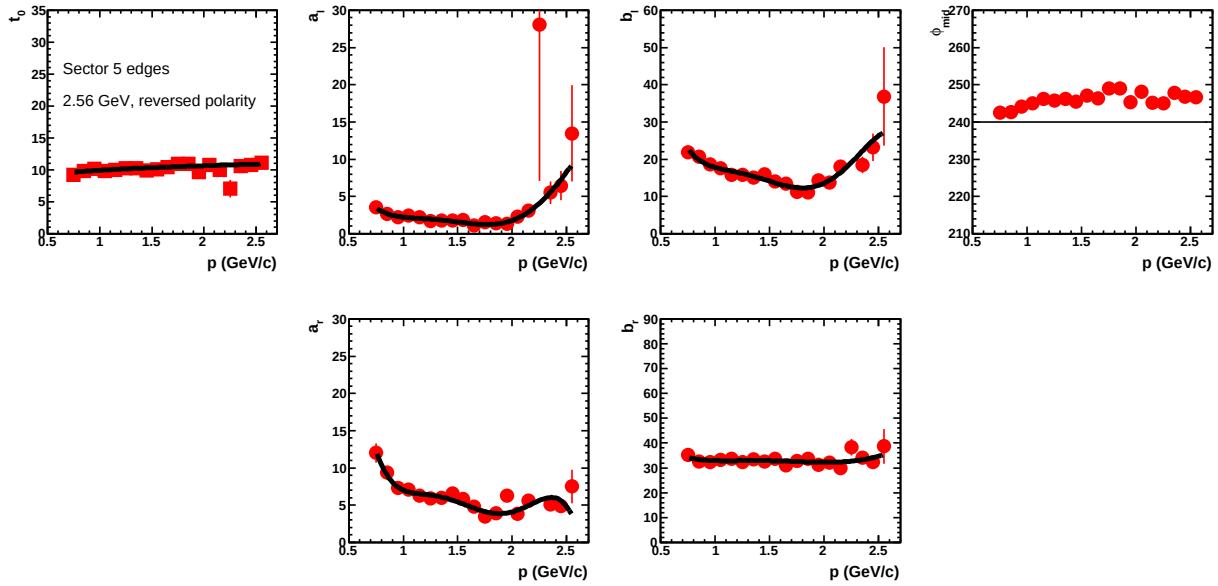

Figure 51: Sector 5.

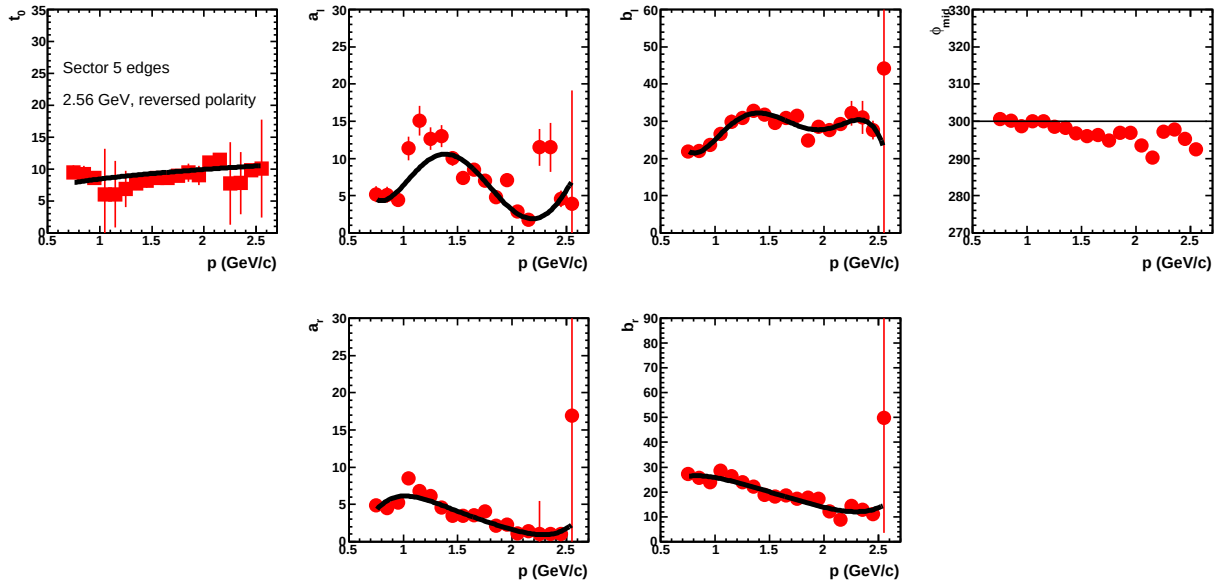

Figure 52: Sector 6.

C Proton Fiducial Cuts

The procedure we used to produce the proton fiducial cuts is described here. First, one has to locate the region of flat acceptance in the center of each region to perform the first-generation, trapezoidal fits to the azimuthal distribution. This proved more of a challenge here than for the electron fiducials. Figure 53 shows the CLAS acceptance for protons that are in coincidence with electrons. Much of the acceptance is flat except for a rounded 'peninsula'

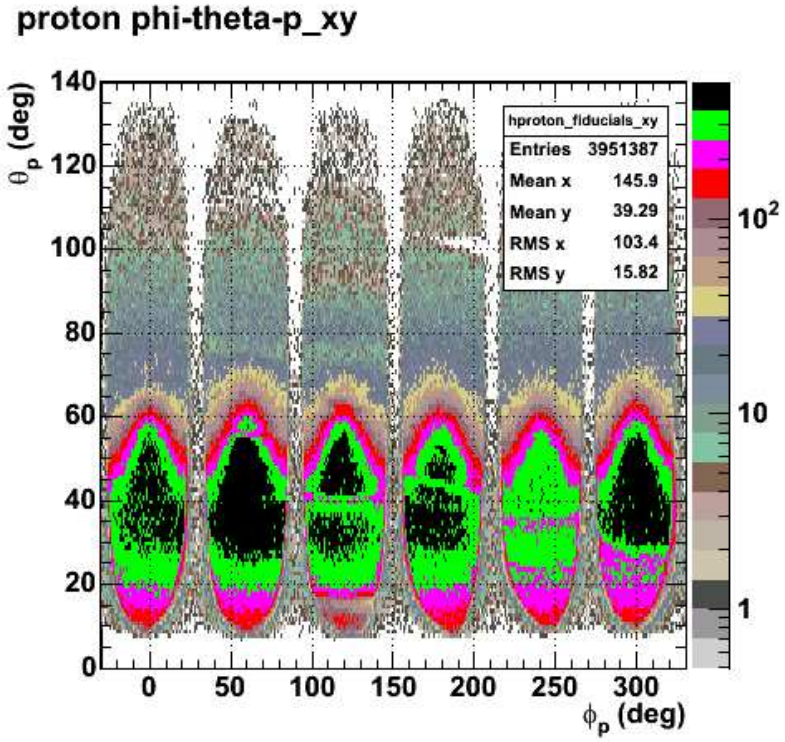

Figure 53: CLAS acceptance for protons in coincidence with electrons.

in the range $\theta_p = 50^\circ - 70^\circ$. This feature distorts the flat acceptance of CLAS and makes our trapezoidal fit (see Appendix A) unusable. This feature is a product of quasielastic events where the proton is strongly correlated with the electron and the forward angle electron acceptance of CLAS; forward-angle, quasielastic electron events have a large-angle proton. Thus, the proton 'peninsula' reflects the shape of the forward-angle electron acceptance in CLAS. The protons in the peninsula come from $e - p$ coincidences where the electron is detected in the forward portion of the opposite sector (*i.e.* an electron in sector 4 will have a correlated proton in sector 1). The shape of the azimuthal distribution is produced by the CLAS, forward-angle, electron acceptance in the opposite sector. To demonstrate this effect more clearly we eliminated all electron events with $\theta_e < 40^\circ$, but only in sector 4. If our explanation is correct, then the protons correlated with those electrons (*i.e.*, the protons that will be detected in quasielastic kinematics in the opposite sector (sector 1)) will be eliminated along with the peninsula. Figure 54 shows this effect. The region $\theta_p = 50^\circ - 70^\circ$ in sector 1 ($\phi_p = -30^\circ - 30^\circ$) is now flat while the peninsula can still be seen in the other

sectors. In our final sample used for generating the proton fiducial cuts we included positive

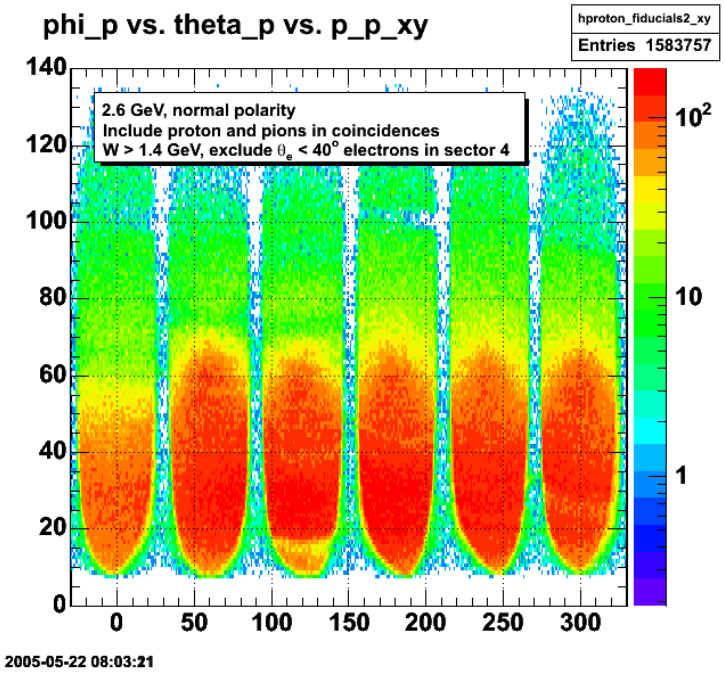

Figure 54: Eliminating the peninsula.

pions from $e-\pi^+$ events since their acceptance should be the same as the proton acceptance [18] and including them in our sample significantly improved the statistical quality. We also required that the mass of the recoiling system have $W > 1.4$ GeV to reduce the the number of correlated quasielastic events. An example of the final event sample is shown in Figure 55. The effect of cuts on the trapezoidal fitting procedure is shown in Figure 56. The black points show the position of the edges found in the first generation fits without the cuts described above to produce a more uniform azimuthal distribution. Note the dramatic shift in the edge positions extracted from these first generation fits in the region $\theta_p = 50° - 70°$. The red points show the positions of the edges found with the trapezoidal fitting method after the constraints described above were included. For hadrons produced at $\theta_h < 45°$, the agreement between the two methods is excellent. For $\theta_h > 45°$, the 'peninsula' has disappeared. The positions of the edges more closely follow the CLAS acceptance.

Once the edges have been found with the trapezoidal fit method, the θ_p dependence of each side of the CLAS acceptance in each sector is fitted in a manner similar to the fits described in Appendix A (second generation electron fits). The functions used are shown in Equations 30-31 in Appendix A. Last, the proton momentum dependence of the second generation fits is itself fitted. The results for all sectors and running conditions are shown in Appendix D. An example of the final hadron acceptance for the 2.6-GeV, reversed torus polarity data set is shown in Figure 57.

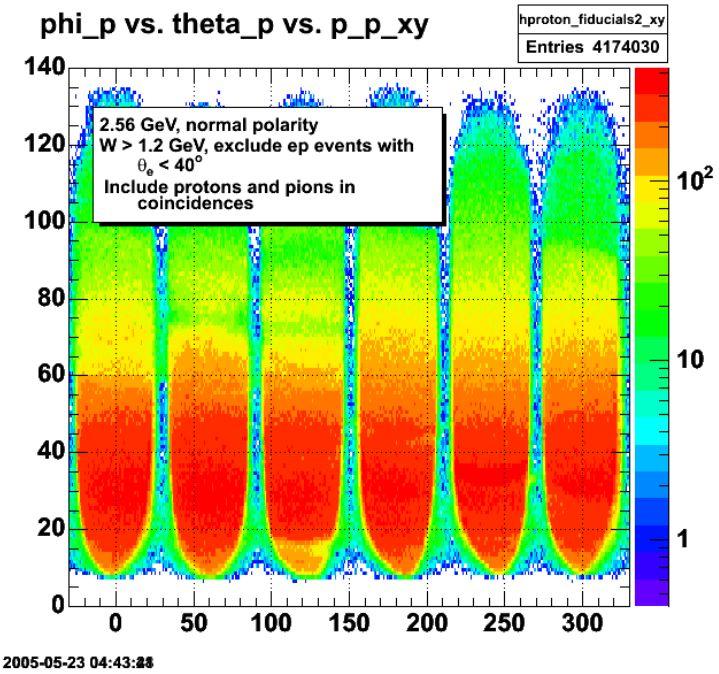

Figure 55: Final hadron sample.

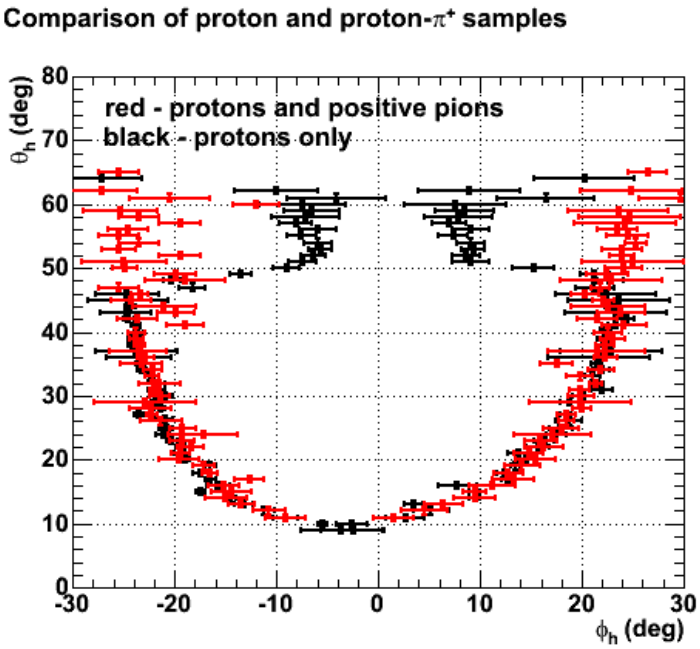

Figure 56: Comparison of hadron edge positions before and after eliminating correlated events.

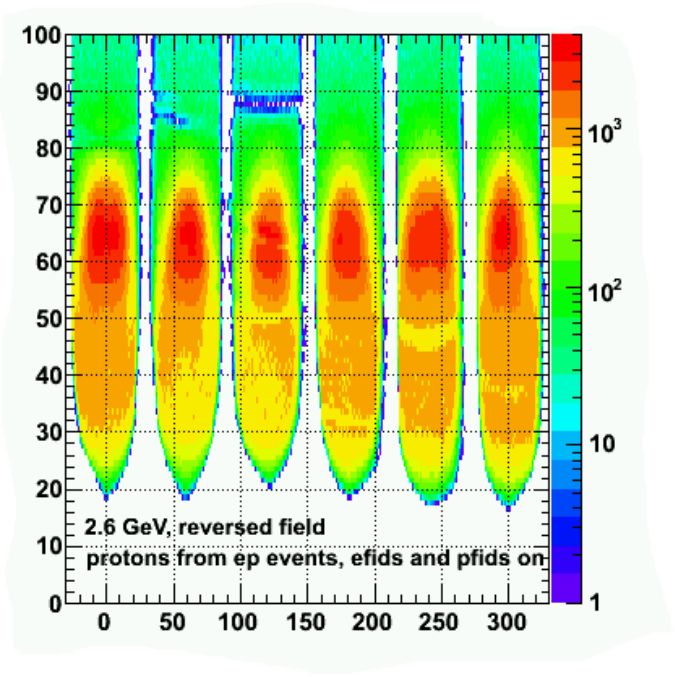

Figure 57: Final hadron acceptance for $e - p$ coincidences for the 2.6-GeV, reversed torus polarity data set.

D Proton Fiducial Fits

Third Generation Fits, 2.6 GeV, normal polarity.

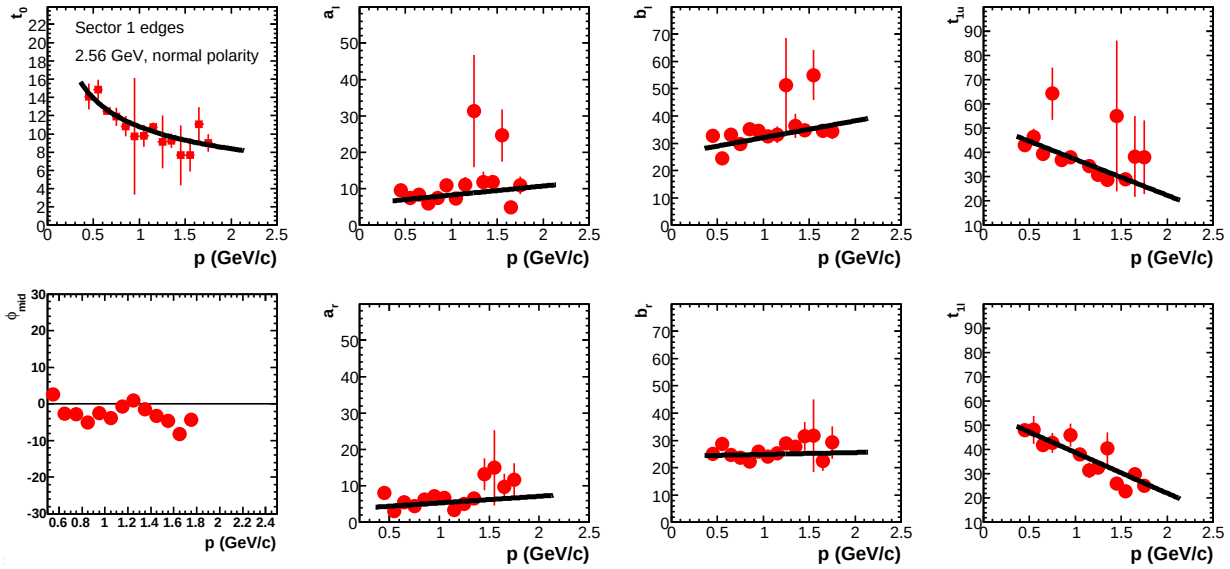

Figure 58: Sector 1.

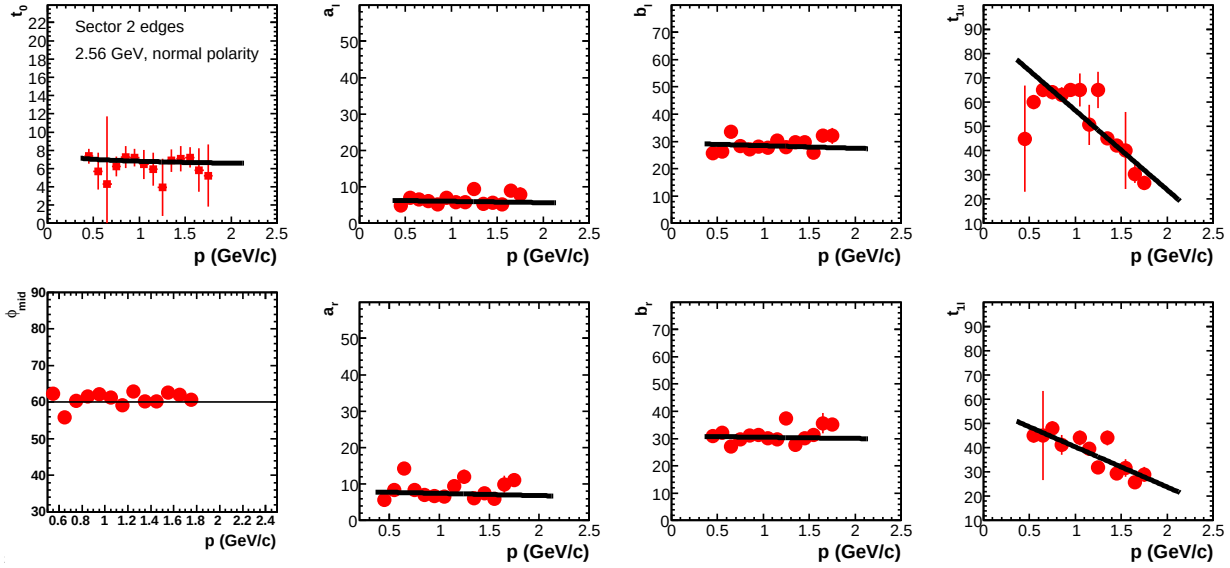

Figure 59: Sector 2.

Third Generation Fits, 2.6 GeV, normal polarity.

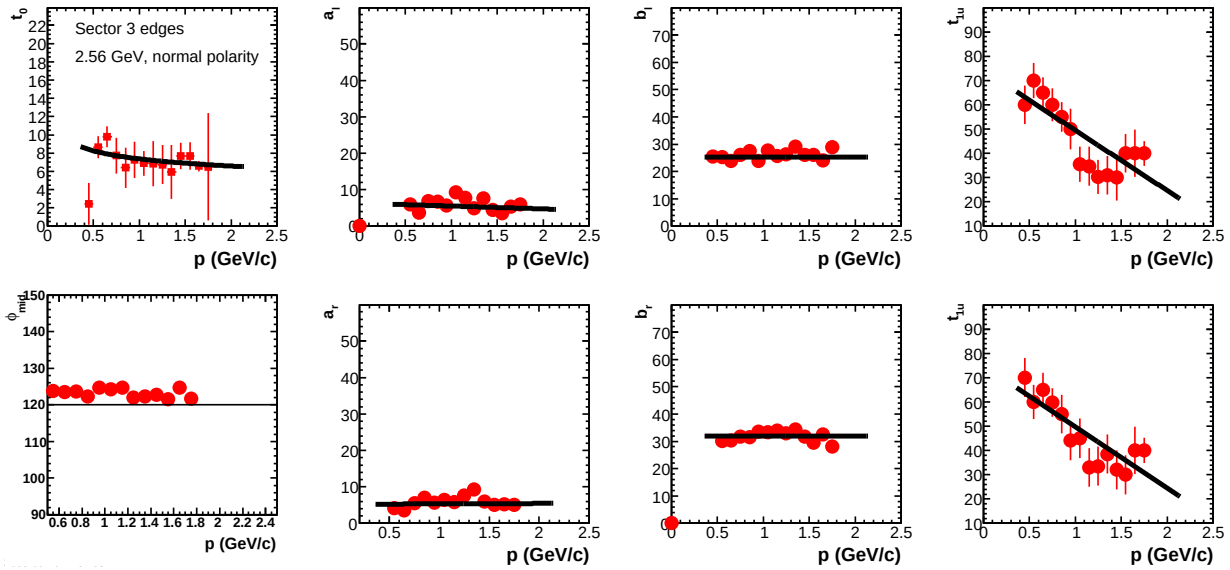

Figure 60: Sector 3.

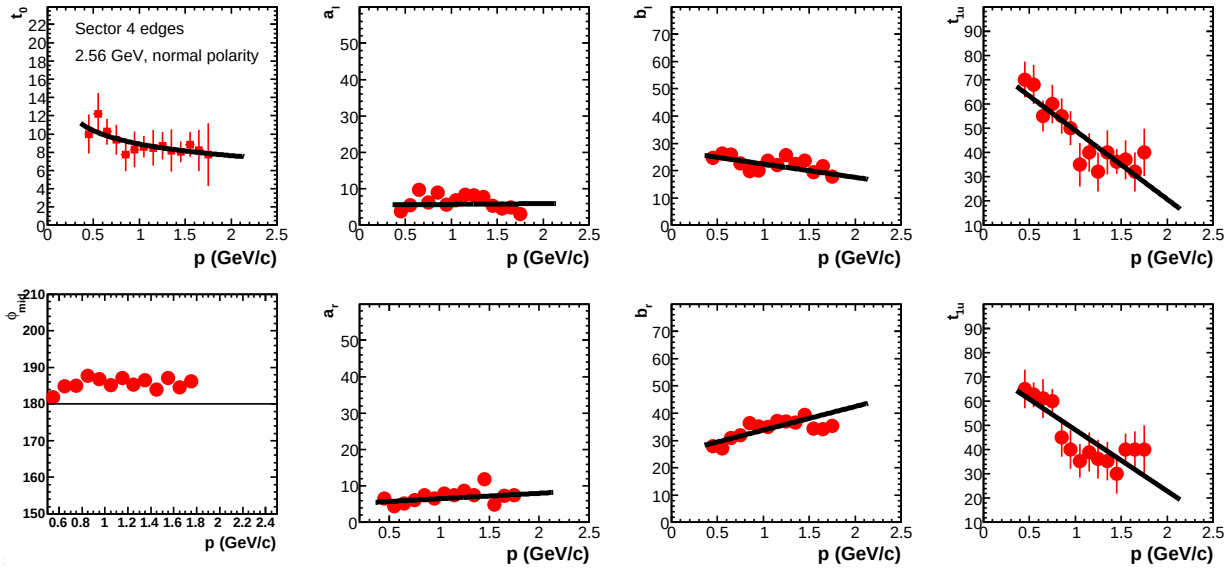

Figure 61: Sector 4.

Third Generation Fits, 2.6 GeV, normal polarity.

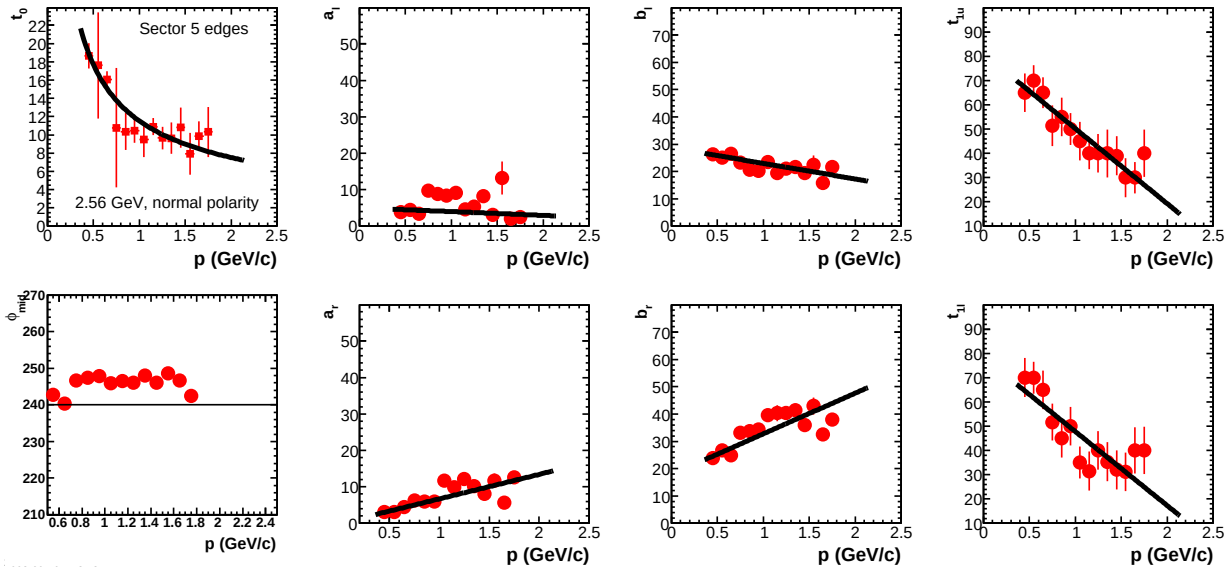

Figure 62: Sector 5.

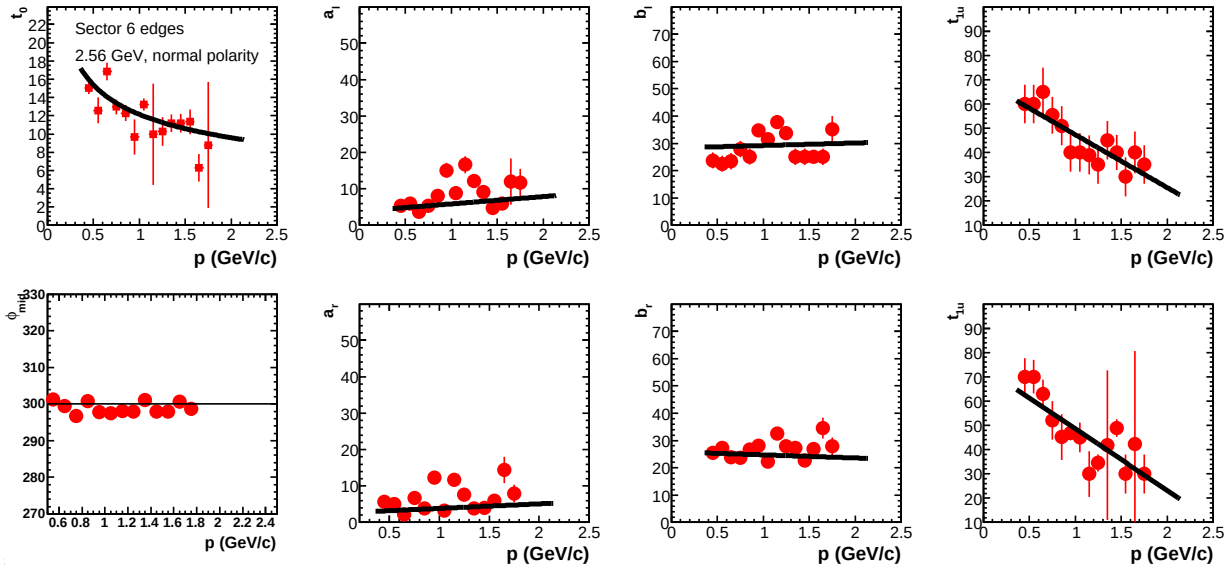

Figure 63: Sector 6.

Third Generation Fits, 2.6 GeV, reversed polarity.

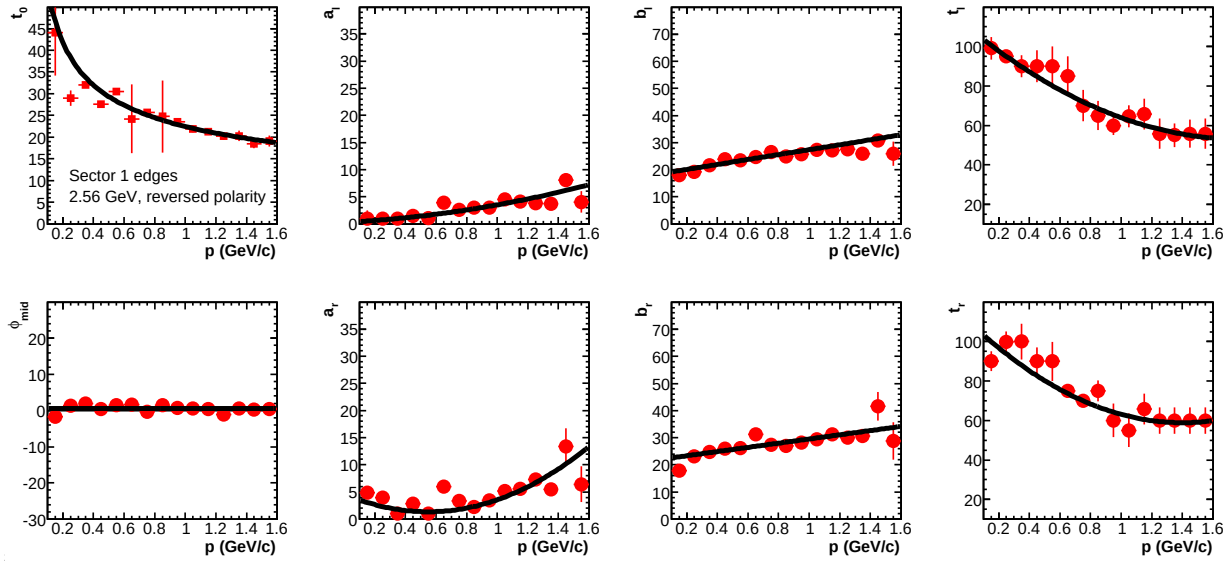

Figure 64: Sector 1.

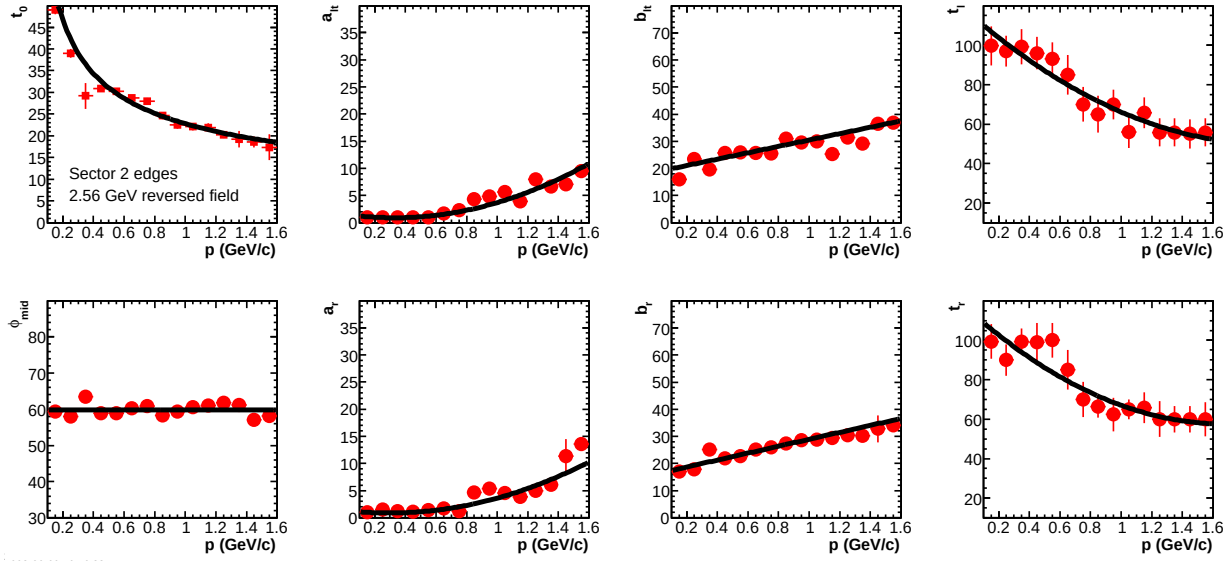

Figure 65: Sector 2.

Third Generation Fits, 2.6 GeV, reversed polarity.

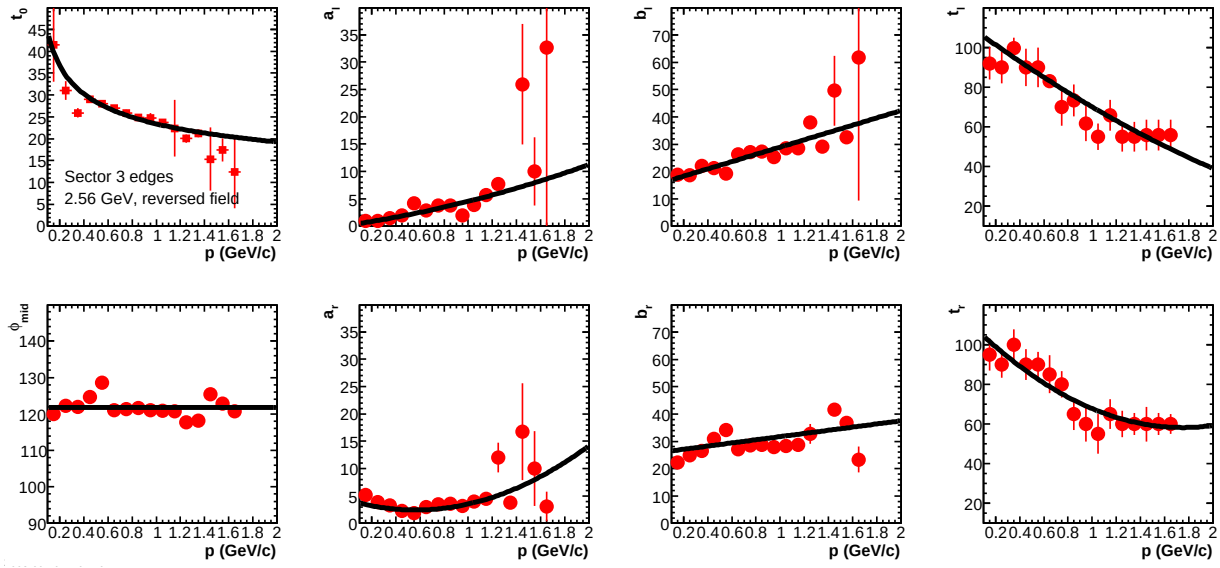

Figure 66: Sector 3.

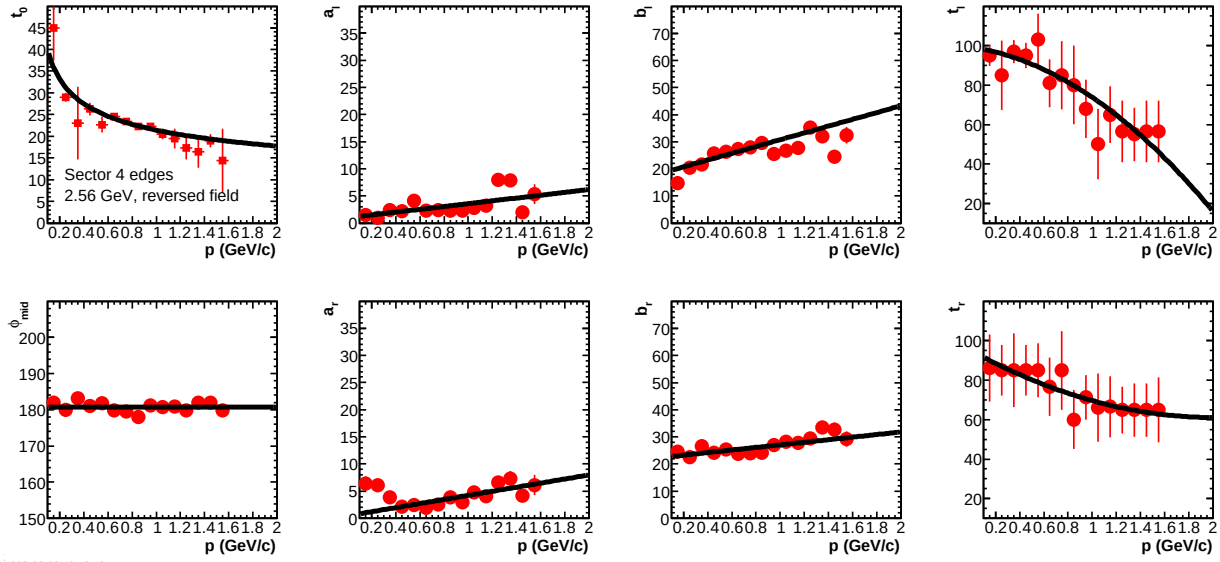

Figure 67: Sector 4.

Third Generation Fits, 2.6 GeV, reversed polarity.

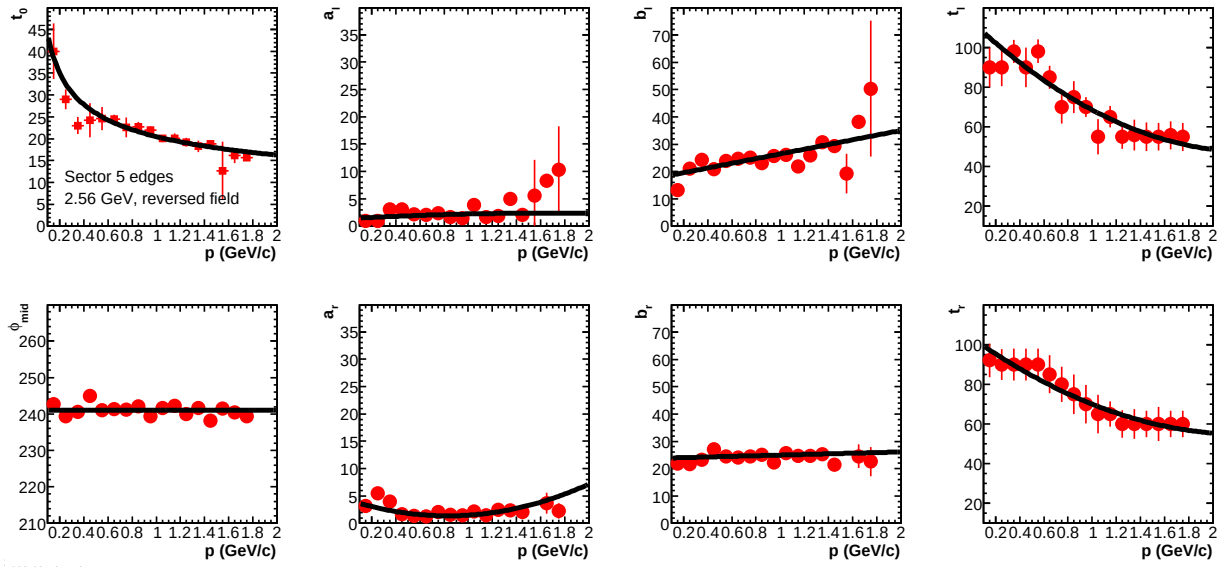

Figure 68: Sector 5.

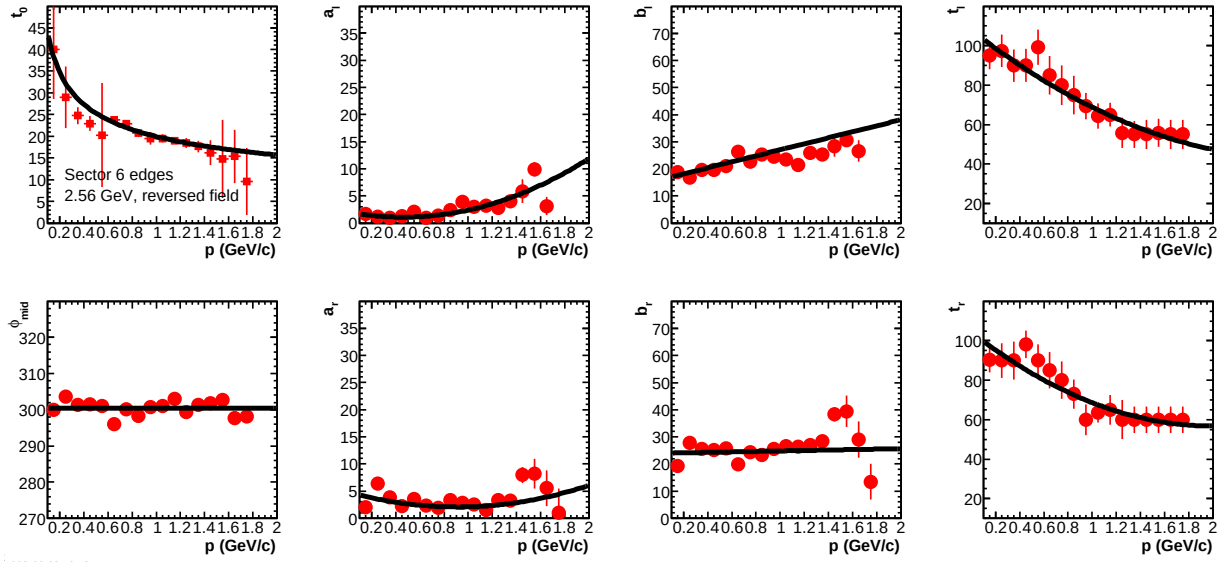

Figure 69: Sector 6.

E Acceptance Effects in $\langle \sin\phi_{pq} \rangle^{\pm}$

To more clearly understand Equations 16-17 which relate $\langle \sin\phi_{pq} \rangle^{\pm}$ to A'_{LT} and the acceptance recall again the expression for the differential cross section for $^2\mathrm{H}(\vec{e}, e'p)n$ (Equations 1 and 3).

$$\frac{d^3\sigma}{d\nu d\Omega_e d\Omega_p} = \sigma^{\pm} = c[\rho_L f_L + \rho_T f_T + \rho_{LT} f_{LT}\cos(\phi_{pq}) + \rho_{TT} f_{TT}\cos(2\phi_{pq}) + h\rho'_{LT} f'_{LT}\sin(\phi_{pq})] \quad (32)$$

$$= \sigma_L + \sigma_T + \sigma_{LT}\cos\phi_{pq} + \sigma_{TT}\cos 2\phi_{pq} + h\sigma'_{LT}\sin\phi_{pq} \quad (33)$$

The $\sin\phi_{pq}$ moment of the data at a given Q^2 and θ^{cm}_{pq} or p_m is defined by the following expression.

$$\langle \sin\phi_{pq} \rangle^{\pm} = \frac{\int_0^{2\pi} \sigma^{\pm}\sin\phi_{pq} d\phi}{\int_0^{2\pi} \sigma^{\pm} d\phi} \quad (34)$$

Now let

$$\sigma^{\pm} = \kappa\epsilon(\phi_{pq}) N^{\pm}(\phi_{pq}) \quad (35)$$

where $N^{\pm}$ is the number of counts for each helicity, ϵ is the CLAS acceptance and may vary with ϕ_{pq}, and κ contains all the other helicity-independent, kinematic factors needed to determine cross sections. In turn, $N^{\pm}$ is composed of different longitudinal and transverse components so

$$N^{\pm}(\phi_{pq}) = N^{\pm}_L + N^{\pm}_T + N^{\pm}_{LT}\cos\phi_{pq} + N^{\pm}_{TT}\cos 2\phi_{pq} + hN^{\pm}_{LT}{}'\sin\phi_{pq} \quad (36)$$

where ϕ_{pq} is the angle between the scattering plane and reaction plane (See Figure 1) and $h = \pm 1$ is the helicity. Hereafter, we will suppress the $\pm$ superscript for clarity and it will be assumed that all $N's$ depend on the helicity. Finally, the CLAS acceptance as a function of ϕ_{pq} at a given Q^2 and θ^{cm}_{pq} or p_m can be expressed as

$$\epsilon(\phi_{pq}) = A_0 + \sum_{m=1}^{\infty}(a_m \sin m\phi_{pq} + b_m \cos m\phi_{pq}) \quad (37)$$

where we have taken advantage of the completeness of the sines and cosines. Substituting Equations 35, 36, and 37 into Equation 34 one obtains (after doing some algebra and some integrals) the following expression

$$\langle \sin\phi_{pq} \rangle^{\pm} = \frac{(N_L + N_T - \frac{N_{TT}}{2})a_1 + \frac{N_{LT}}{2}a_2 + \frac{N_{TT}}{2}a_3 \pm N'_{LT}(A_0 - \frac{b_2}{2})}{2(N_L + N_T)A_0 + N_{LT}b_1 + N_{TT}b_2 \pm N'_{LT}a_1} \quad (38)$$

where we have used $h = \pm 1$. Notice that all the terms in the acceptance function $\epsilon(\phi_{pq})$ with $m > 3$ have disappeared. We now take advantage of the observation that in other measurements the cross section is dominated by the longitudinal (L) and transverse (T) pieces. In the denominator of Equation 38, N_{TT}, N_{LT}, and N'_{LT} are much less than $N_L + N_T$ so we can neglect their contribution. The result is the following expression.

$$\langle \sin\phi_{pq} \rangle^{\pm} = \frac{(N_L + N_T - \frac{N_{TT}}{2})a_1 + \frac{N_{LT}}{2}a_2 + \frac{N_{TT}}{2}a_3 \pm N'_{LT}(A_0 - \frac{b_2}{2})}{2(N_L + N_T)A_0} \quad (39)$$

We now take the difference between $\langle \sin \phi_{pq} \rangle^{\pm}$ for the different helicities, substitute Equation 39 for the moments, and obtain

$$\langle \sin \phi_{pq} \rangle^{+} - \langle \sin \phi_{pq} \rangle^{-} = \frac{N'_{LT}(A_0 - \frac{b_2}{2})}{(N_L + N_T)A_0} \quad . \tag{40}$$

Last, we assume $b_2 \ll A_0$ (which we discuss below) and use Equation 35 to rewrite the final result in terms of the partial cross sections instead of the N's so

$$\langle \sin \phi_{pq} \rangle^{+} - \langle \sin \phi_{pq} \rangle^{-} = \frac{N'_{LT} A_0}{(N_L + N_T)A_0} \tag{41}$$

$$= \frac{\sigma'_{LT}}{\sigma_L + \sigma_T} \tag{42}$$

$$= A'_{LT} \tag{43}$$

which is the result in Equation 17. To support the assumption that $b_2 << A_0$ we have extracted A'_{LT} using the weighted moments described here and by fitting the ϕ_{pq} dependence of the asymmetry (see Section 6.3.2). In fitting the ϕ_{pq} dependence we also explored the contribution of other terms and found them consistent with zero.

To show how we obtained Equation 16 recall that we can neglect N_{LT} and N_{TT} relative to N_L and N_T in the numerator of Equation 39. We retain the N'_{LT} term since it will survive when we take the difference between the moments for the different helicities. Applying this approximation and $b_2 \ll A_0$ to Equation 39 we obtain

$$\langle \sin \phi_{pq} \rangle^{\pm} = \frac{(N_L + N_T)a_1 \pm N'_{LT} A_0}{2(N_L + N_T)A_0} \tag{44}$$

$$= \frac{a_1}{2A_0} \pm \frac{N'_{LT}}{2(N_L + N_T)} \tag{45}$$

$$= \alpha \pm \frac{\sigma'_{LT}}{2(\sigma_L + \sigma_T)} \tag{46}$$

which is the form of Equation 16. We have used Equation 35 again to rewrite the final result in terms of the partial cross sections instead of the N's and labeled the first term α to be consistent with the text in Section 6.1.

F Radiative Corrections

To test our modifications to EXCLURAD we will compare them with the more traditional approaches. Below we describe how to relate the parameters of the Schwinger-style calculation with the approach used in EXCLURAD. In the Schwinger method one calculates the radiative correction for the scattering of an electron in a Coulomb field. This corresponds to inclusive electron scattering. An essential step in the calculation is to integrate over the radiative tail of the energy of a scattered electron to arrive at a correction factor for the yield lost to the emission of photons. The parameters of that integration are defined in Figure 70 [35]. The parameter ΔE is the energy range over which the integral is performed (starting

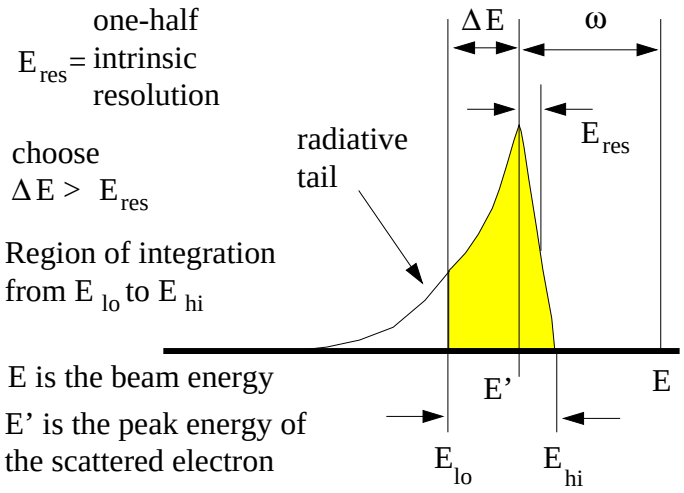

Figure 70: Energy spectrum of scattered electron showing definitions of quantities used in the Schwinger radiative correction calculation.

at the unradiated energy of the electron) to estimate the yield lost to radiated photons.

Afanasev, *et al.* follow an analogous procedure in their more sophisticated approach [25]. They integrate over the radiative tail of the scattered electron, but they perform the integration in terms of the covariant 'inelasticity' v defined as

$$v = \Lambda^2 - m_u^2 \tag{47}$$

where m_u is the mass of the undetected hadron and Λ is the four-momentum of the missing or undetected particles. The quantity v describes the missing mass due to the emission of a bremsstrahlung photon and can be rewritten as

$$v = W^2 + m_h^2 - m_u^2 - 2WE_h \tag{48}$$

where W is the mass of the system recoiling against the electron, m_h is the mass of the detected hadron, and E_h is the center-of-mass energy of the detected hadron. To determine the relationship between ΔE and v consider the usual expression for W^2

$$W^2 = M^2 + 2M(E - E') - Q^2 \tag{49}$$

where

$$Q^2 \approx 4EE' \sin^2 \frac{\theta}{2} \tag{50}$$

M is the target mass, and θ is the electron scattering angle. However, for an event with a radiated photon, the measured energy of the scattered electron is not E', but some lower energy

$$E_{lo} = E' - \Delta E \tag{51}$$

so W for this event will not be 'correct'. The new value of W is

$$W^2_{rad} = M^2 + 2M(E - E_{lo}) - 4EE_{lo} \sin^2 \frac{\theta}{2} \quad . \tag{52}$$

Using Equations 51 and 52 in the expression for v in Equation 48 one obtains the following function of ΔE.

$$v = M^2 + 2M(E - E' + \Delta E) - 4E(E' + \Delta E) \sin^2 \frac{\theta}{2} + m_h^2 - m_u^2 - 2E_h \sqrt{M^2 + 2M(E - E' + \Delta E) - 4E(E' + \Delta E) \sin^2 \frac{\theta}{2}} \tag{53}$$

This expression can be re-arranged so

$$v = W_0^2 + m_h^2 - m_u^2 + 2\Delta E(M + 2E \sin^2 \frac{\theta}{2}) - 2E_h \sqrt{W_0^2 + 2\Delta E(M + 2E \sin^2 \frac{\theta}{2})} \tag{54}$$

where

$$W_0^2 = M^2 + 2M(E - E') - 4EE' \sin^2 \frac{\theta}{2} \tag{55}$$

and the quantities E, E', and θ are determined by the electron kinematics. The hadron energy E_h is determined by the choice of the angle of the outgoing hadron relative to $\vec{q}$, the three-vector of the momentum transfer. The masses M, m_h, and m_u are all known.

As an example of applying Equation 54 consider the following kinematics in Table 11. The results of the calculation are shown in Figure 71. The dependence of v on ΔE is almost

$E = 2.558$ GeV	$E' = 2.345$ GeV	$\theta = 14.84°$
$m_h = 0.938$ GeV	$m_u = 0.940$ GeV	$\theta_h^{cm} = 45°$
$M = 1.876$ GeV	$Q^2 = 0.52$ (GeV/c)^2	$W = 1.93$ GeV

Table 11: Kinematics for calculating $v(\Delta E)$.

linear implying the importance of that term in Equation 54 over the sum of all the other terms.

A comparison of radiative corrections calculated with EXCLURAD with ones calculated using the Schwinger method is shown in Figure 72. We do not expect the two calculations to be precisely the same because each one uses a different model for the response functions

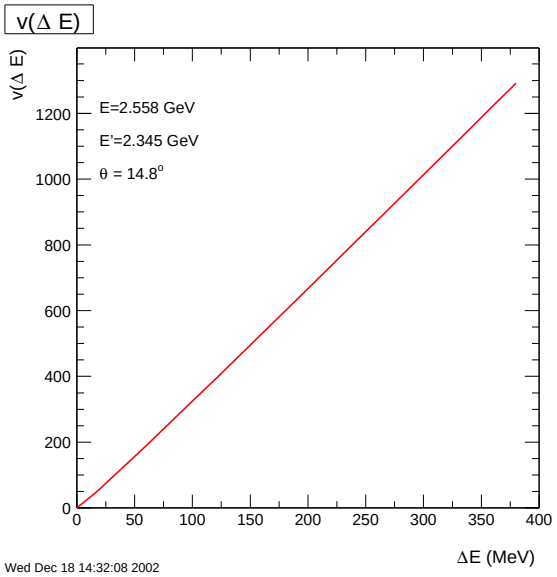

Figure 71: Dependence of v on ΔE for the kinematics listed in Table 11.

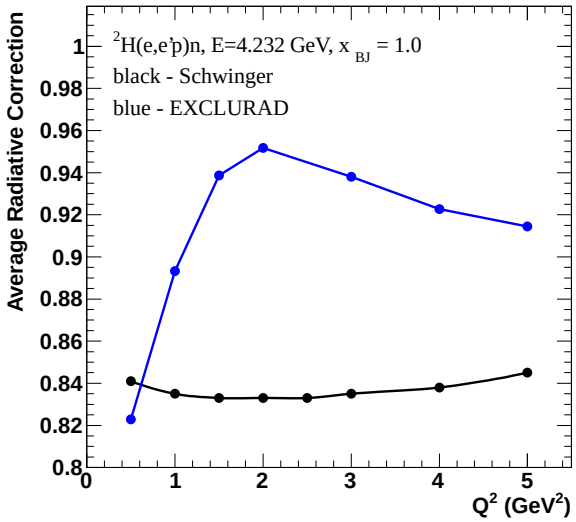

Figure 72: Comparison of radiative corrections calculated with EXCLURAD (blue) and using the Schwinger method (black).

(EXCLURAD uses the DEEP code [11]). The EXCLURAD calculation is, on average, about 10% higher than the Schwinger one and varies more with Q^2(from about 2% less to about 14% larger). This Q^2 dependence is similar to the behavior observed in EXCLURAD calculations for other reactions [25]. More details can be found in Ref. [28].

G Applying Radiative Corrections

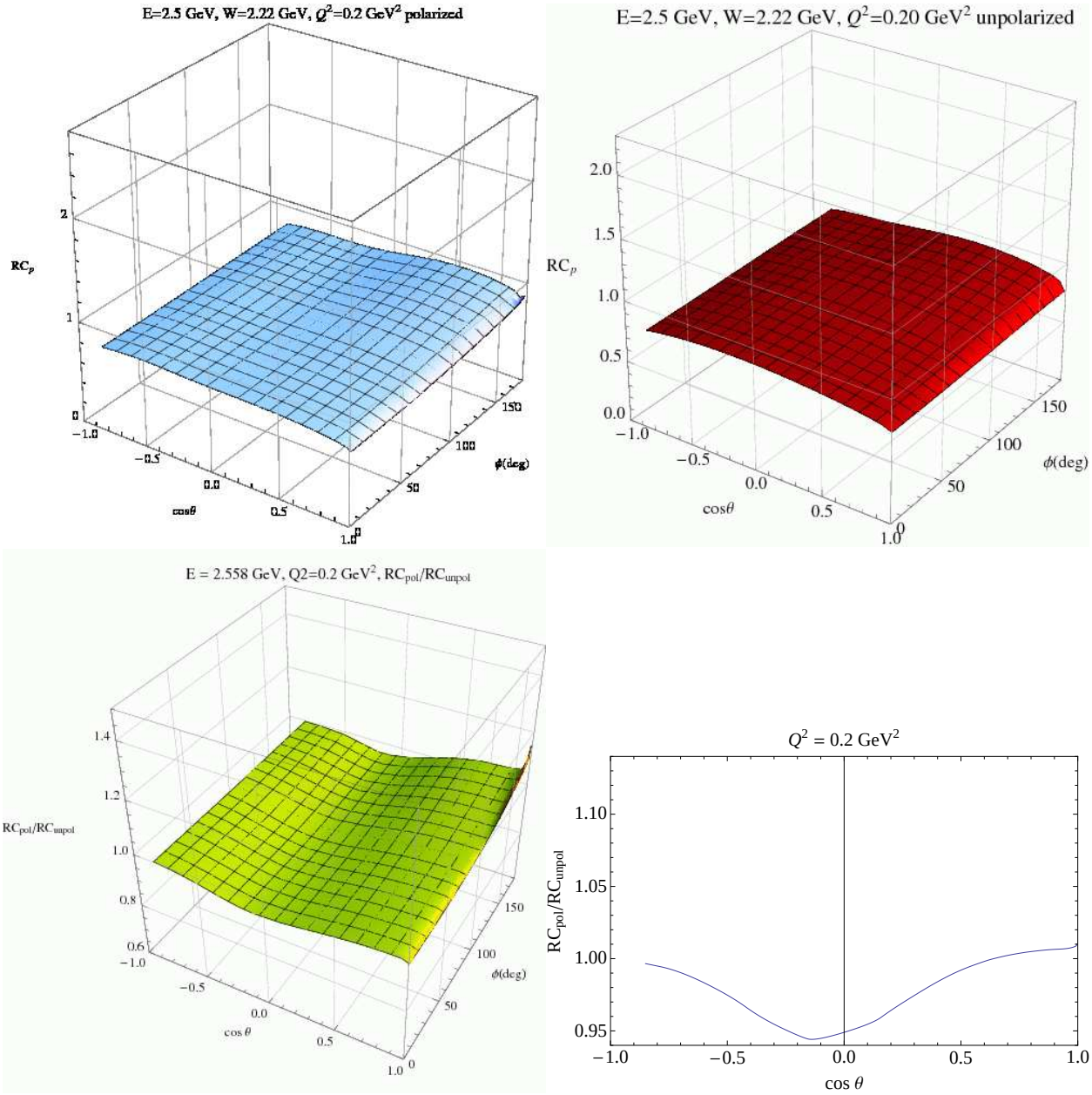

Figure 73: Radiative corrections for polarized (upper-left) and unpolarized (upper-right) cross sections and their ratio (lower-left) are plotted as functions of $\cos\theta$ and ϕ at Q^2 = 0.2 (GeV/c)^2. The average over ϕ is shown in the lower-right panel.

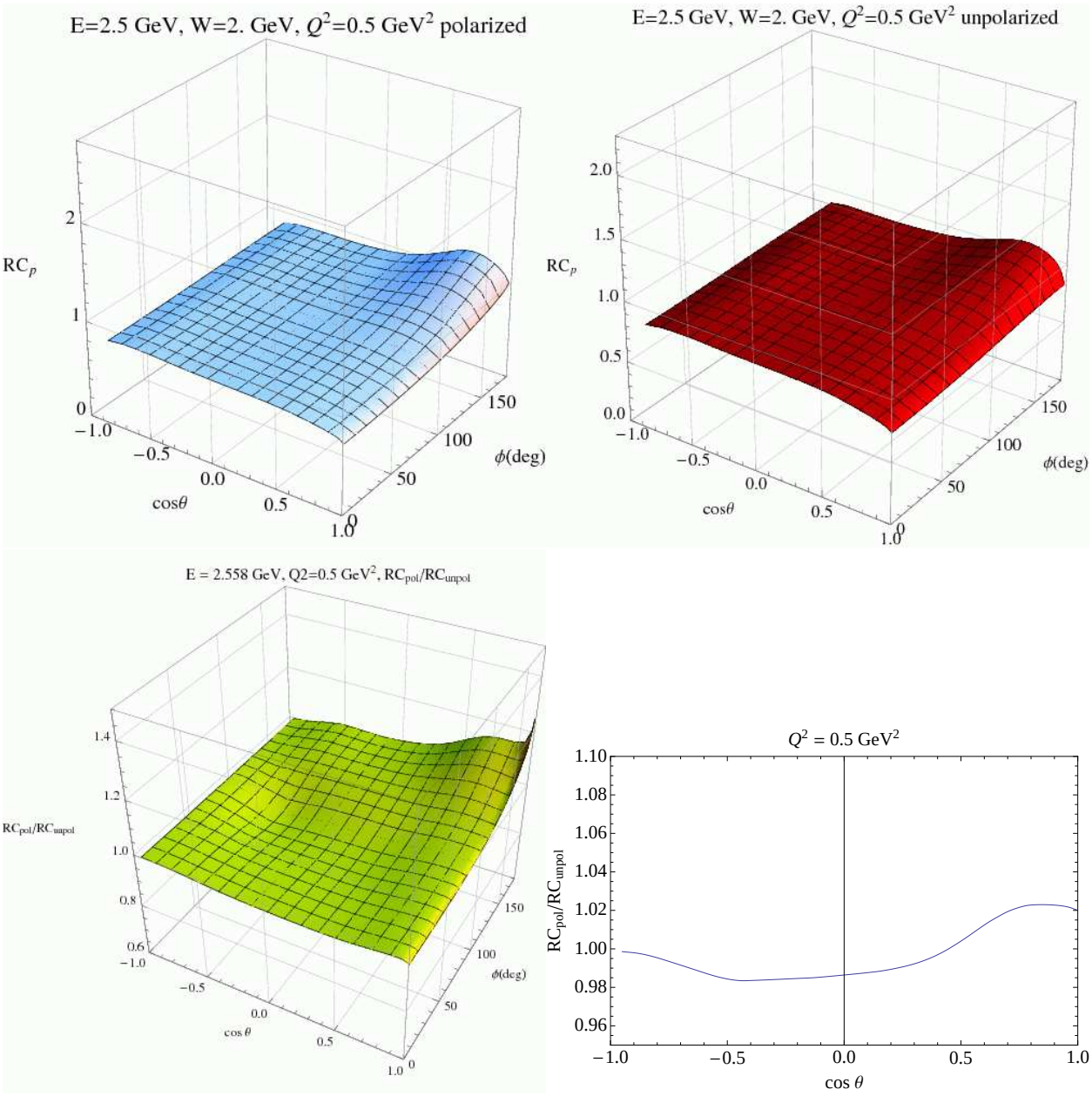

Figure 74: Radiative corrections for polarized (upper-left) and unpolarized (upper-right) cross sections and their ratio (lower-left) are plotted as functions of $\cos\theta$ and ϕ at Q^2 = 0.5 (GeV/c)^2. The average over ϕ is shown in the lower-right panel.

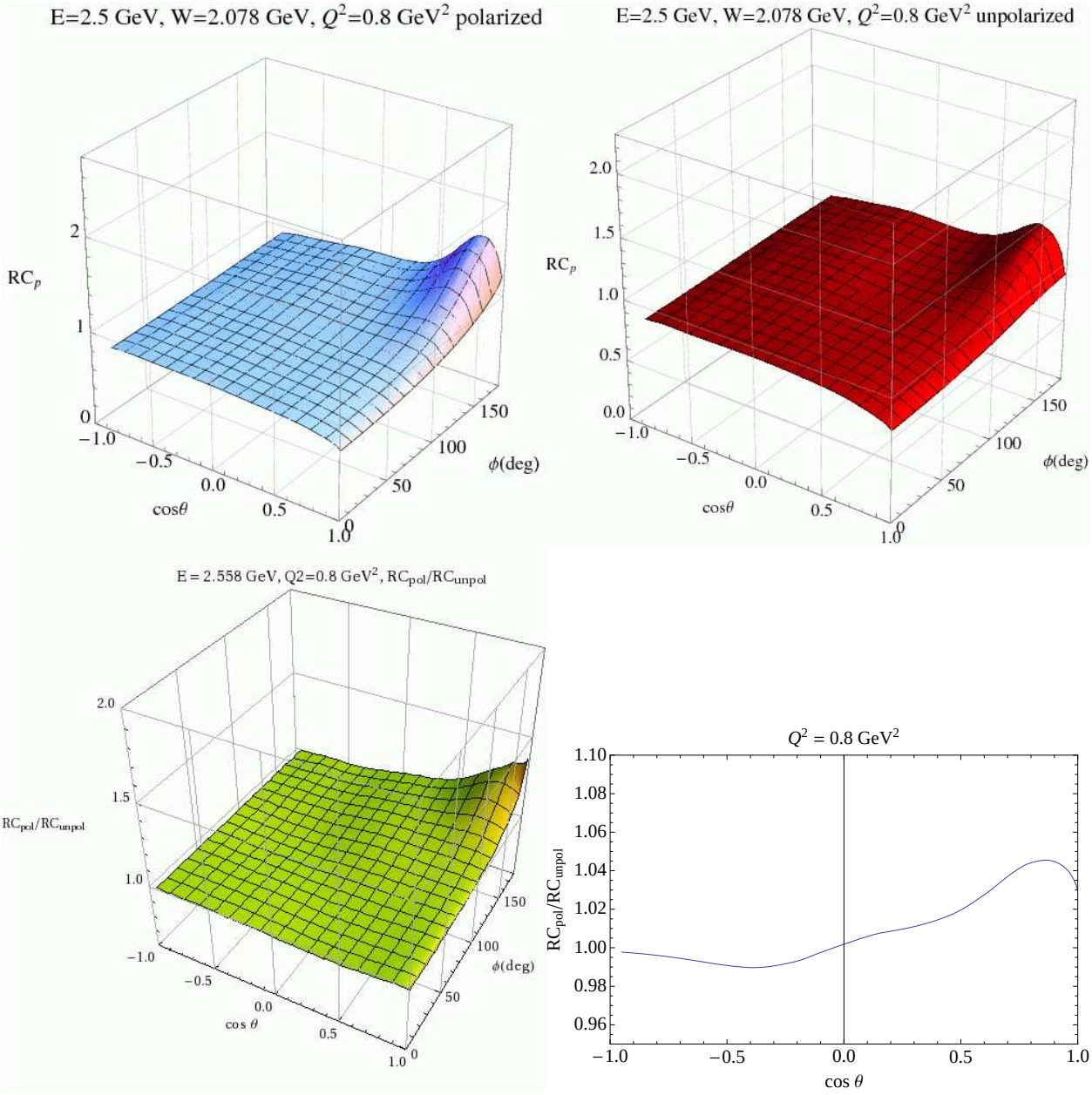

Figure 75: Radiative corrections for polarized (upper-left) and unpolarized (upper-right) cross sections and their ratio (lower-left) are plotted as functions of $\cos\theta$ and ϕ at Q^2 = 0.8 (GeV/c)^2. The average over ϕ is shown in the lower-right panel.

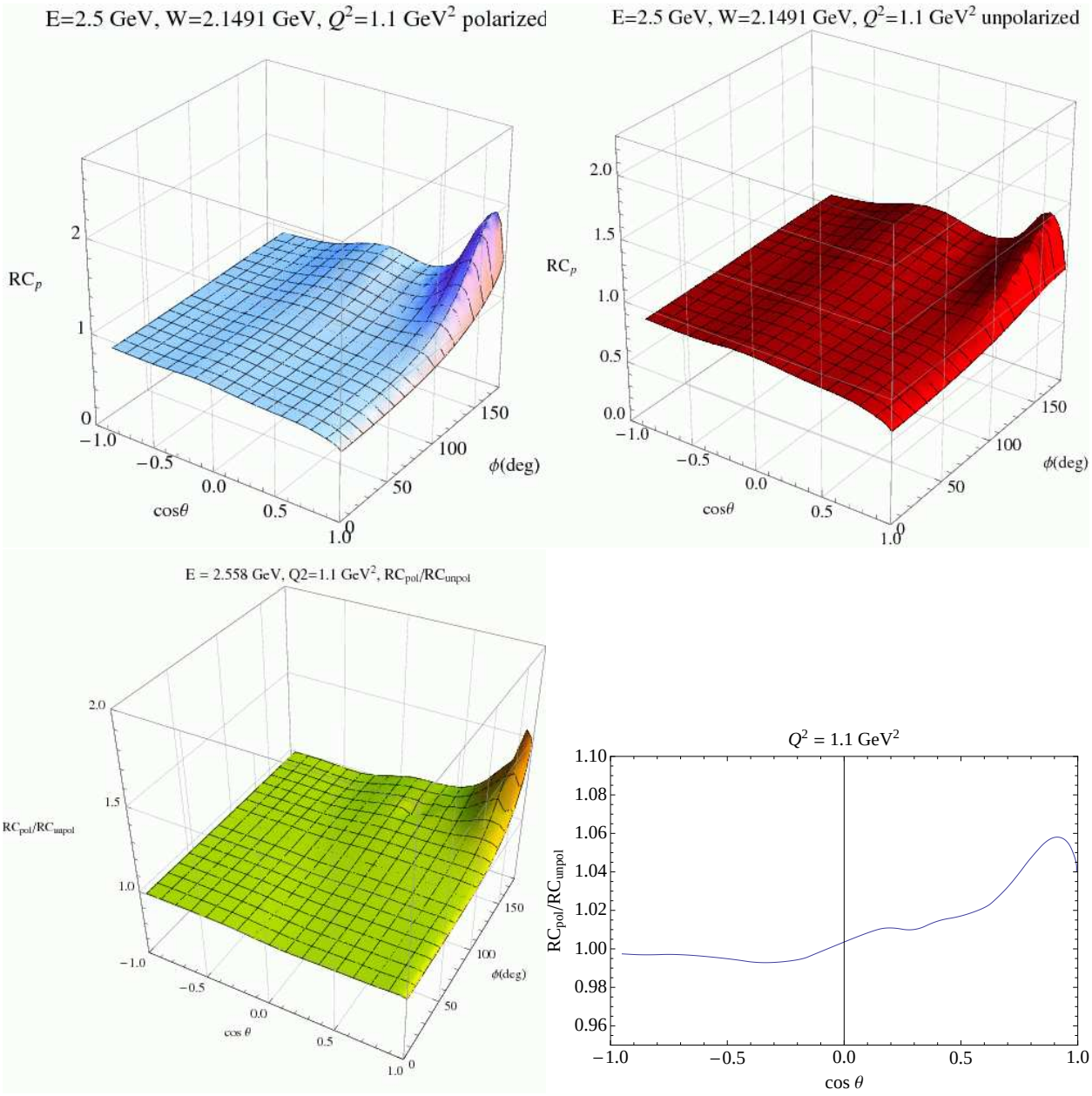

Figure 76: Radiative corrections for polarized (upper-left) and unpolarized (upper-right) cross sections and their ratio (lower-left) are plotted as functions of $\cos\theta$ and ϕ at Q^2 = 1.1 (GeV/c)^2. The average over ϕ is shown in the lower-right panel.

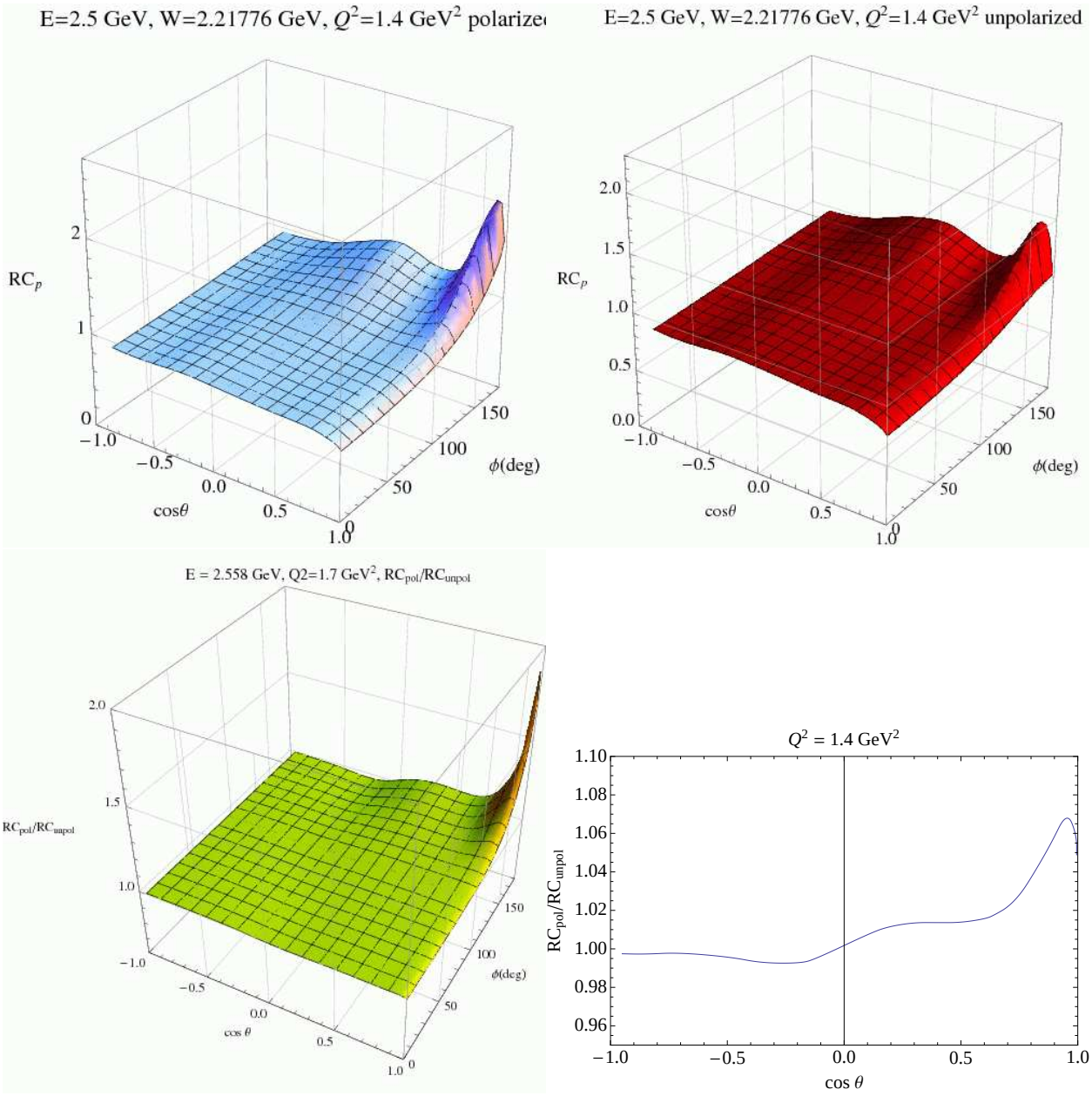

Figure 77: Radiative corrections for polarized (upper-left) and unpolarized (upper-right) cross sections and their ratio (lower-left) are plotted as functions of $\cos\theta$ and ϕ at Q^2 = 1.4 (GeV/c)^2. The average over ϕ is shown in the lower-right panel.

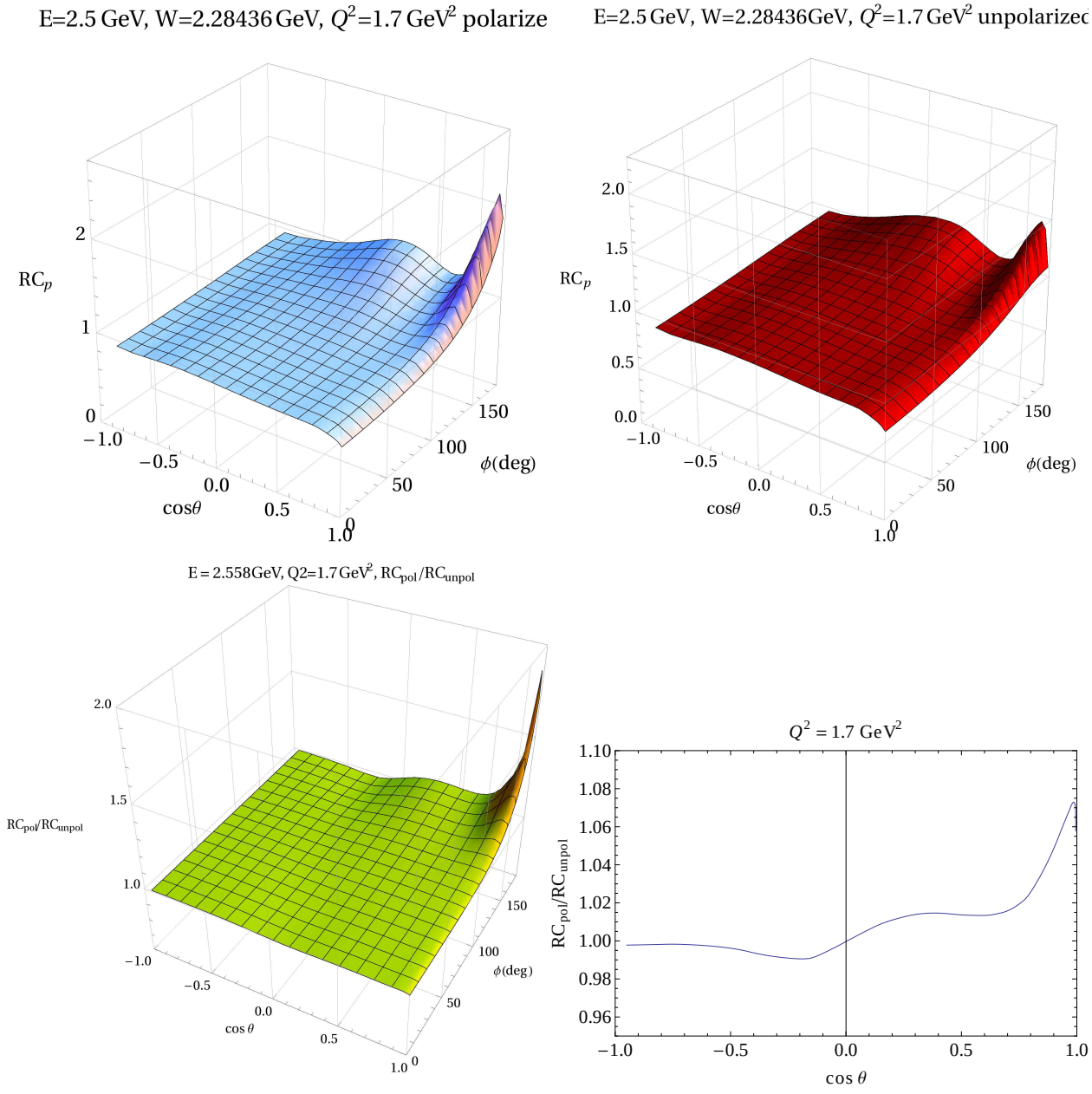

Figure 78: Radiative corrections for polarized (upper-left) and unpolarized (upper-right) cross sections and their ratio (lower-left) are plotted as functions of $\cos\theta$ and ϕ at Q^2 = 1.7 (GeV/c)^2. The average over ϕ is shown in the lower-right panel.

H Monte Carlo Simulation of Quasielastic Scattering in Deuterium

To simulate the quasielastic production we treat the deuteron as composed of two, on-shell nucleons, one of which will act as a spectator in the interaction. We start with the existing, elastic, nucleon form factors. The differential cross section for elastic electron-nucleon scattering can then be calculated in the laboratory frame as [36]

$$\frac{d\sigma}{d\Omega} = \sigma_{Mott}\left[\left(F_1^2 + \frac{\kappa^2 Q^2}{4M^2}F_2^2\right) + \frac{Q^2}{2M^2}\left(F_1 + \kappa F_2\right)^2 \tan^2\left(\frac{\theta}{2}\right)\right] \tag{56}$$

where θ is the electron scattering angle and σ_{Mott} is

$$\sigma_{Mott} = \frac{\alpha^2 E' \cos^2(\frac{\theta}{2})}{4E^3 \sin^4(\frac{\theta}{2})} \quad . \tag{57}$$

It is preferable to define different electromagnetic form factors that are related to the charge and magnetization density of the nucleon in the appropriate kinematics. These so-called Sachs form factors are defined as

$$G_E = F_1 - \frac{\kappa Q^2}{4M^2}F_2 \qquad G_M = F_1 + \kappa F_2 \tag{58}$$

so Equation 2 can be written as

$$\frac{d\sigma}{d\Omega} = \sigma_{Mott}\left(G_E^2 + \frac{\tau}{\epsilon}G_M^2\right)\left(\frac{1}{1+\tau}\right) \tag{59}$$

where

$$\tau = \frac{Q^2}{4M^2} \qquad \text{and} \qquad \epsilon = \frac{1}{1 + 2(1+\tau)\tan^2(\frac{\theta}{2})} \quad . \tag{60}$$

We used Equations 56-60 and made the following assumptions about the form factors

$$G_E^p \approx G_D = \frac{1}{(1 + Q^2/\Delta)^2} \qquad G_M^p \approx \mu_p G_D \qquad G_M^n \approx \mu_n G_D \qquad G_E^n \approx 0 \tag{61}$$

where μ_n and μ_p are the neutron and proton magnetic moments and $\Delta = 0.71$ GeV^2. The number of quasielastic events in a particular Q^2 bin is calculated from the elastic form factors. Next, the Fermi momentum $\vec{p}_f$ for one of the nucleons is chosen at random (the spectator nucleon has momentum $-\vec{p}_f$) and we simulate the kinetics of the scattering. The nucleon momentum $\vec{p}_f$ inside the deuteron is chosen from the Hulthen distribution shown in Figure 79 which depends only on the p_f [37].

We also have to account for the combined effect of the Fermi motion and the beam energy dependence of the elastic cross section. A nucleon whose Fermi motion is directed towards the incoming electron will observe a higher energy beam in its rest frame and (because of the elastic cross section dependence on the beam energy) will have a lower cross section for interacting. Conversely, a nucleon 'running away' from the beam will see

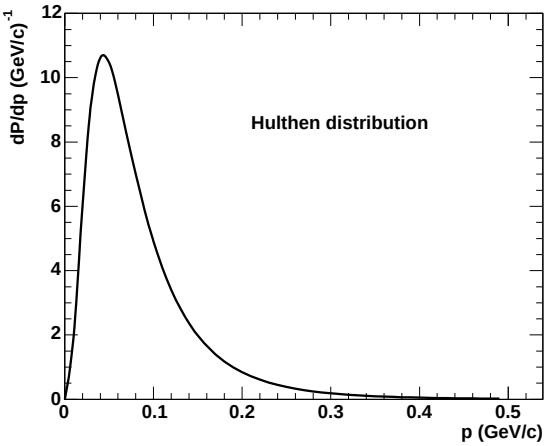

Figure 79: Hulthen distribution representing the nucleon Fermi momentum inside the deuteron.

a lower effective beam energy and have a higher cross section. For a given choice of Fermi momentum p_f and nucleon polar angle $\cos\theta$ there is an effective beam energy in the rest frame of the moving nucleon. The size of the cross section at this effective beam energy in the nucleon rest frame and the Hulthen distribution will determine the relative weight of this $p_f - \cos\theta$ combination. At each effective beam energy in the quasielastic case the Brash parameterization [38] of the nucleon cross section is used to obtain the cross section dependence on the electron scattering angle. This angular dependence is then integrated over the CLAS angular acceptance to obtain the weighting for this effective beam energy (and $p_f - \cos\theta$ point). Multiplying this effective-beam-energy weight with the Hulthen distribution yields the weight function for electron-proton scattering shown in Figure 80. The Hulthen distribution produces a long ridge in the range of the Fermi momentum $p_f \approx 0.04 - 0.05$ GeV/c and the cross section dependence on the effective beam energy creates a downward slope along this ridge from forward to backward angles. The azimuthal angle ϕ_f of the nucleon is chosen from a uniform, random distribution in the range $\phi_f = 0 - 2\pi$. Once the Fermi momentum is chosen, a relativistic boost is made to the rest frame of the nucleon for all particles and the coordinate system is rotated so the incoming electron is along the z axis. A new beam energy is calculated. A nucleon, rest-frame electron scattering angle is chosen from a random distribution weighted by the Brash parameterization. Last, the momenta of the electron and nucleon are transformed back to the laboratory frame. This method was implemented in the program QUEEG and used to simulate quasielastic events in Ref. [14].

To summarize, we use the Brash parameterization of the elastic cross section to choose the number of quasielastic events in a particular Q^2. The Fermi momentum for each is chosen with the combined weights of the Hulthen distribution and the cross section dependence on the effective beam energies at each $p_f - \cos\theta$ point. Once the Fermi momentum is determined, the system is boosted to the nucleon rest frame. The final 4-vectors are chosen from the

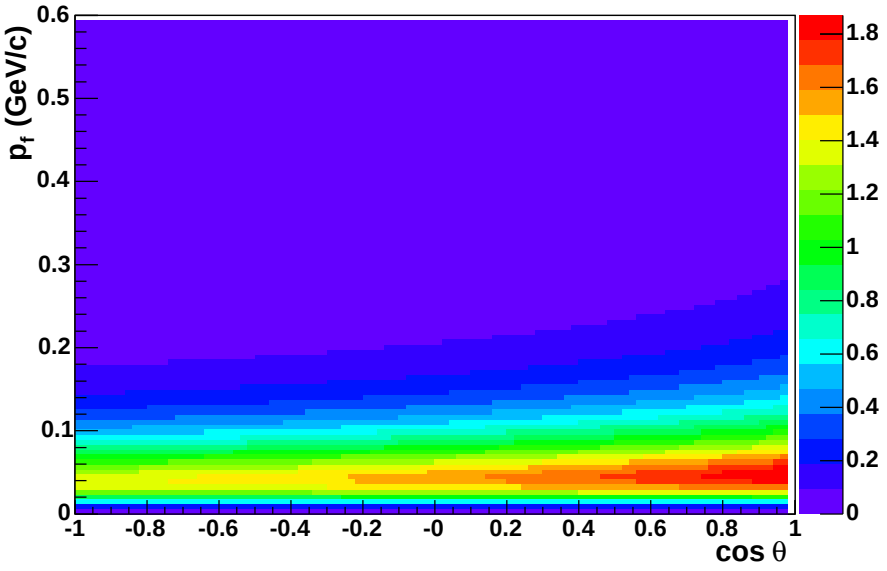

Figure 80: Plot of the weighting function for electron-proton scattering

Brash parameterization (quasielastic case) and the final states are then transformed back to the laboratory frame.

I Systematic Uncertainties

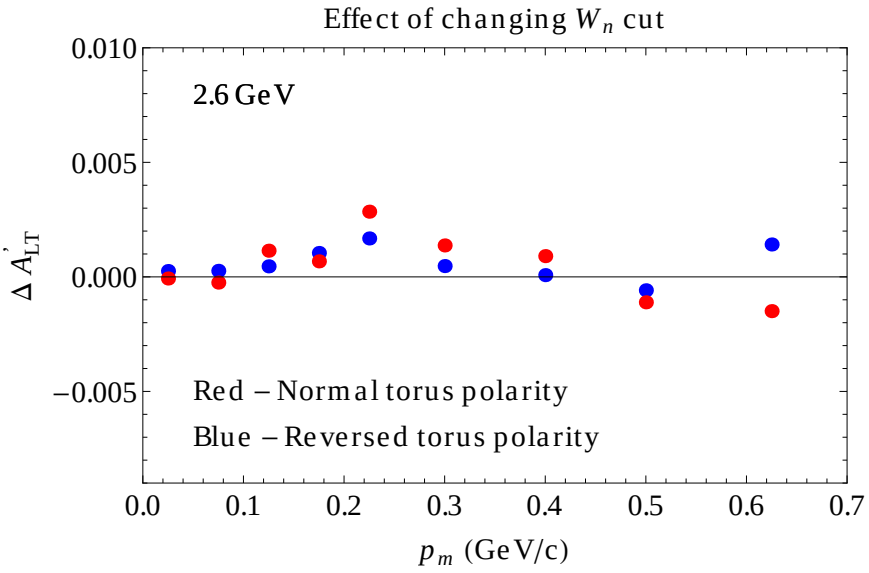

Figure 81: Systematic uncertainties due to the W_n cut.

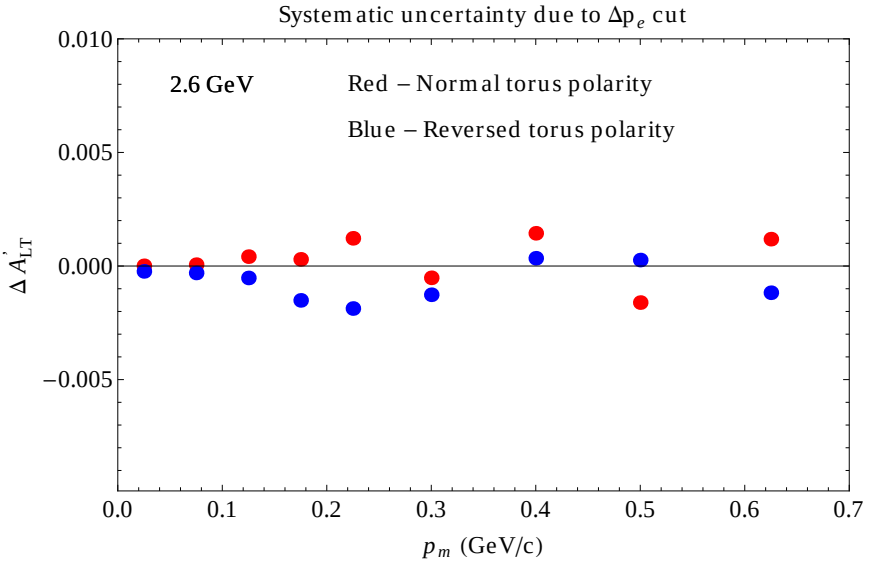

Figure 82: Systematic uncertainties due to the Δp_e cut.

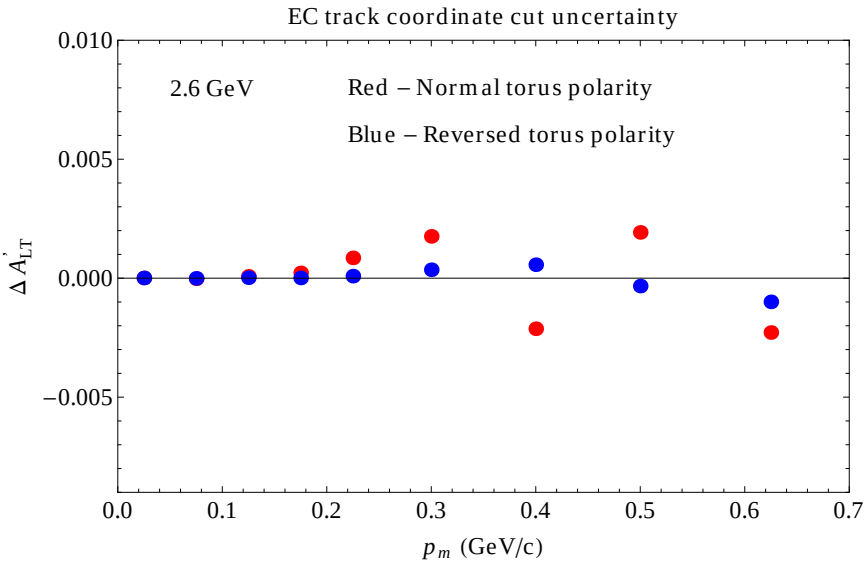

Figure 83: Systematic uncertainties due to the electromagnetic calorimeter tracking coordinate cut.

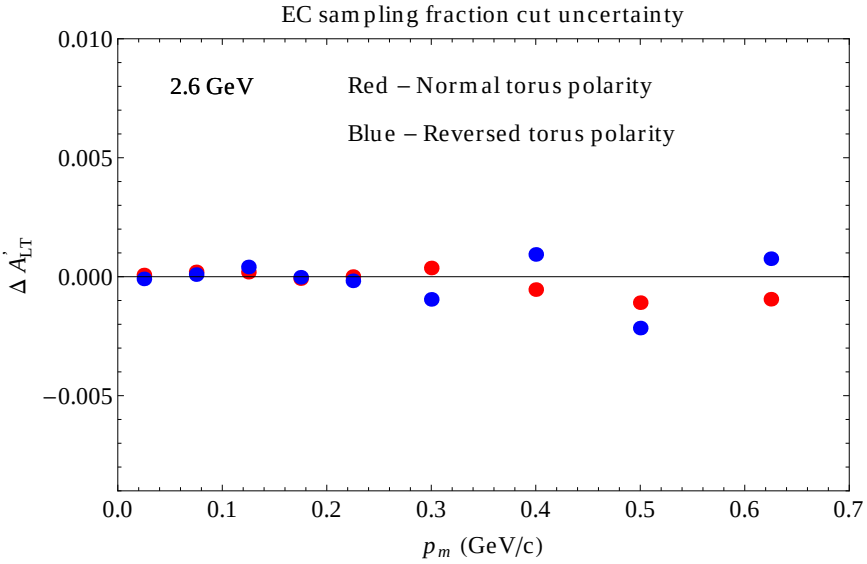

Figure 84: Systematic uncertainties due to the electromagnetic calorimeter sampling fraction cut.

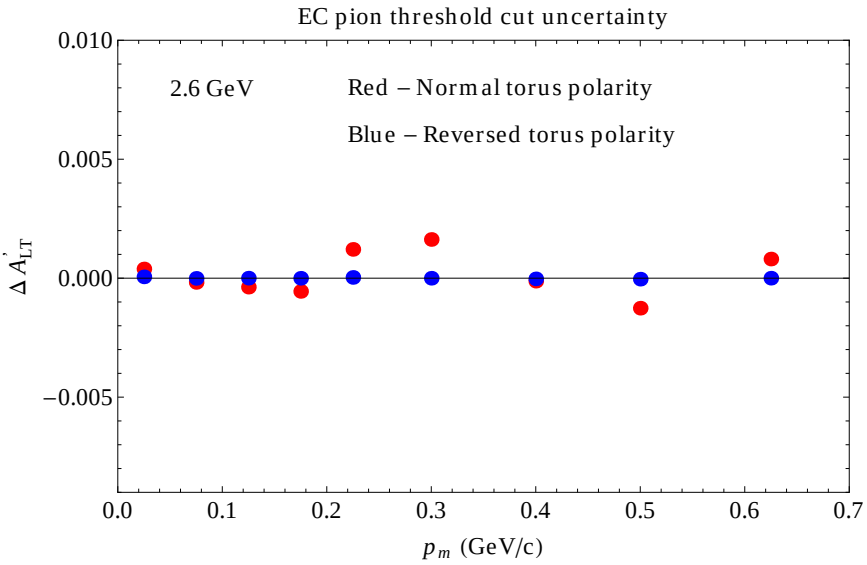

Figure 85: Systematic uncertainties due to the electromagnetic calorimeter pion threshold cut.

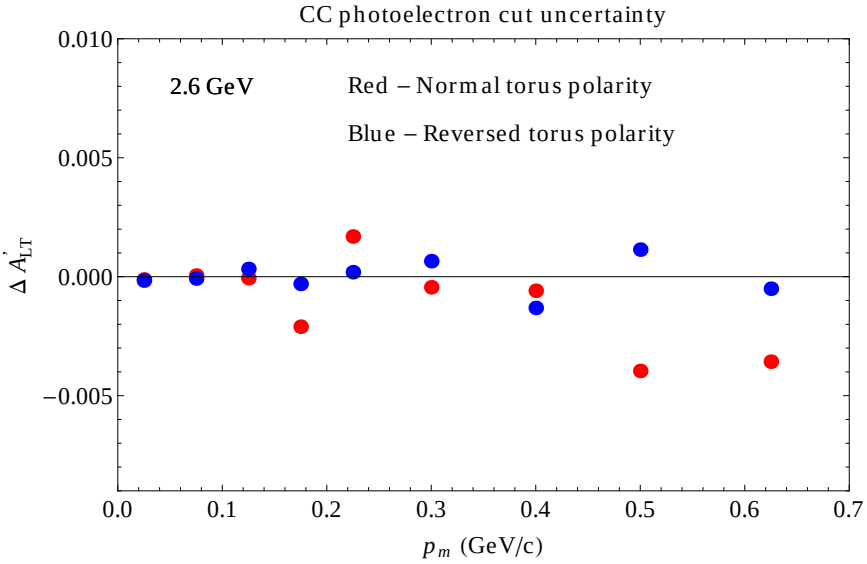

Figure 86: Systematic uncertainties due to the Cherenkov counter photoelectron cut.

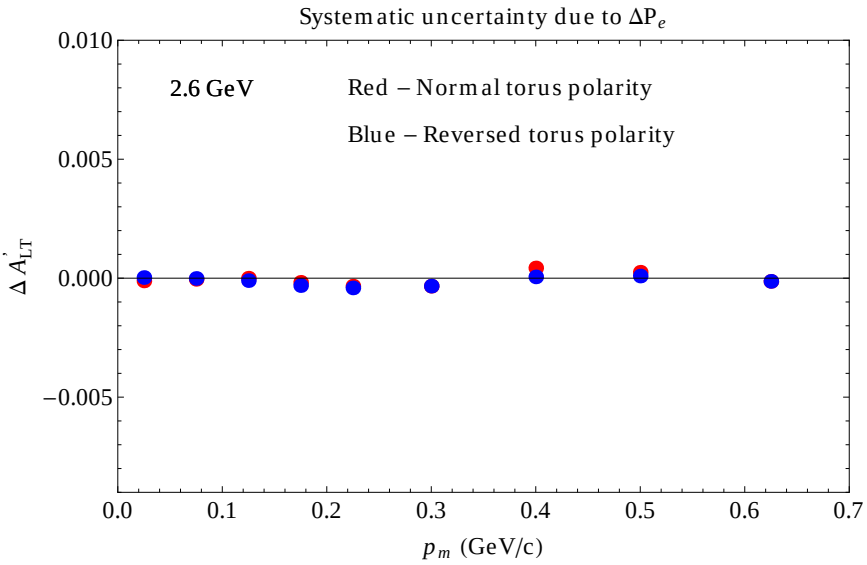

Figure 87: Systematic uncertainties due to the beam polarization.

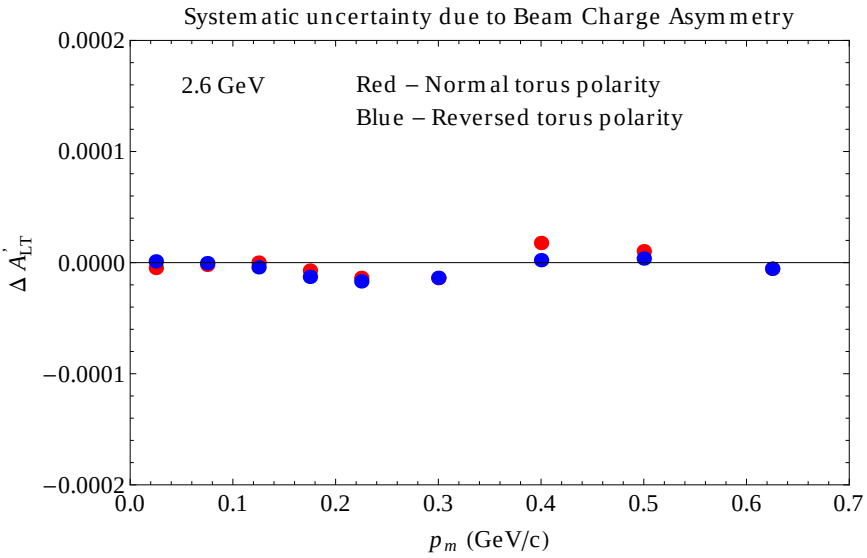

Figure 88: Systematic uncertainties due to the beam charge asymmetry. Note the difference in the scale.

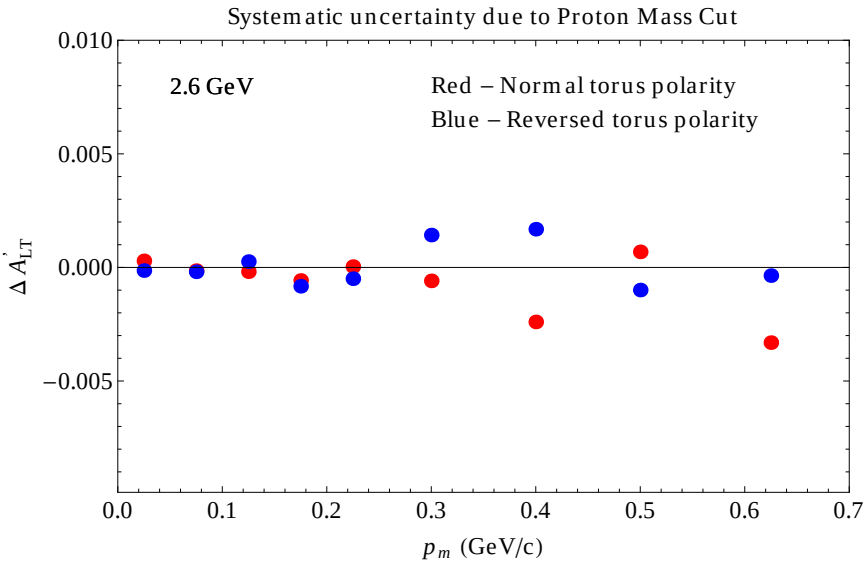

Figure 89: Systematic uncertainties due to proton mass cut.

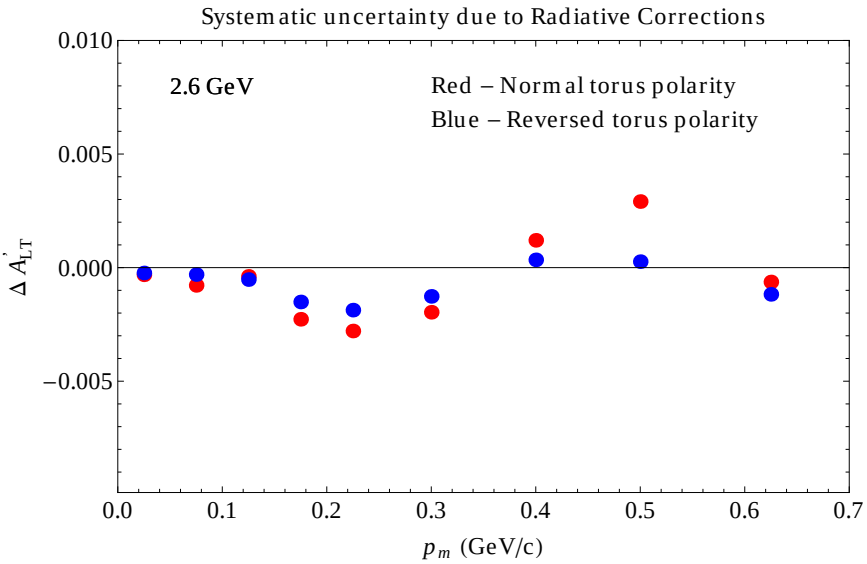

Figure 90: Systematic uncertainties due to the radiative corrections.